# Dissertation

**submitted to the**

**Combined Faculty of Mathematics,**
**Engineering Sciences, and Natural Sciences**

**of the**

**Ruprecht Karl University of Heidelberg**

**for the degree of**

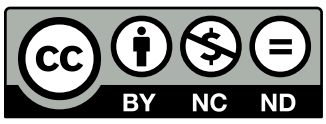
**Doctor of Engineering**

Study and application of incremental digital integration: a novel X-ray detector readout for synchrotron applications

put forward by:
Marin Collonge

Referees: Professor Dr. Peter Fischer
Dr. Pablo Fajardo

This work is licensed under a Creative Commons "Attribution-NonCommercial-NoDerivatives 4.0 International" license.



# Abstract

Cutting-edge synchrotron radiation sources like the ESRF-EBS have significantly enhanced X-ray beam capabilities, generating photon fluxes surpassing previous-generation sources by up to three orders of magnitude. This poses a challenge in detector science, as current state-of-the-art photon-counting hybrid pixel detectors cannot sustain such elevated fluxes. Addressing this, the XIDer project, a collaboration between the ESRF and Heidelberg University, is developing a novel detector with improved readout electronics and sensor material. High-density compound semiconductor materials, particularly CdTe and CdZnTe, are selected as suitable materials for detecting X-rays in the 30–100 keV energy range, despite their non-idealities. XIDer employs a novel versatile readout concept, incremental digital integration, enabling a high dynamic range and reduced sensitivity to sensor leakage variations.

In this thesis, the performance of a digitally integrating detector with a 1-mm thick Cd(Zn)Te sensor is assessed with Monte-Carlo simulations. Results indicate functional equivalence to photon-counting at low fluxes, with energy-dependent readout losses, and equivalence to lossless conventional charge integration at very high fluxes.

The successful implementation of incremental digital integration in two stages, driven by a charge removal concept, is demonstrated experimentally on the fourth generation of XIDer prototypes, featuring a 16-pixel Cd(Zn)Te sensor and a custom-designed readout ASIC. A calibration procedure is presented and assessed. Selected XIDer assemblies are characterised with reference to the target requirements. Electronic noise measurements validate single-photon resolution, and characterisation under 30 keV synchrotron X-rays demonstrate the detector linearity. A maximum detectable flux of 680 Mcps/pixel is achieved. The flux-induced leakage current in Cd(Zn)Te sensors, characterised using X-rays and a pulsed LED, is observed to be significant and will require further investigation for optimal detector performance.

The XIDer collaboration marks good progress in addressing the challenges posed by upgraded synchrotron sources, with most parameters approaching their targets, and showcasing advancements in sensor materials and readout schemes for next-generation X-ray detectors.

# Contents

**Abstract** **v**

**Contents** **vii**

**1 The XIDer project** **1**

1.1 Introduction . . . . . 1

1.1.1 The ESRF - Extremely Brilliant Source . . . . . 1

1.1.2 New scientific opportunities . . . . . 2

1.1.3 Demand for new X-ray detectors . . . . . 3

1.1.4 Target specifications . . . . . 5

1.2 Hybrid pixel semiconductor detection . . . . . 6

1.2.1 Overview on available high-Z sensor materials . . . . . 8

1.2.2 Focus on high-density compound semiconductor issues . . . . . 10

1.2.3 Photon-counting readout . . . . . 13

1.2.4 Conventional charge-integrating readout . . . . . 14

1.2.5 State of the art summary . . . . . 16

1.3 The XIDer detector . . . . . 17

1.3.1 A novel readout: incremental digital integration . . . . . 18

1.3.2 Advantages and foreseen challenges over state-of-the-art detectors 20

1.4 Outline of the manuscript . . . . . 21

**2 *A priori* investigation of incremental digital integration** **23**

2.1 Simulated performance of a digitally integrating detector using X-DECIMO . . . . . 23

2.1.1 Monte Carlo simulation tool . . . . . 23

2.1.2 Simulation setup . . . . . 25

2.1.3 Material performance . . . . . 28

2.1.4 Readout performance with flux . . . . . 29

2.1.5 Readout performance with X-ray energy . . . . . 33

2.1.6 Statistics retrieved from a Poisson source with uniform illumination . . . 35
2.2 Readout limitations . . . 37
2.2.1 Role of calibration . . . 37
2.2.2 Effect of noise and dark current . . . 40
2.3 Conclusion . . . 41

**3 System Description 43**
3.1 ASIC prototype . . . 43
3.1.1 Front-end . . . 43
3.1.2 Front-end trimming . . . 45
3.1.3 Charge injection circuit . . . 47
3.1.4 Sequencer . . . 47
3.1.5 Data handling: the telegram interface . . . 52
3.2 Sensor prototype . . . 53
3.3 Characterisation apparatus . . . 54
3.3.1 Carrier and mezzanine printed circuit boards . . . 54
3.3.2 Complete setup . . . 56
3.4 Characterisation software . . . 57
3.5 Sensor-ASIC assemblies . . . 59
3.5.1 Hybridisation procedure . . . 59
3.5.2 Hybridised assemblies of interest . . . 60
3.6 Light sources used for characterisation . . . 61
3.6.1 Visible LED in-lab setup . . . 62
3.6.2 Beamline setup . . . 62

**4 Calibration 67**
4.1 Calibration procedure . . . 67
4.1.1 Calibration of the internal injection circuit . . . 68
4.1.2 Calibration of the threshold . . . 70
4.1.3 Calibration of the charge pump packet size . . . 71
4.2 Preliminary assessment . . . 73
4.2.1 Baseline stability . . . 73
4.2.2 Influence of DAC resolution . . . 73
4.2.3 Dispersion of individual calibrated parameters . . . 74
4.2.4 Dispersion of front-end linearity with internal injection . . . 76
4.3 Calibration assessment with charge injection . . . 77
4.3.1 Assessment with internal injection circuit . . . 78

4.3.2 Assessment with external injection circuit . . . . . 78
4.4 Calibration assessment with LED illumination . . . . . 79
4.5 Calibration assessment with X-rays at a beamline . . . . . 81
4.6 Conclusion . . . . . 82

**5 Assembly characterisation 85**
5.1 Noise considerations . . . . . 86
5.1.1 Equivalent noise charge . . . . . 86
5.1.2 Dark flux . . . . . 88
5.2 Characterisation of transfer phase . . . . . 89
5.3 High dynamic range and linearity . . . . . 92
5.3.1 Maximum dynamic range under charge injection . . . . . 92
5.3.2 Linearity under 30 keV X-ray irradiation . . . . . 93
5.3.3 X-ray counting statistics . . . . . 95
5.4 Time-resolved capabilities . . . . . 96
5.4.1 Charge collection in a front-end . . . . . 97
5.4.2 Quantifying flux-induced leakage with a pulsed LED . . . . . 98
5.5 Flux-induced leakage transients . . . . . 100
5.5.1 Measuring the slow afterglow components under X-ray irradiation 101
5.5.2 Measuring the microsecond time scale afterglow components under pulsed LED irradiation . . . . . 103

**6 Summary and conclusions 107**

**7 Appendix 113**
7.1 Table of hybridised prototype assemblies . . . . . 113

**Bibliography 117**

**Acknowledgements 131**

# Chapter 1

# The XIDer project

New scientific opportunities have emerged from recent upgrades of synchrotron radiation facilities, and with that, new requirements and expectations for improved X-ray detection technology have surfaced. This chapter first introduces the motivations to start the XIDer detector project at the heart of this manuscript, and covers the basic elements of hybrid pixel detection with a focus on high-density compound semiconductors (high-Z materials). The XIDer detector project and its novel readout scheme is then presented. Part of this chapter is taken or adapted from [1].

## 1.1 Introduction

### 1.1.1 The ESRF - Extremely Brilliant Source

Founded with the objective of providing cutting-edge synchrotron radiation for multidisciplinary research, the European Synchrotron Radiation Facility (ESRF) operates a state-of-the-art synchrotron radiation source, generating intense X-ray beams through the manipulation of high-energy electrons. Accelerators are employed to impart relativistic speeds to electrons, which are stored in a 844 m ring [2]. As the electrons are deflected by magnetic fields inside the storage ring, they follow curved trajectories, and in the process emit electromagnetic waves called synchrotron radiation. The ESRF developed advanced synchrotron beamlines, represented in Figure 1.1 and equipped with intricate detectors, enabling unprecedented insights into materials and biological structures at the atomic and molecular levels. A diverse community of users, ranging from physicists and chemists to biologists and material scientists, converges at such facilities to harness the powerful X-ray beams in various research applications [2].

The ESRF - Extremely Brilliant Source (ESRF-EBS) marked the advent of fourth-generation high-energy synchrotron facilities [2]. The ESRF-EBS upgraded storage

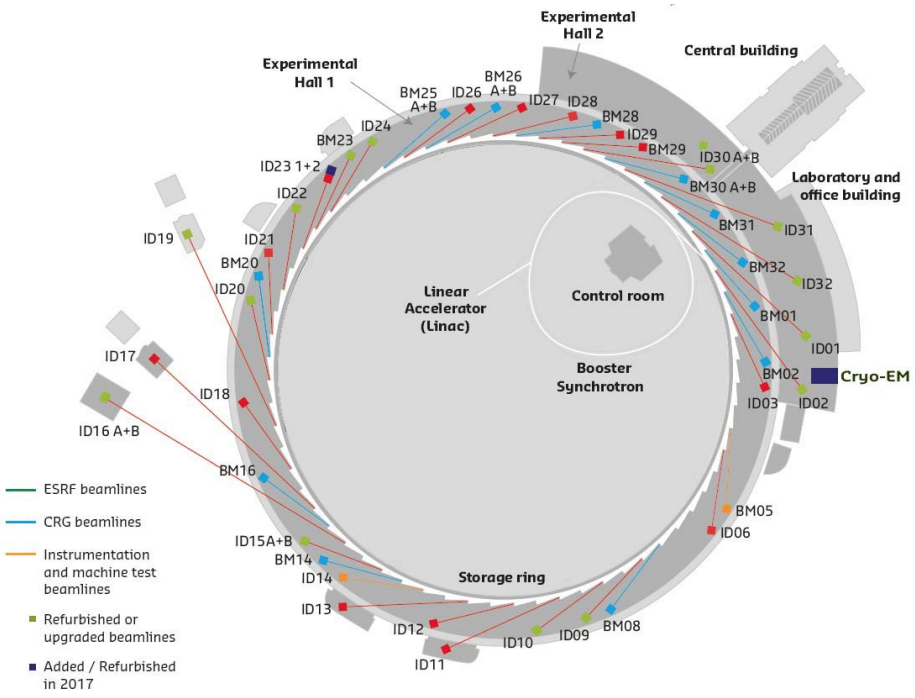



**Figure 1.1.** Location of the beamlines in the ESRF experimental halls in 2017. From [3].

ring, based on a novel hybrid multibend achromat lattice, allowed a reduction of the horizontal emittance of a factor 30 compared to the former ring [4, 5]. The utilisation of reduced-gap undulators and the incorporation of highly efficient optics enabled the generation of X-ray beams with further increased intensity [6, 7]. Overall, when compared to previous-generation facilities, the brilliance and coherence of the X-ray beam increased by up to three orders of magnitude, especially at hard X-ray energies [8]. The exact figure depends on the specific application.

As shown by Figure 1.2, the ESRF brilliance has grown exponentially with the years since first-generation synchrotron facilities, and is now reaching more than $10^{21}$ photons/s/mm$^2$/mrad$^2$/0.1%BW at 50 keV [9].

### 1.1.2 New scientific opportunities

An increased brilliance in the 30–100 keV energy range is beneficial for applications that require the measurement of strong signals, like many material science experiments such as high-pressure and single-bunch X-ray diffraction experiments. Notably, in these types of diffraction and scattering experiments where the studied sample is typically made of inorganic material, a high photon energy is required to effectively illuminate the regions of the sample being investigated. The dimensions of the illuminated volume are significantly larger compared to experiments studying samples made of organic material, and are usually well above 100 µm. In turn, this relaxes the

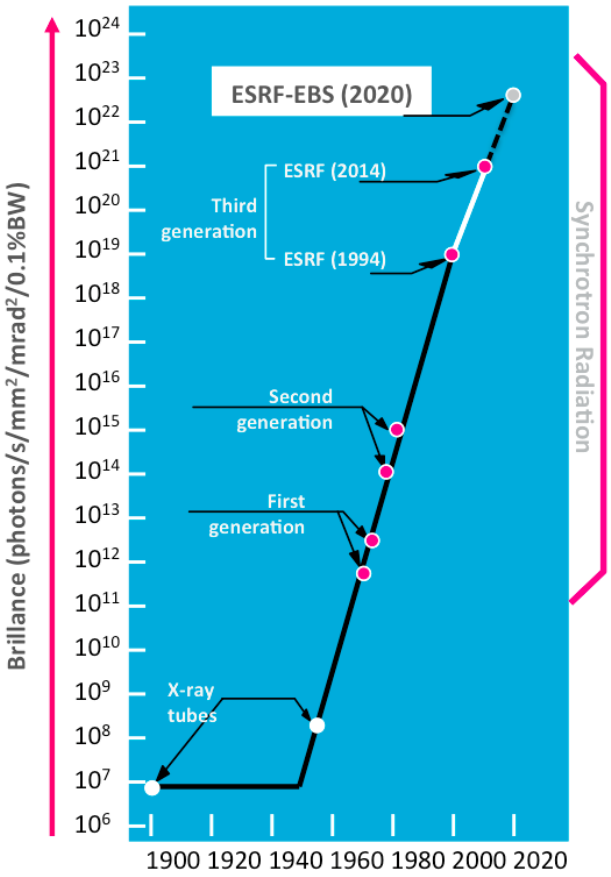



**Figure 1.2.** Evolution of ESRF X-ray brilliance with synchrotron generations. From [10].

pixel size requirements of the detectors down to the range of 100 µm to 200 µm.

Contrastingly, the detector can record in such diffraction experiments signals with extremely high dynamic range, sometimes surpassing $10^9$ photons per second per pixel. The photon statistics in experiments with such intensity enable the exploration of physical phenomena on the micro- and sub-microsecond time scales, including irreversible processes. These elusive time domains, that were challenging to access with the prior generation of synchrotron sources, are now within reach, provided that detectors are capable of sampling diffraction patterns at MHz rates and effectively managing the elevated incident photon flux.

### 1.1.3 Demand for new X-ray detectors

Currently, the 2D detectors utilised in diffraction and scattering experiments at synchrotron facilities like the ESRF are photon-counting hybrid pixel devices, comprised of a pixelated semiconductor sensor bonded to a photon-counting readout [11,12]. Due to their capability to directly convert X-ray photons into charge, these devices offer the single-photon sensitivity necessary for photon counting operation. This signal-

processing approach yields output data with exceptionally low readout noise, which is practically negligible in most cases [13,14]. Another crucial aspect of photon-counting readout is its potential to design signal-processing electronics that remain unaffected by fluctuations in the dark current generated within the semiconductor sensor. This feature becomes paramount when dealing with high-energy photon detectors based on high-density compound semiconductors like cadmium telluride or gallium arsenide, which suffer from strong flux-dependent sensor leakage [15–17].

Nevertheless, despite the prominence of photon-counting hybrid pixel technology, notably the state-of-the-art Dectris EIGER2 detector [18] that is used across various synchrotron applications, its performance is constrained by pulse pile-up [19]. As the average photon flux per pixel approaches a certain X-ray hit rate, the pulse discrimination circuitry starts missing counts, leading to pile-up counting losses in the detector. For instance, with the Dectris EIGER2 detector, when the flux per pixel reaches a few million photon hits per second, the pile-up counting losses surpass 10% of the average incident hit rate [15, 20].

High dynamic range charge-integrating hybrid pixel detectors developed over the last decade could in principle overcome this pile-up limitation. These detectors operate by integrating the charge coming from a sensor during a very short time window for which the contribution resulting from the integration of the sensor leakage current is close to negligible. This makes them very well suited for single-pulse measurements at X-ray free-electron lasers for instance [21,22], especially at lower X-ray energies where silicon still has sufficient stopping power. However, these devices lack the versatility required for applications at storage rings, where the duration of the integration intervals, the acquisition duty cycle and the operation conditions may vary considerably from experiment to experiment. In addition, there are presently no commercially-available integrating detector using a high-density sensor.

There is clearly a major limitation of existing detectors, preventing the efficient use of new generation of synchrotrons. To address this limitation, two distinct strategies are under exploration at the ESRF as well as other facilities. The first strategy involves developing novel photon-counting detectors capable of handling count rates up to two orders of magnitude higher, such as the SPHIRD detector [23, 24]. The second strategy entails implementing novel charge-integrating detectors with time-resolved capabilities, specifically designed for operation at high photon energies within storage rings. This manuscript focuses on the latter.

### 1.1.4 Target specifications

As mentioned previously, the increased X-ray brilliance in the 30–100 keV energy range is desirable for users in the synchrotron community as it facilitates high-energy diffraction experiments. The ESRF-EBS can deliver in a single bunch tens of thousands of monochromatic X-ray photons per $mm^2$, with each bunch being intense enough to generate a high-contrast diffraction pattern on the detector. Shortening the time resolution to sub-microsecond levels while still keeping a very high dynamic range is key to perform novel single-bunch time-resolved X-ray diffraction experiments and follow irreversible processes.

To fully exploit the upgraded source, an ideal detector should have the versatility to manage the different electron filling patterns used at the ESRF, described by Figure 1.3. This includes the possibility to process individually every bunch of the 16-bunch mode, in which X-ray photons are emitted in bunches separated by 176 ns, but also to support the very high flux output of the quasi-continuous 7/8+1 filling mode.

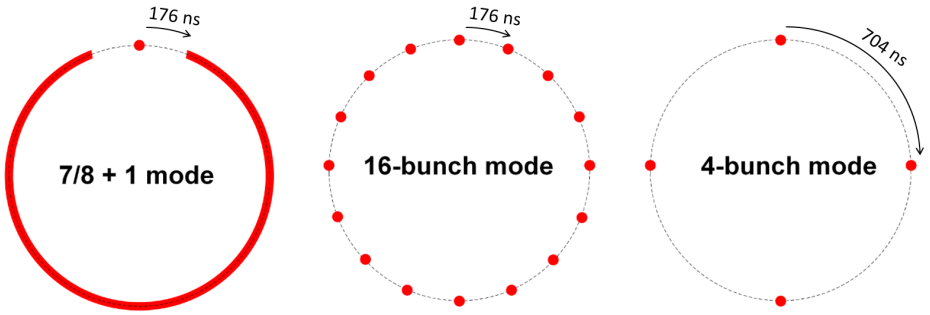



**Figure 1.3.** Electron filling patterns commonly used at the ESRF, represented in red over the dashed storage ring. Red lines indicate contiguous electron bunches and red dots single bunches. The orbit period is 2.82 µs, meaning that the bunch spacing in 16-bunch mode is 176 ns. From [25].

To summarise, an ideal detector should have the following features, also presented in Table 1.1:

- A high-energy range of 30–100 keV. This entails the use of a high-density compound such as cadmium telluride (CdTe), cadmium zinc telluride (CdZnTe), or to a lesser extent gallium arsenide (GaAs).

- A relatively large pixel size of 100–200 µm, with possible $2 \times 2$ pixel hardware binning. The pixel size requirements are quite relaxed for such a scattering detector when compared to high-resolution X-ray imaging cameras, on the order of 1 µm [26, 27].

- A time resolution of 176 ns, which corresponds to an internal frame rate higher than 5.68 MHz, to be able to cope with the most demanding 16-bunch pulsed mode operation. This also requires frame storage cells, as reading out frames at 5.68 MHz is not technically feasible.
- A very high dynamic range, from detecting single photons to reaching 250 ph/pulse/pixel in pulsed mode operation and 1500 Mcps/pixel in continuous operation.

**Table 1.1.** Target detector specifications

| **Main features** | **Target** |
|---|---|
| **Sensor** | |
| Sensor material | Cd(Zn)Te, GaAs |
| Energy range | 30–100 keV |
| Pixel size | 100–200 µm |
| Noise | single-photon sensitivity |
| **Pulsed mode operation** | *16-bunch mode* |
| Maximum photon flux | $\sim$ 250 ph/pulse/pixel |
| Cycle dead time | $\leq$ 170 ns |
| Internal frame rate | $\geq$ 5.68 MHz (storage cells required) |
| **Continuous mode operation** | *7/8+1 mode* |
| Maximum photon flux | $\sim$ 1500 Mcps/pixel |
| Cycle dead time | $\leq$ 170 ns |

The following sections compare the different detector technologies and provide a state of the art, before presenting the XIDer detector and its novel readout scheme.

## 1.2 Hybrid pixel semiconductor detection

Several technologies enable the direct or indirect detection of X-ray photons, the most important being monolithic detectors, hybrid pixel detectors, and scintillation cameras.

Monolithic pixel detectors, which include CMOS Monolithic Active Pixel Sensors (MAPS) [28] such as Percival [29] and CITIUS [30], are silicon-based and can be immediately ruled out due to the poor absorption efficiency of silicon at hard X-ray energies (more detail given in Subsection 1.2.1).

Another option is indirect detection using scintillators, coupled with a silicon detector. There are several potential scintillating material candidates, including for

instance thallium-activated cesium iodide (CsI(Tl)) and its high light emission yield relative to most other materials. Still, the light output of CsI(Tl) of 54 ph/keV (with the maximum of the broad emission situated at 550 nm [31,32]) is likely not sufficient to have a single X-ray photon resolution when coupled to a fast silicon detector. Interestingly, single-photon sensitivity for X-ray energies above 20 keV was demonstrated with the scintillating material Terbium-doped gadolinium oxysulfide ($Gd_2O_2S$:Tb, or GOS:Tb) [33], which has an even higher light output than CsI(Tl) [34], but has a quite slow decay time of around 600 µs [33, 35]. Essentially all scintillating materials have a primary decay time higher than approximately 1 µs, which prevent their use in the ultrafast time-revolved experiments envisaged. Another limitation of scintillation-based indirect detection is that it relies on the coupling with a sCMOS camera, and commercial scientific CMOS cameras are imaging detectors that are not tailored for fast time-resolved needs, being limited to frame rates on the order of 100 Hz [36].

The detection can instead be done with a high-Z semiconductor sensor that is hybridised to a readout application-specific integrated circuit (ASIC) to form a hybrid pixel detector, as depicted by Figure 1.4. The electric field needed to move the photoelectrons towards the bottom electrode is created by applying a high-voltage bias between the top and bottom electrodes.

In any case, research and development of fast, heavily-parallelised readout electronics is necessary to meet the time resolution requirements of high-energy synchrotron experimenters. Designing an hybrid pixel detector with custom readout electronics associated to a high-Z semiconductor sensor is the most sensible approach.

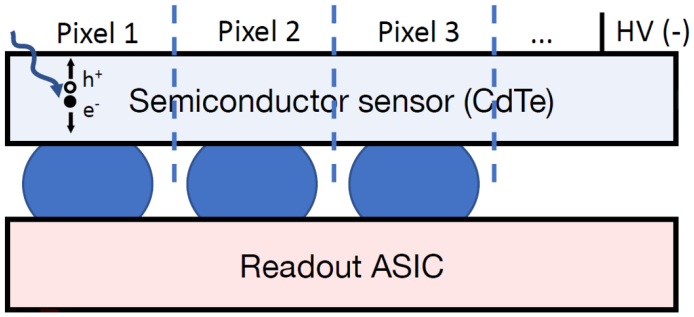



**Figure 1.4.** Schematic of a CdTe-based hybrid pixel detector, in which a readout ASIC is bonded to a pixelated CdTe sensor. The sensor is biased by applying a voltage between electrodes. Photoelectrons generated via the photoelectric effect drift towards the pixelated bottom electrode and the electric signal from each pixel is read out by the ASIC.

### 1.2.1 Overview on available high-Z sensor materials

Light detection with semiconductors relies on the photoelectric effect, transforming radiant energy to electric energy, which can then be processed by electronic components. During this phenomenon, an incident above-bandgap photon is absorbed by a semiconductor material, promoting bound electrons to the conduction band. This creates photoelectrons-hole pairs, which are free charge carriers that respond to the surrounding electric field and can be collected by electrodes. For a photon of energy $E$ incident on a material of atomic number $Z$, the photoemission cross section can be approximated locally by $\sigma = \text{const} \cdot Z^n E^{-3}$, where n is a number varying between 4 and 5 [37]. From this relation is inferred that a material with higher atomic number will more easily stop light and that photons with higher energies are less likely to be absorbed via the photoelectric effect.

The Lambert's law states that the probability of finding a particle incident on a material at depth $x$ is given by $P(x) = \frac{1}{\lambda}\, e^{-x/\lambda}$. The absorption length $\lambda$ is the distance into the material where the intensity of the incident photon beam has dropped to $1/e \approx 63\%$, and can be used to characterise the light stopping power of a material. Silicon, the most commonly used semiconductor, has very low stopping power at high photon energies: Figure 1.5 shows that silicon has an absorption length higher than 1 cm for photon energies above 50 keV. A high-density material is needed to more efficiently detect hard X-ray photons at these energies. A well-established material with a good absorption efficiency in the 30-100 keV energy range of interest is cadmium telluride (CdTe). CdTe has an average atomic number of 50, compared to silicon whose atomic number is 14. Figure 1.5 shows that the absorption length of CdTe remains under the millimetre for energies below approximately 100 keV. Gallium arsenide (GaAs), with $Z_{avg} = 32$, is also another good candidate for hard X-ray detection, but its stopping power is still lacking when approaching photon energies of 100 keV.

From Figure 1.5 can also be observed a sudden increase in absorption of the CdTe material around 26.7 keV and 31.9 keV. These two energy levels are the K-edges of cadmium and tellurium respectively, which correspond to the binding energy of the innermost electron shell (or K-shell) of the Cd and Te atoms. With above K-edge illumination, an incident photon can then eject a K-shell electron via the photoelectric effect. It should be noted that the relaxation of this excited electron to a lower energy state may happen through the emission of a photon in a process called fluorescence. This photon re-emission process occurs with high probability when the incident photon energy is closely above the K-edge: for instance, the fluorescence quantum yield is an estimated 85% directly above the Cd K-edge [38]. Fluorescence photons can be of various energies depending on the non-radiative decay processes between excited

and ground state, but are always lower than the incident photon energy. Concerning cadmium fluorescence, the most likely K-edge fluorescence photon energy is 23.174 keV with 53.6% radiative rate [38]. The fluorescence photons can be re-absorbed inside the CdTe sensor material, which has an absorption length on the order of 100 µm at these energies. Since fluorescence photons are isotropically-emitted, they also worsen the theoretical spatial resolution reachable in a CdTe detector.

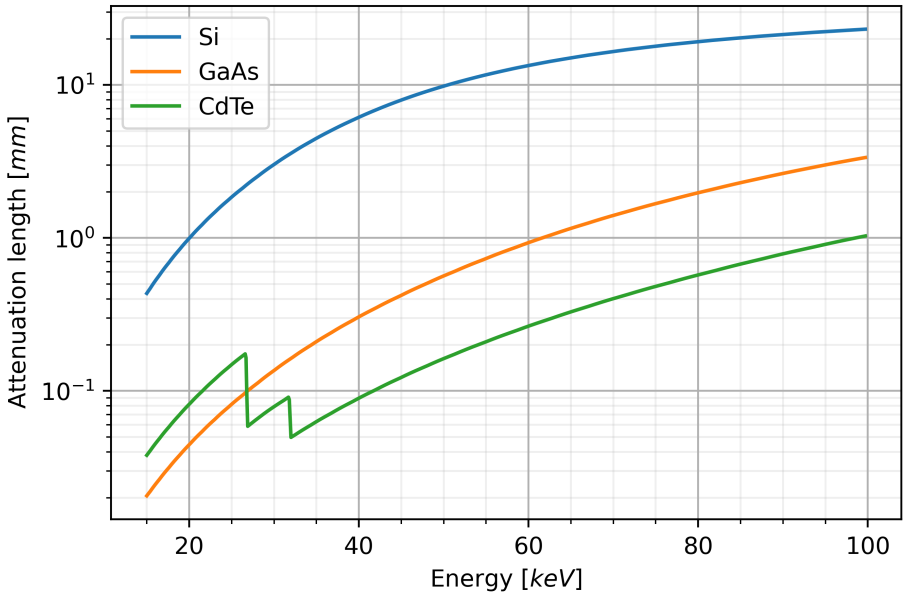



**Figure 1.5.** Absorption length of silicon (Si), gallium arsenide (GaAs), and cadmium telluride (CdTe) as a function of incident photon energy. Calculated with data from [39].

To have a good detective quantum efficiency, the sensor thickness should be on the order of the absorption length: at 100 keV, the absorption length is approximately 1 mm for CdTe, 3 mm for GaAs, and 2 cm for Si. The photoelectrons generated by the absorption of an X-ray photon in the bulk of the sensor material diffuse during their drift through the sensor along the direction of the externally-imposed electric field. From a point-like absorption event, the electrons reaching the collecting electrode are dispersed with a 2D Gaussian cross-section. After drifting through 1 mm of CdTe, the typical standard deviation $\sigma_{x,y}$ of the charge cloud is on the order of 10 to 15 µm, and charge may be shared among several pixels. A sensor thickness of several centimetres would produce much larger charge clouds, which, in addition to being very impractical, is incompatible with the spatial resolution requirements. Therefore, silicon cannot be envisaged for the detection of such hard X-rays.

### 1.2.2 Focus on high-density compound semiconductor issues

Only high-Z semiconductor sensors are considered in this work, as they provide good absorption efficiency for hard X-ray energies. The envisaged high-Z candidate semiconductors, Cd(Zn)Te and GaAs, all share similar issues linked to crystallographic defects introduced during the growth process. Ohmic and Schottky electrical contact technologies are still under investigation by the scientific community to mitigate these issues, and notably sensor leakage [40, 41]. To present these high-Z sensor imperfections, Cd(Zn)Te is taken as a reference, being the most studied in the literature as well as in the framework of the XIDer project.

Cd(Zn)Te crystals are binary (or ternary) compounds, and impurities or imperfections in the growth process happen, typically Cd/Te vacancies or extra Cd/Te ions in the crystalline structure. Because of these impurities, high-Z sensors are affected by two main issues, polarisation and aftersignal, with different degrees of intensity depending on the material and contact technology. Polarisation is a change in the internal electric field, which can result in a deterioration of the charge collection efficiency [42–44]. At the extreme, the electric field collapses and charge carriers are no longer collected. Aftersignal, also known as afterglow, is the release of charge after the incident X-ray illumination has stopped.

To understand these two effects, the notion of charge trapping and detrapping must be introduced. When a Cd(Zn)Te sensor is biased, a strong electric field is created inside the sensor bulk, and the charge carriers generated by incident X-rays can be trapped in the crystal impurities. Free electrons from the conduction band are said to be trapped in donor states, and free holes from the valence band in acceptor states. A trap centre is characterised by its trapping rate $\Lambda^{\Downarrow}$ and its detrapping rate $\Lambda^{\Uparrow}$. Taking the example of one donor state $D$ (see Figure 1.6) with the notations of [45] and [46], the electrons trapping and detrapping rates are given by Formulas 1.1 and 1.2.

$$\Lambda_D^{\Downarrow} = \sigma_D \, \theta_n \, (N_D - n_D) \tag{1.1}$$

$$\Lambda_D^{\Uparrow} = \nu_D \, e^{-\frac{E_C - E_D}{kT}} \tag{1.2}$$

In these equations, $\sigma_D$ is the capture cross section of the donor, $\theta_n$ is the electron thermal velocity, $N_D$ and $n_D$ are respectively the concentration of defects and the concentration of electrons already trapped within the donor state. $\nu_D$ is the electron escape frequency (independent of carrier concentrations), $E_C$ and $E_D$ are the energies of the conduction band and of the donor state, $k$ is the Boltzmann constant, and $T$ is the electronic temperature. The energy level of a trap centre is placed inside

the semiconductor band gap between the valence and conduction band. As depicted by Figure 1.6, shallow traps have their energy level close to either the valence or the conduction band, with trapped electrons more likely to be close to the conduction band and trapped holes close to the valence band. Eventually, the trapped charge carriers are released (detrapped), and the deeper the trap centres, *i.e.* the farther from the valence or conduction bands, the larger the detrapping time constant is. Over fifty trap levels have been referenced for CdTe, with contradicting measurements [47], and some papers mentioning « considerable controversy » on the topic [42]. One can assume a continuum of trap energy levels [42, 45]. Aftersignal is understood as the detrapping in time of trapped charge carriers, with time constants spanning from a few nanoseconds to several seconds. Aftersignal adds to the overall leakage current that can be measured at the electrodes of a biased sensor, with a contribution that depends non-linearly and rather unpredictably on the past irradiation history (X-ray energy, dose, time of irradiation).

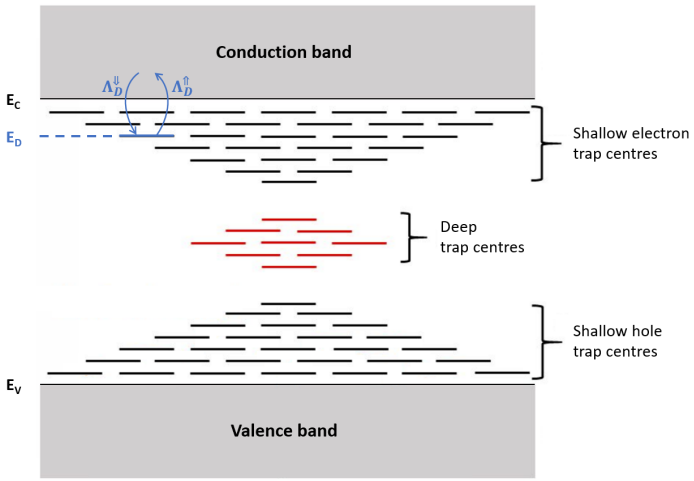
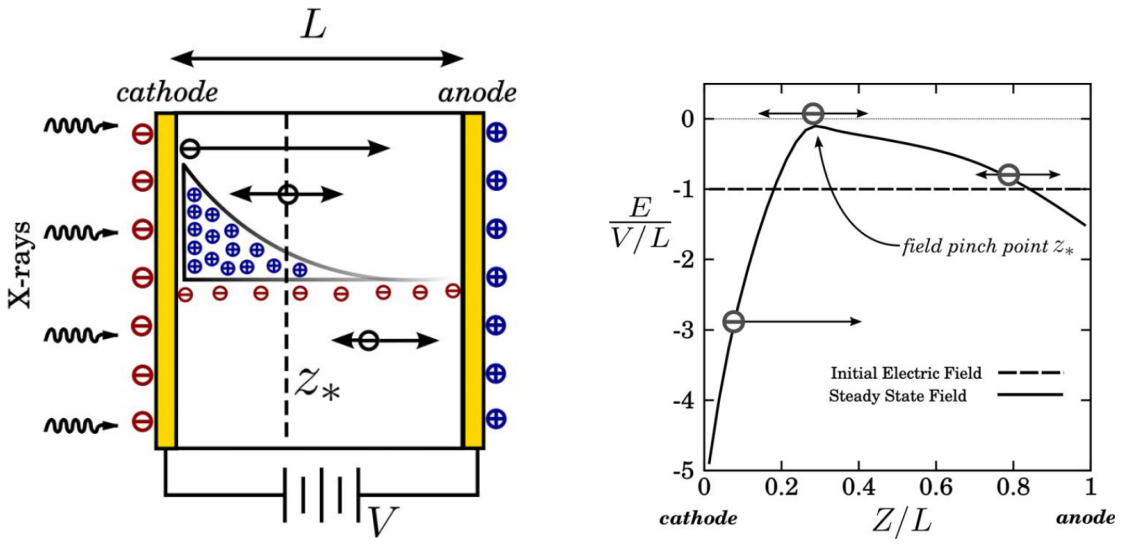



**Figure 1.6.** Schematic of electron and hole trap levels in the band gap of a semiconductor. Shallow electron and shallow hole traps have energy levels close to the conduction and valence bands respectively, while deep traps are closer to the mid gap. Image adapted from [48].

Trapping rates depend on the concentration of the charge carrier inside the sensor bulk. Since Cd(Zn)Te, commonly with the other high-Z materials, has wildly different electron and hole mobility-lifetime product values ($\mu_e\tau_e = 2.7 \times 10^{-3}\,\mathrm{cm}^2/\mathrm{V}$ and $\mu_h\tau_h = 1.8 \times 10^{-4}\,\mathrm{cm}^2/\mathrm{V}$ in CdTe at room temperature, see [49]), holes have a higher concentration inside the biased sensor material and are significantly more likely to be trapped. This causes an imbalance between the spatial distributions of trapped electrons and trapped holes inside the sensor, which disrupts the internal electric field.

Considering high-flux X-ray cathode irradiation of a Cd(Zn)Te sensor, trapped holes and electrons are distributed like depicted in Figure 1.7a. Electron mobility

being high, the electrons in the sensor are trapped quasi-uniformly its depth. On the contrary, hole mobility being low, holes are trapped in larger numbers close to the cathode, with an exponential distribution across the sensor depth closely following the exponential interaction profile of the X-ray photons in the material [45]. Figure 1.7b shows electric field profiles inside the sensor bulk, where the dashed line is the ideal unperturbed electric field and the solid line is the profile resulting from the simulated charge densities during high-flux irradiation depicted in Figure 1.7a. The electric field is affected significantly by the X-ray irradiation, and notably, a field pinch point is observed inside the bulk, for which the strength of the electric field is reduced to a fraction of its unperturbed value. The presence of this pinch point is explained by the gradient in the trapped hole distribution inside the sensor, and results in a drop of the charge collection efficiency in the phenomenon called flux-induced polarisation. A more detailed analysis, which is not in the scope of this manuscript, is given in [45].




**(a)** Representation of charge distributions **(b)** Electric field profile

**Figure 1.7.** Simulation results of a CdZnTe sensor under high-flux cathode irradiation: charge distributions and corresponding steady state profile of the electric field strength. Images from [45].

These considerations were made for a Cd(Zn)Te sensor with Ohmic metal-semiconductor contacts, through which charges can freely flow. Another type of contact is the Schottky contact: a potential barrier (the Schottky barrier height) between metal and semiconductor blocks charge transport in a diode-like fashion. For this reason, CdTe sensors with a Schottky anode and an Ohmic cathode contacts have the advantage to have a lowered leakage current. However, these sensors suffer more from polarisation effects, rendering their time response very unstable [50, 51].

Recently, a novel material with better hole transport properties has emerged: high-

flux capable cadmium zinc telluride (HF-CdZnTe or HF-CZT). This novel material has a hole mobility-lifetime product $\mu_h\tau_h = 2.9\times10^{-4}\,\mathrm{cm}^2/\mathrm{V}$ that is 50% higher with respect to CdTe and at least ten times higher with respect to standard CdZnTe [52]. As previously explained, this should reduce the impact of polarisation effects on the sensor, making it a particularly promising material [53].

Although Schottky CdTe sensors were also investigated, this work focuses on detector prototypes with Ohmic CdTe and (Ohmic) high-flux CdZnTe sensors, materials that were deemed most promising.

### 1.2.3 Photon-counting readout

Hybrid pixel detectors are conventionally equipped with either a photon-counting readout scheme or a charge-integrating readout scheme. Both have their advantages and limitations, detailed in the following two subsections.

In a photon-counting detector, the charge signal incoming from a photon is first amplified, typically with the use of a charge-sensitive preamplifier, which converts the charge pulse into a voltage step with amplitude proportional to the incident charge. This voltage step is then fed to a pulse shaper to produce a fast rise-time pulse, whose level is compared to one or several user-defined threshold(s) [54, 55].

Figure 1.8 shows a schematic of the main elements of a photon-counting detector. Depending on the application, the shaped pulses can be processed in different ways. A single-threshold discriminator can be used to infer the observation of a single monochromatic photon of a certain energy: when above this threshold, a digital counter is incremented. For spectroscopy, the processing can also be done with an analogue-to-digital converter (ADC) to measure the detected signal amplitude with a resolution of n bits. Time of occurrence can also be retrieved using a time-to-digital converter for timing measurements.

When coupled to a high-Z sensor, state-of-the-art photon-counting devices such as the Dectris EIGER2 [18] have single-photon sensitivity in the 30–100 keV energy range, and work essentially noise-free owing to signal discrimination. The signal processing electronics can be designed to be insensitive to leakage current generated by the sensor material, which is particularly significant for the case of CdTe. Moreover, like in the EIGER2 CdTe detector, a two-threshold comparator can be used to discriminate fluorescence photons and higher X-ray harmonics from photons of the operating wavelength.

However, since photons incident on such devices are immediately processed with amplifiers of finite bandwidth, two photons arriving too closely in time will pile up and be counted as a single photon by the pulse discriminator circuitry. This is known

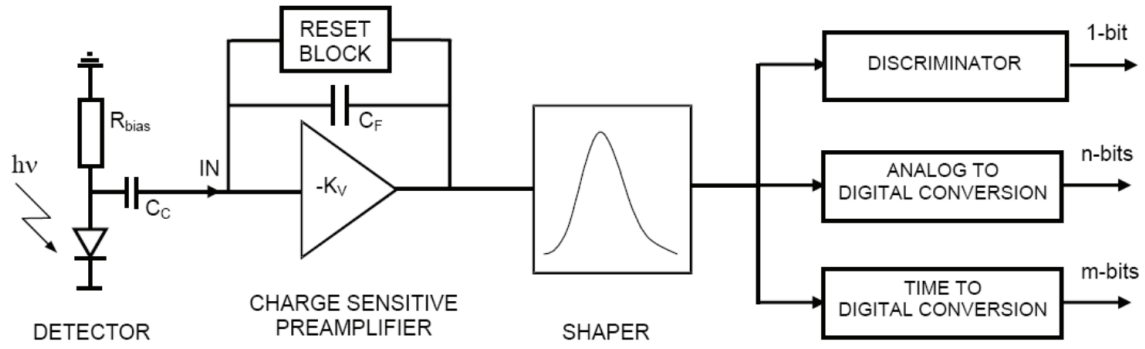



**Figure 1.8.** Building blocks of the pixel front-end electronics in a typical photon-counting detector. From [55].

as paralysation of the counting circuit, which limits the maximum count rate per pixel and produces pile-up counting losses [56–59]. For earlier iterations of photon-counting detectors, like the Dectris PILATUS2, pile-up would completely paralyse the counting after a flux of typically $2 \times 10^6$ ph/s/pixel [20]: an increase in incident flux after that point results in a decrease of measured flux. More recent iterations, such as the PILATUS3 or EIGER/EIGER2 detectors, have the capability of instant retriggering: following each count, the pulse is reevaluated after an adjustable dead time interval and the time-over-threshold of piled-up signals is measured. This allows for non-paralysable counting and increased high-rate performances [20, 58, 60]. With current state-of-the-art photon-counting detectors, pile-up counting losses start being significant when the incident flux is only a few millions photons per second per pixel, but can be compensated with a count rate correction within a certain range. For example, the maximum count rate quoted by the Dectris EIGER2 X/XE CdTe is $10^7$ ph/s/pixel [18], still two orders of magnitude lower than the output flux of ESRF-EBS beamlines. Research and development of faster front-end readout electronics with in-pixel pile-up compensation, as well as decreased pixel pitches can increase this maximum count rate, but it seems unlikely that the two orders of magnitude gap is bridged in the near future. Consequently, the new generation of synchrotron sources cannot be fully exploited by these photon-counting detectors.

### 1.2.4 Conventional charge-integrating readout

While photon-counting devices treat photons one at a time, charge-integrating devices process the total incoming signal, including noise and sensor leakage, during a user-defined integration time frame [54]. During this integration window, incident charge is integrated by the feedback capacitor of a charge-sensitive amplifier. At the end of

the integration window, the preamplifier voltage output level is read out and the stage is reset.

In such schemes, the dynamic range is limited by how many equivalent photons the feedback capacitor can store during the minimal integration frame. As shown in Figure 1.9, a common strategy to push the dynamic range is to have multiple feedback capacitors with sizes spanning over several orders of magnitude. Then, a low-gain capacitor can be used under high incident photon fluxes, while the highest-gain capacitor will be favoured for low fluxes to retain single-photon sensitivity. In some older detectors, like the CSPAD (Cornell–SLAC Pixel Array Detector [61, 62]), every pixel can be programmed in either low-gain or high-gain mode in a scheme that can be called programmable gain switching. Most current charge-integrating detectors implement in-pixel dynamic gain switching: each pixel front-end is able to automatically change the gain mode by switching additional feedback capacitance. This is the case of the ePix10k [61,63], which replaced the CSPAD detector, as well as the AGIPD (Adaptative Gain Integrating Pixel Detector [22,64,65]) and JUNGFRAU [66–69] detectors, which were developed primarily for free-electron lasers notably at the Paul Scherrer Institute. A correlated double-sampling (CDS) stage is often used to reduce low-frequency noise components and reset switch noise when in high-gain mode [61, 64, 67].

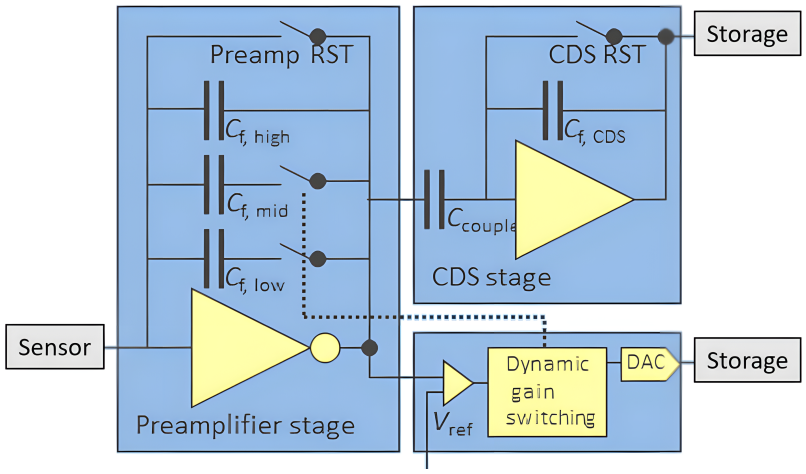



**Figure 1.9.** Building blocks of the pixel front-end electronics in a charge-integrating detector with dynamic gain switching. Adapted from AGIPD readout ASIC channel [64].

Detectors like JUNGFRAU or ePix10k are very well suited for single-pulse measurements at X-ray free-electron lasers (XFEL) [63,67]. However, they lack the necessary flexibility to be used for high-energy experiments in storage rings where integration windows and operating conditions can significantly vary between experiments. Indeed, as they use three-way gain switching, they require the calibration of 3 gains

and 3 offsets (called pedestals), with these offsets being determined by collecting dark images before each new measurement. After each acquisition, the analogue data are digitised off-chip by high-resolution ADCs, and are then gain and pedestal corrected. This back-end processing is a lengthy and computationally-intensive operation, which in the case of XFEL applications can be performed in the 10–100 ms gaps between pulse trains but is a hindrance to many synchrotron applications requiring nearly 100% duty cycle [54]. Moreover, the significant leakage current in high-Z sensors poses a real challenge for conventional charge-integrating detectors. As the integration interval increases, the performance of these systems significantly degrades, rendering them impractical.

### 1.2.5 State of the art summary

This subsection aims to summarise the main features of commonly-used state-of-the-art hybrid pixel X-ray detectors that are most representative and suited for high-energy high-dynamic-range diffraction experiments at synchrotron facilities. Table 1.2 compares the characteristics of photon-counting technologies EIGER2, Medipix3 and UFXC32k (Ultra Fast X-Ray Chip with 32 k channels), while Table 1.3 compares charge-integrating technologies JUNGFRAU, ePix10k and MM-PAD 2.1 (Mixed-Mode Pixel Array Detector). Detectors such as LPD (Large Pixel Detector [70, 71]), DSSC (DEPMOS Sensor with Signal Compression [72, 73]), and AGIPD [64] were made specifically for FEL applications and are thus not considered here. Were also left out of the tables detector systems still under early development such as Medipix4 [74, 75] and Timepix4 [76–79], as well as detectors aimed at spectroscopic applications (e.g. HEXITEC MHz [80, 81]).

All three photon-counting systems compared in Table 1.2 have similar features: a maximum count rate of approximately 1 billion photon per pixel per $mm^2$, a noise sufficiently low to have essentially noise-free detection at the desired X-ray energies, and two independent thresholds. When these two thresholds are set at the same level, there can be a continuous readout at kHz frequencies by reading out alternatively the two discriminator stages with a minimal $\sim$100 ns dead time. As for the described charge-integrating systems, JUNGFRAU and ePix10k are quite similar as they both utilise three-way automatic gain switching and the analogue signal is digitised by high-resolution ADCs and processed off-chip. The upgraded MM-PAD 2.1 (still in development) has a different strategy employing charge removal to digitise the coarse part of the signal, allowing to reach a much higher dynamic range, at the cost of a vastly increased electronic noise, rendering single-photon sensitivity impossible at lower photon energies.

**Table 1.2.** Comparison table of state-of-the-art photon-counting technologies

| | **EIGER2** [18] | **Medipix3** [13, 82] | **UFXC32k** [14, 83–85] |
|---|---|---|---|
| **Developer** | Dectris | Medipix collaboration (CERN, DESY, ESRF...) | AGH University of Science and Technology |
| **Pixel pitch** | 75 µm | 55 µm or 110 µm | 75 µm |
| **Thresholds** | 2 | 2 | 2 |
| **Max. count rate** | $1.7 \times 10^9$ ph/s/mm$^2$ | $0.8 \times 10^9$ ph/s/mm$^2$ | $\sim 10^9$ ph/s/mm$^2$ |
| **Frame rate** | 4.5 kHz (8-bit)<br>2.25 kHz (16-bit) | 2 kHz (12-bit)<br>1 kHz (24-bit) | 6 kHz (8-bit)<br>3.5 kHz (14-bit) |
| **Readout** | Continuous<br>(100 ns dead time) | Continuous<br>(700 ns dead time) | Continuous<br>(85 ns dead time) |
| **Noise (rms)** | 70 e$^-$ | 80 e$^-$ | 123 e$^-$ |

**Table 1.3.** Comparison table of state-of-the-art charge-integrating technologies

| | **JUNGFRAU** [66–69] | **ePix10k** [61, 63, 86] | **MM-PAD 2.1** [87, 88] |
|---|---|---|---|
| **Developer** | PSI | SLAC | Cornell University |
| **Pixel pitch** | 75 µm | 100 µm | 150 µm |
| **Gain switching** | Automatic 3-way | Automatic 3-way | Automatic 2-way |
| **Dynamic range** | $10^4$ ph/frame/px<br>@ 12 keV | $10^4$ ph/frame/px<br>@ 8 keV | $10^7$ ph/frame/px<br>@ 20 keV |
| **Frame rate** | Up to 2.4 kHz | Up to 1 kHz | 10 kHz |
| **Readout** | Digitised and processed off-chip | Digitised and processed off-chip | Hybrid digitisation (charge removal+residual) |
| **Noise (rms)** | 50 e$^-$ | 67 e$^-$ | 840 e$^-$ |

In most synchrotron applications, photon-counting systems will be preferred for their dead-time-free, noise-free and leakage-independent operation. However, currently, charge-integrating detectors are the only choice when fluxes above $10^9$ ph/s/mm$^2$ are needed, although lacking versatility and good management of sensor leakage.

## 1.3 The XIDer detector

With the user expectations for monochromatic high-energy time-resolved diffraction experiments detailed in Section 1.1 in mind, the ESRF started the XIDer project. XIDer stands for X-ray Integrating Detector: it is a charge-integrating hybrid pixel detector, developed in collaboration with Heidelberg University for their expertise in readout chip design, while the ESRF dealt with sensor design and procurement, system specification and evaluation. It employs a novel charge-integrating readout scheme called incremental digital integration, designed to have a high dynamic range

and a high duty cycle operation, and handle non-constant leakage currents from high-Z compound semiconductor sensors [25].

### 1.3.1 A novel readout: incremental digital integration

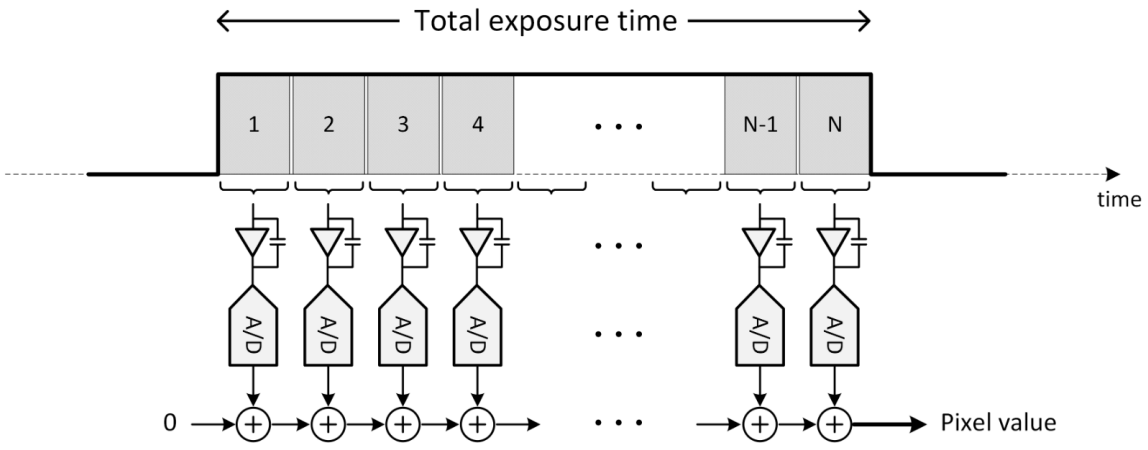


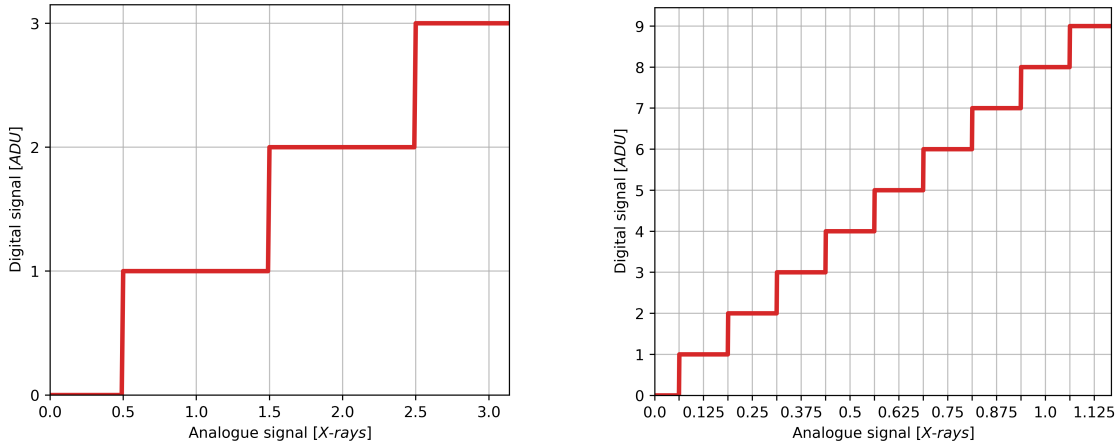

**Figure 1.10.** The incremental digital integration readout scheme: the concept is to slice the total exposure time into N subsequent subframes, which are each integrated, digitised, and finally accumulated or stored on the per-pixel level. From [25].

Figure 1.10 shows a schematic of the basic principle of the incremental digital integration readout scheme. This charge-integrating scheme is based on the subdivision of the total frame of exposure into N subsequent intervals of equal duration (subframes), typically on the microsecond time scale. During each of these subframes, the detected signal is individually integrated by a charge-sensitive amplifier and digitised. Sequentially, the N digitised values are summed to produce the final value corresponding to the total frame. Alternatively for fast time-resolved experiments, the digitised values can be individually stored to reach a sub-microsecond time resolution.

The digitisation process is performed by uniform mid-tread analogue-to-digital conversion, which includes signal discrimination: a signal integrated over a subframe that is below threshold is digitised to 0 ADU (analogue-to-digital unit) and does not contribute to the final accumulated signal. Low levels of signal can then be discarded, allowing for noise-free operation, assuming that noise stays below threshold. Because of the quantum nature of the X-ray photon source, the logical approach is to consider a quantiser with a quantisation step size matching the amplitude of a single X-ray photon at the desired energy: the least significant bit (LSB) of the digitisation process is 1 ph. It is reminded that XIDer is intended to be used with a mono-energetic X-ray source only. In this way, the transfer function of the corresponding analogue-to-digital converter (ADC) is given by Figure 1.11a, with an implicit discrimination threshold

set at 0.5 LSB, *i.e.* the half-photon level, ensuring that the quantisation residual error is zero in average. The readout then mimics the behaviour of a photon-counting system.

Instead of choosing an LSB of 1 ph, whereas a higher LSB would not preserve single photon resolution (nor single photon sensitivity), a possibility is to choose an LSB matching a specific fraction of a single photon signal. This can be useful to gain information about partial charge collection or spatial charge sharing. For instance, Figure 1.11b shows the transfer function of an ADC with an LSB of 1/8 ph, for which an analogue signal with amplitude corresponding to a single photon is converted to the digital value of 8 ADU. In this example, the discrimination threshold is set to the implicit mid-tread quantiser value of 0.5 LSB, here 1/16 ph, although one could think to set this threshold to a higher value: a discrimination threshold desired at 0.25 ph would have a dedicated logic discard and not accumulate digitised values below 2 ADU.




**(a)** Quantiser with LSB = 1 ph

**(b)** Quantiser with LSB = 1/8 ph

**Figure 1.11.** Transfer functions of uniform mid-tread analogue-to-digital converters, with a least significant bit (LSB) equal to 1 ph for Graph (a) and 1/8 ph for Graph (b).

Since digital integration is a charge-integrating readout scheme, the pixel front-end electronics must be reset between subframes. The subframes are intended to be synchronised with the time structure of the synchrotron beam. As previously shown by Figure 1.3, the X-rays are usually emitted in bunches following periodic patterns with gaps lasting 176 ns or 704 ns. In order to achieve nearly 100% duty cycle, XIDer is being developed to be able to synchronise with these gaps, such that the front-ends integrate incoming signal during bunch emission and are reset during the gaps.

### 1.3.2 Advantages and foreseen challenges over state-of-the-art detectors

The incremental digital integration readout scheme benefits from signal discrimination and quantisation, preventing the accumulation of systematic residual error. Much like photon-counting devices, single photon resolution with single photon sensitivity can be achieved. If the noise contributions stay below the discrimination threshold, then noise is totally suppressed by quantisation at low fluxes. At higher fluxes, electronic noise becomes insignificant when compared to a synchrotron Poissonian fluctuations. Perhaps the main advantage of this readout scheme is its handling of leakage current contributions that are present in the considered high-Z compound semiconductor sensors. This advantage comes from short subframes: as the integration subframe is shortened to sub-microsecond durations, the leakage current integrated during that time is reduced. Should the leakage current integrated during a subframe be lower than the discrimination threshold, the readout operates free of sensor leakage contributions. After the necessary calibration procedures and trimming of the pixel front-ends, little post-processing is required to retrieve useful data from the raw detected images, especially in comparison with current conventional charge-integrating detectors. Digitisation enables fast data readout, low-latency data analysis, and on-the-fly data reduction. Owing to in-chip digital data storage, implementing rich functionalities such as like data histogramming or post-triggering options is possible [25].

Moreover, unlike photon-counting readout schemes, digital integration is capable of a high dynamic range and is not limited by pile-up. For digital integration, the dynamic range is limited by the speed and the resolution of the analogue-to-digital conversion occurring during each subframe. Here, since the integration subframe is intended to be reduced to microsecond time scales, high-resolution ADCs are not required. Indeed, the goal is for XIDer to handle fluxes reaching $10^9$ ph/s/pixel = 1000 ph/µs/pixel, for which is only needed a 10-bit ADC whereas charge-integrating detectors like JUNGFRAU or ePix10k use ADCs with resolution of 14 bits or more. The speed of an ADC should also be taken into account. Instead of performing the analogue-to-digital conversion by direct conversion at the end of the integration period, which would contribute to a dead time, the conversion can be done simultaneously with the integration using a charge removal circuitry [87]. In that scheme, a charge pump removes charge packets from the input and increments a digital counter. The maximum achievable dynamic range will then be limited mostly by the frequency of the charge pump. To further push the dynamic range of XIDer, the charge removal process is split in two pipelined stages, as shown in Figure 1.12: a coarse stage first

removes coarse charge packets, then a fine stage removes fine charge packets. Each stage increments their own lower-resolution digital counter, which must be assembled to reconstruct the final subframe value. In the XIDer prototypes presented in this work, the coarse stage removes packets of 8 ph, and the fine stage removes packets of 1 ph. In any case, the fine stage charge packet size should not be any higher than 1 ph to preserve single photon resolution.

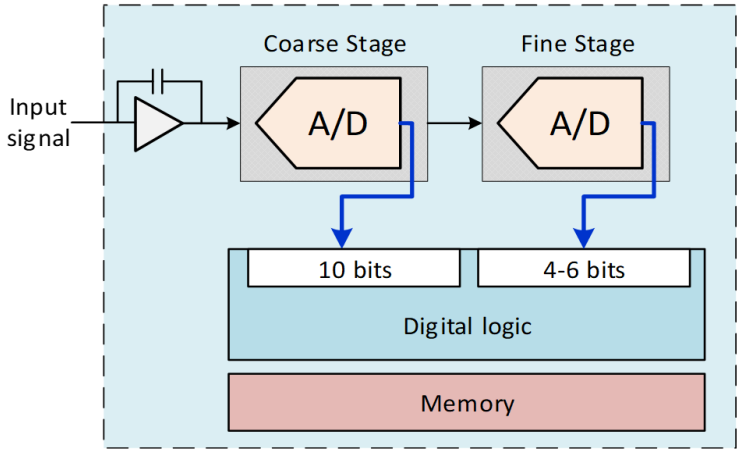



**Figure 1.12.** Schematic of a pipelined two-stage digital integration readout scheme. The input signal is processed first by the coarse stage, and then by the fine stage. A digital logic reconstructs the final value from the coarse and fine counters.

## 1.4 Outline of the manuscript

The incremental digital integration readout scheme, specially designed for high-energy time-resolved X-ray diffraction experiments, was motivated and introduced in this first Chapter 1. This detection readout is investigated and assessed using Monte Carlo simulations in the following Chapter 2, concluding on the *a priori* advantages and limitations of the readout.

Chapter 3 describes the prototype characterisation system used in this manuscript, which includes the front-end electronics implementing the digital integration readout, the hybridisation process of the integrated circuit to the high-Z sensor, as well as hardware and software necessary to the experimental characterisation system. Chapter 4 discusses the procedures that were elaborated to calibrate the hybridised detector prototype assemblies, and gives an assessment of this calibration. After that, selected XIDer prototype assemblies are experimentally characterised in Chapter 5. The electronic noise is discussed, the maximum high dynamic range and the linearity of the prototype assemblies under X-ray irradiation is measured. The aftersignal

phenonemon in the Cd(Zn)Te material is then investigated, at the same highlighting the microsecond scale fast time-resolved capabilities of the detector pixel front-end.

Finally, Chapter 6 gives a summary of the manuscript and concludes on the key achievements and next steps of the XIDer detector project.

# Chapter 2

# *A priori* investigation of incremental digital integration

Detector simulations are commonly performed to provide valuable information on the impact on detector performance of physical phenomena, such as charge diffusion or fluorescence, and system non-idealities such as electronic noise or calibration imperfections. They deepen our understanding of the mechanisms at play in an X-ray detector by finely probing the system functioning and limitations in controlled ways that experimentation cannot replicate. They are essential for the development of future detectors [89, 90], providing feedback for potential design improvements. In this context, simulation tools are used to evaluate this novel incremental digital integration (IDI) readout scheme in a Cd(Zn)Te-based pixelated X-ray detector. This chapter presents the flux- and energy-dependent behaviour of the readout, the effect of readout noise, and key simulations necessary to the comprehension of the experimental characterisation chapter, relating to Poisson distributions and to the importance of calibration. Several aspects, such as spatial resolution and noise power spectrum, were also studied in this initial investigation of the readout scheme, but are not presented in this manuscript for the sake of brevity. Parts of this chapter are directly taken from corresponding article [91] by M. Collonge *et al.*

## 2.1 Simulated performance of a digitally integrating detector using X-DECIMO

### 2.1.1 Monte Carlo simulation tool

The X-ray Detector Simulation and Modelling tool (X-DECIMO), developed at the ESRF, is used to assess the performance of a digital integration detector. X-DECIMO

is a modular Python package based on the Monte Carlo method and designed to simulate complete X-ray detection chains [92]. The main purpose of this tool is to explore novel readout schemes for future detectors like XIDer. It is organised in interconnected modules implemented as separate Python objects, as represented by Figure 2.1.

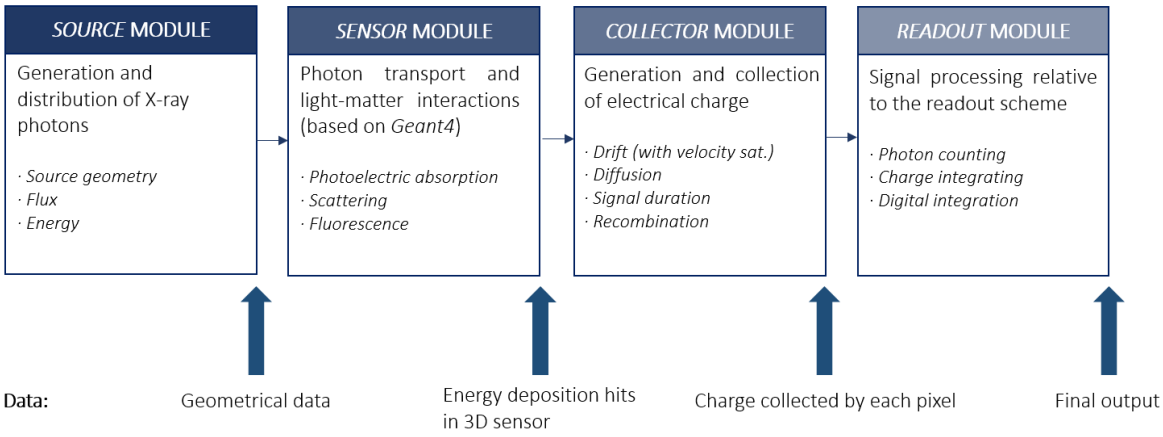



**Figure 2.1.** Building blocks of the X-DECIMO pipeline [92]. Each module is a separate Python object, controlling the Monte Carlo experiment via optimised C/C++ routines.

First, the *Source* module defines the monochromatic X-ray generation, notably the photon energy and flux, as well as the source geometry and temporal structure. By default, the emission is continuous in time and follows Poisson statistics, but can also be configured to reproduce the time structures of the ESRF.

Secondly, the *Sensor* module handles photon transport and material absorption for a given pixelated 3D sensor material. The simulation of the complex light-matter interactions at play in the material, such as fluorescence re-emission, is outsourced to the simulation toolkit Geant4, developed at CERN [93]. The result of these interactions is the 3D distribution of the energy deposited in the sensor bulk.

Thirdly, the *Collection* module generates a distribution of charge carriers from this distribution of energy deposition hits. It takes into consideration Fano noise, which is the variance in photoelectron production per incident photon in the material [94]. This module then computes the drift of electrons and holes towards the electrodes for a specified bias voltage, and determines the amount of charge collected by each pixel. The longitudinal drift driven by the electric field inside the material and the transverse thermal diffusion are both taken into account, considering velocity saturation effects. The signal duration for each charge pulse arriving on an electrode is calculated using a simplified model, and the lifetimes of the charge carriers are considered to simulate the charge recombination process. Currently, X-DECIMO implements only slabs of semiconductor sensor material, in which a stationary 1D electric field is calculated.

A complex and computationally-heavy solving of the drift-diffusion equation would be necessary to simulate how charge carrier dynamics and electric field influence each other [46]. This is however out of scope for this study and for X-DECIMO, whose focus is the investigation of readout schemes. Consequently, high-flux polarisation phenomena present in Cd(Zn)Te [44] are not simulated.

Finally, the *Readout* module performs signal processing relative to the readout scheme to be investigated, which can be a conventional charge-integrating scheme, a photon-counting scheme, or incremental digital integration.

Using this pipeline approach, the total efficiency of a detector can be represented as a multiplication of four factors, one for each of the four building blocks of Figure 2.1.

$\eta_{detector} = \eta_{source} \times \eta_{sensor} \times \eta_{collector} \times \eta_{readout}$ , with:

- $\eta_{source}$ : the source efficiency is the proportion of photons generated by the source that effectively arrive to the sensor surface. A mismatch between the source spatial distribution and the sensor lowers this efficiency. It also includes absorption in the propagation medium (*e.g.* air) during the X-ray photons travel towards the sensor.

- $\eta_{sensor}$ : the sensor efficiency is the amount of energy deposited in the 3D sensor divided by the total energy of photons incident on the sensor surface. Two main factors can lower this efficiency. The first is the transmission of the sensor, which is negligible only when the sensor thickness is much bigger than the attenuation length of the material for the given photon energy. Secondly, re-emission processes from fluorescence events provide additional losses, as fluorescence photons are isotropically-emitted and can escape the sensor volume from any side.

- $\eta_{collector}$ : the charge collection efficiency is the ratio of energy collected as charge pulses on the electrodes over the energy deposited in the sensor. An amount of charge is converted to equivalent energy using the material pair-creation energy, which for CdTe is $\epsilon_{CdTe} = 4.43\,\text{eV/pair}$ [95]. Collection losses arise from the recombination of charge carriers according to their lifetime.

- $\eta_{readout}$ : the readout efficiency corresponds to the non-linearities in the readout scheme, which appear with thresholding and digitisation.

### 2.1.2 Simulation setup

This chapter considers a 1-mm thick Ohmic CdTe sensor with a 100 µm pixel pitch under a $-500\,\text{V}$ bias voltage. Charge transport properties in CdTe are taken from [95].

Given that high-flux polarisation phenomena are not simulated, CdZnTe material would behave very similarly to CdTe material, and is not investigated.

The readout discrimination threshold is tuned at the half-photon signal level and an ideal mid-tread uniform quantiser with a least significant bit (LSB) of 1 ph is simulated for digitisation. XIDer prototypes include a pipelined coarse and fine stages in order to increase dynamic range (see Figure 1.12). Since an ideal two-stage digitisation operation is equivalent to an ideal single-stage operation, only one stage is considered in the following simulations.

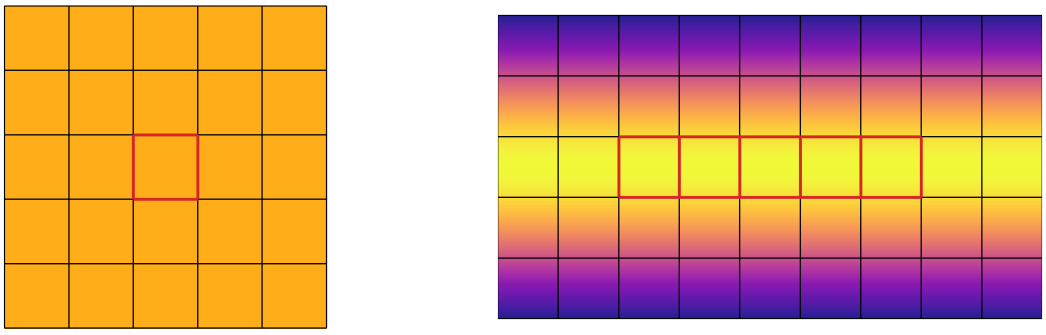
A 5×5 pixel structure and a uniform monochromatic Poissonian X-ray source are first simulated. The use of an ideal uniform source is key to understanding the behaviour of the system in detail, but is not representative of the use case since a real experiment would illuminate the detector with a diffraction pattern. To more closely emulate a diffraction pattern on the detector, a second non-uniform X-ray source is also considered: a Gaussian-profile line with varying standard deviation illuminating a 5×9 pixel structure. Table 2.1 summarises the essential simulation parameters used, and Figure 2.2 shows the shape of the sensors and sources considered.

**Table 2.1.** Summary table of key simulation parameters.

| **Simulation parameter** | **Value** |
|---|---|
| Source energy | 20 – 100 keV |
| Source flux | $10^{-3}$ – $10^{3}$ ph/subframe/pixel |
| Sensor material | 1 mm CdTe |
| Pixel pitch | 100 µm |
| Bias voltage | −500 V |
| Subframe duration | 2.8 µs or ∼1 ESRF orbit |
| Digitisation LSB | 1 ph |
| Digitisation threshold | 0.5 ph |

To improve simulation statistics, the source spatial distribution is set to match the sensor geometry, and the source is simulated directly in front of the sensor surface to avoid losses during the propagation of X-rays in air. The efficiency of the source is consequently not singularly evaluated, but is still implicitly considered in the calculations. To mitigate border effects, the whole finite pixel structure is illuminated but only the central pixel volume is evaluated.

Readout losses may have been propagated from losses in the material arising from physical phenomena. To have the entire picture and understand the efficiency of the digital integration readout scheme, it is important to first examine the material



**(a)** Uniform source: 5×5 pixel matrix

**(b)** Gaussian line source (centred): 5×9 pixel matrix

**Figure 2.2.** Geometry of the sensors and sources simulated in X-DECIMO. Data is extracted by averaging over the central pixel(s), outlined in red. Gaussian lines of varying location and scale are used.

efficiency: the sensor efficiency and the collection efficiency as previously defined.

The X-DECIMO simulations presented in the following sections are summarised by Table 2.2.

**Table 2.2.** Summary table of X-DECIMO simulations presented in this chapter.

| **Goal** | **Simulation run** | **Source** |
|---|---|---|
| Material efficiency vs. energy<br>See Subsection 2.1.3 | 20–100 keV | Uniform |
| Readout efficiency vs. flux<br>See Subsection 2.1.4 | • $10^{-3}$–100 ph/subf/px<br>• few energy points | Uniform |
| | | Gaussian line:<br>• position 0–50 µm<br>• scale 50–1000 µm |
| Readout efficiency vs. energy<br>See Subsection 2.1.5 | • 20–100 keV<br>• few flux points | Uniform |
| | | Gaussian line:<br>• position 0–50 µm<br>• scale 50–1000 µm |
| Output distribution statistics<br>See Subsection 2.1.6 | • $10^{-3}$–$10^{3}$ ph/subf/px<br>• 30 keV<br>• 10 µm–100 mm pitch | Uniform (size adjusted to match the sensor) |

### 2.1.3 Material performance

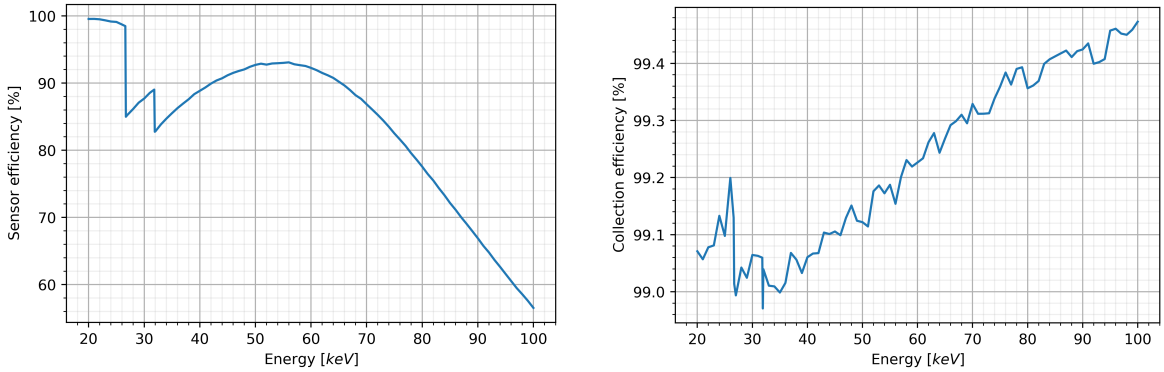
A 1-mm CdTe, 5×5 pixel matrix with 100 µm pixel pitch, irradiated under uniform X-ray illumination is simulated to investigate the material efficiency as a function of the incident photon energy.

Figure 2.3a shows the sensor efficiency in the volume above the most central pixel, defined as the ratio of the total deposited energy inside the volume over the photon energy incident on the column top surface.

Three X-ray energy ranges, linked to physical phenomena, stand out: below the 26.7 keV Cadmium K-edge, between 26.7 keV and 50 keV, and above 50 keV. Above 50 keV, the stopping power of 1 mm of CdTe starts significantly decreasing. The sensor becomes transparent to X-rays with increasing photon energy, which is the driving force explaining the drop in sensor efficiency at high energies [39]. Below 50 keV, it can be assumed that 1 mm of CdTe stops 100% of incident photons. Fluorescence appears in CdTe for incident photon energies higher than the Cadmium K-edge (26.7 keV). In this 26.7–50 keV energy range, the main cause for sensor losses is fluorescence escape, when a fluorescence photon propagates outside the sensor volume. This is highlighted in Figure 2.3a by an approximately 13% drop in sensor efficiency at the Cadmium K-edge (26.7 keV) and a further 6% drop at the Tellurium K-edge (31.9 keV). Directly above the Cd K-edge, the fluorescence quantum yield is an estimated 85% [38]. Considering the shallow depth of interaction of X-ray photons in CdTe at these energies, it is likely that some of the isotropically re-emitted fluorescence photons escape the sensor, mainly from the top of the sensor but also potentially from the sides or bottom of the sensor. Fluorescence escape becomes less likely with increasing energy as the depth of interaction is increased and the fluorescence yield decreases. Interestingly, the possible escape from the sensor sides means that the sensor efficiency is linked to the pixel position in the sensor and the spread of the illumination. The simulations shown here are for the central pixel of a limited 5×5 pixel illuminated surface, therefore the likelihood of fluorescence escape from the sides is increased with respect to a simulated wider flat field and, in turn, the losses are overestimated. Further computationally intensive simulations of a wider illuminated zone would be required for a more accurate picture in the centre of a large detector under flat field irradiation.

It should be noted that, for this energy range under the same conditions, a 1 mm CdZnTe (Cadmium Zinc Telluride) sensor was simulated to perform similarly to a 1 mm CdTe sensor, as they have the same behaviour with fluorescence at the energies of interest.

Figure 2.3b shows the collection efficiency, defined as the total energy collected as charge pulses on the central pixel electrode divided by the total energy deposited




**(a)** Sensor efficiency

**(b)** Collection efficiency

**Figure 2.3.** Simulated sensor and collection efficiencies for a 1-mm CdTe sensor under a bias voltage of −500 V, as a function of the source energy. Graph (a) shows the impact of fluorescence escape, and transmission at higher energies. Graph (b) demonstrates the influence of depth of interaction on charge transport losses.

in this central pixel column. The effects of carrier recombination can be observed, resulting in charge collection losses. The variations with photon energy are linked to the depth of interaction. Indeed, at increasing energies, the photons are absorbed deeper on average in the sensor bulk, and the generated photoelectrons have a shorter distance to travel towards the bottom electrode. At energies below $\sim$ 25 keV, when the X-rays are absorbed superficially, photoelectrons drift through the entire 1 mm thickness of CdTe, and in the process around 1% are lost to recombination.

### 2.1.4 Readout performance with flux

The digital integration readout is designed to have a high dynamic range, handling single photon resolution as well as high fluxes of billions of photons per pixel per second. Because of the use of discrimination and digitisation, this readout scheme is expected to perform differently at low and at high fluxes. Readout losses arise from the treatment of partial charge collection at the individual pixel level. The principal source of partial charge collection is spatial charge sharing, where the photoelectrons generated by the absorption of an X-ray photon diffuse during their drift through the sensor material. Partial charge collection can be due to temporal or spatial sharing, however, the following section focuses on spatial partial charge collection. From a point-like absorption event, the electrons reaching the bottom electrode are dispersed with a 2D Gaussian cross-section. After drifting through 1-mm CdTe, the typical standard deviation $\sigma_{x,y}$ of the charge cloud is 10 to 15 µm according to the performed simulations, a value that can also be derived experimentally [96]. With a 100 µm

pixel pitch, it is then likely that a non-negligible amount of electrons are shared among several pixels.

A second source of partial charge collection is fluorescence. This is particularly significant for CdTe, which starts fluorescing at photon energies above the 26.7 keV Cadmium K-edge. In this material, the fluorescence photons are typically 23-30 keV [38] and the mean free path of photons with such energies in CdTe ranges between 59 and 112 µm [39, 96], which is comparable to the 100 µm pixel pitch. Therefore, fluorescence escape (when the fluorescence photon escapes the sensor) and fluorescence redistribution (when the fluorescence photon is reabsorbed in a pixel different from the original hit) are likely.

The digital integration readout scheme involves digitisation and with it, quantisation error. This section aims to quantify quantisation error by means of simulation with respect to source flux. Quantisation error is naturally linked to how the quantiser is set up, notably the least significant bit (LSB) and threshold. Here is only considered a mid-tread quantiser that is LSB=1 ph and a threshold at 0.5 ph. To take into account only the losses from the IDI readout and not material transparency or charge collection efficiency discussed previously, the figure of merit chosen here is the readout non-linearity (RNL) error. It is defined as the efficiency of the readout with reference to the number of collected electrons, expressed as a percentage error.

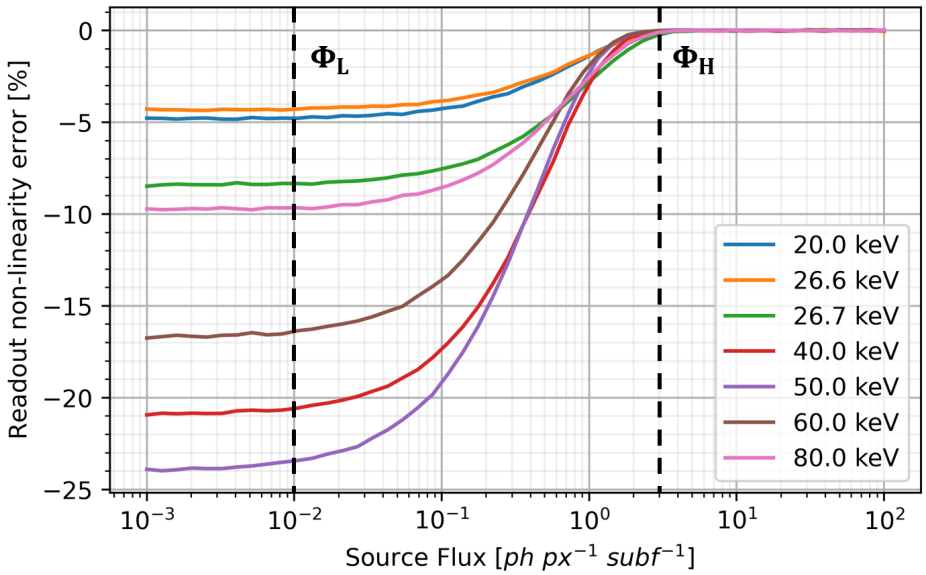



**Figure 2.4.** Simulated readout non-linearity error for a digitally integrating detector with 1-mm CdTe sensor and 100 µm pixel pitch, as a function of the source flux, under uniform illumination. Two stable regimes are observed: a low-flux regime for values below $\Phi_L$ and a high-flux regime for values above $\Phi_H$, with a transition in-between. Above $\Phi_H$, the digital integration readout records no losses for all energy points.

A 5×5 pixel matrix with 100 µm pitch, irradiated under uniform X-ray illumination, was simulated to probe the readout losses as a function of the incident photon flux. Figure 2.4 shows the readout non-linearity error of the digital integration readout as a function of source flux for the central pixel. The flux is converted to the more convenient units of photons per pixel per subframe, where the subframe duration is implicitly defined. Figure 2.4 highlights the two functional flux regimes of digital integration: a low-flux regime and a high-flux regime. The regime boundaries are located at $\Phi_L$ and $\Phi_H$ respectively, with a transition region between them. For fluxes smaller than $\Phi_L$, the readout non-linearity error is stable with flux. The energy dependence of the non-linearity at low flux is investigated in Subsection 2.1.5. The readout losses then decrease for all energy points as the flux is increased above $\Phi_L$, until they are reduced to zero for fluxes larger than $\Phi_H$.

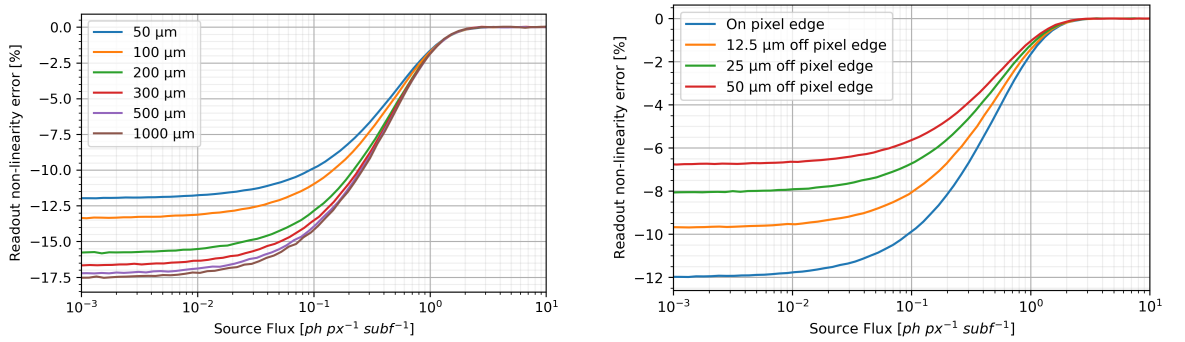
At low flux, the digital integration scheme (with LSB=1 ph) is functionally equivalent to a regular photon-counting scheme, as long as it is statistically improbable to record two or more photons in one pixel during a single subframe. A satisfactory flux criterion for the "low-flux approximation" is $\Phi \cdot \Delta t \cdot p^2 \ll 1\,\text{ph}$ with $\Phi$ the flux in ph/s/mm$^2$, $\Delta$t as the subframe duration, and p as the pixel pitch. From Figure 2.4, an empirical low-flux limit $\Phi_L$ can be defined. For fluxes below $\Phi_L = 0.01$ ph/subframe/pixel , the low-flux approximation is satisfied, the readout is purely a single photon-counting readout with a threshold set at the half-photon level, and the non-linearity error is constant with flux. For 100 µm pixels and 1 µs subframes, this translates to fluxes smaller than $\Phi_L = 1\,\text{Mph/s/mm}^2$.

Under these low-flux conditions, any amount of spatial charge sharing produces losses since a discrimination threshold is used [56,97]. For example, a photon absorbed in the very corner of a pixel has its electron cloud equally split in four pixels. Each of the four pixels sees 25% of the charge of the photon, and all four pixels discard the integrated charge as it is below threshold. Photons incident close to the corner of a pixel are therefore discarded, and the more spread-out the charge cloud is arriving at the collecting electrode, the larger the charge-sharing losses become. This means that more losses are expected when the electron cloud travels longer, for instance at low energies when photons are absorbed superficially.

Similarly, a high-flux limit $\Phi_H$ can be empirically defined from this plot. For fluxes above $\Phi_H = 3$ ph/subframe/pixel ($\Phi_H = 300\,\text{Mph/s/mm}^2$ for 100 µm pixels and 1 µs subframes), the readout records zero losses for all energy points and behaves like a conventional charge integrating readout. The transition between photon-counting and charge-integrating regimes lies between $\Phi_L$ and $\Phi_H$. As the flux increases over this range, the likelihood of having multiple shared events in the same pixel and in the

same subframe increases. This then reduces the readout losses because an additional shared event may carry enough charge to go above threshold in a pixel that originally only received a photon near its corner. When the flux is increased above $\Phi_H$, the system counts the correct number of photons on average. There are enough charge-sharing events to balance out the quantisation error on average and the readout reaches linearity.

Moving away from uniform illumination, a line illumination with a Gaussian profile was simulated on a 100 µm pixel matrix, replicating the more realistic scenario of a diffraction ring pattern. The line is parallel to the matrix y axis and along the x axis has a matrix-centred Gaussian profile with a standard deviation ranging from 50 µm to 1000 µm. Figure 2.5a shows the readout non-linearity error when the Gaussian line is centred on the pixel edges. The error is shown for the five central pixels (see Figure 2.2b), which receive the largest flux. The same flux regimes seen previously in Figure 2.4 are apparent with Gaussian illumination. Losses at low flux decrease as the illumination profile transitions from quasi-uniformity for 1000 µm standard deviation to a narrower distribution. As the illumination is focused on to fewer pixels, shared events contributing to charge-sharing losses become less likely. This explains why aligning the Gaussian line on the pixel edges has more losses than other positions in x, as shown in Figure 2.5b.




**(a)** RNL error with Gaussian line standard deviations

**(b)** RNL error with 50 µm Gaussian line positions

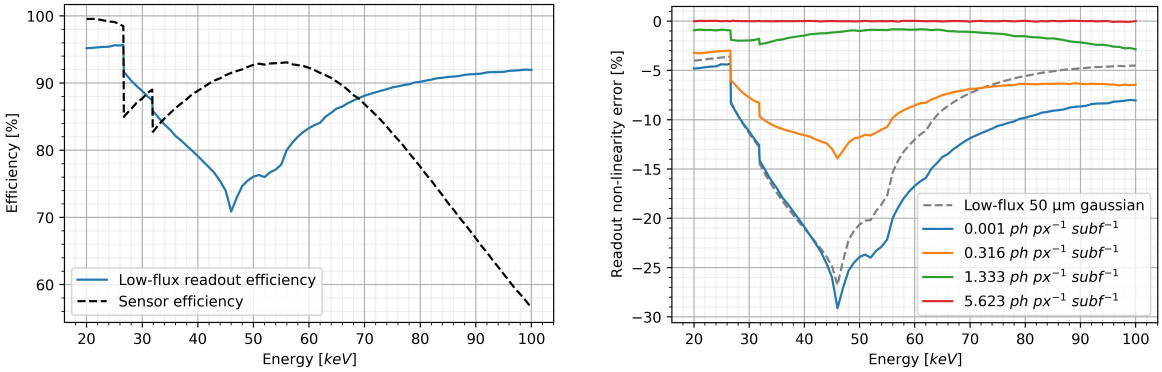
**Figure 2.5.** Simulated readout non-linearity (RNL) error for a digitally integrating detector with 1-mm CdTe sensor and 100 µm pixel pitch, as a function of the source flux, under 60 keV Gaussian-profile line illumination. Graph (a) shows the influence of the profile width when aligned with the pixel edges. Graph (b) shows the RNL error when a 50 µm Gaussian line is translated in x, parallel to the pixel edges.

While digital integration exhibits no non-linearity error under high-flux illumination in all investigated cases, Figure 2.4 also shows that the low-flux losses are highly

dependent on the energy of irradiation. Evidently, this is tied to fluorescence: low-flux losses are doubled from 26.6 keV to 26.7 keV, just below and above the Cadmium K-edge respectively. This is worthy of a dedicated investigation.

### 2.1.5 Readout performance with X-ray energy

The energy dependence of low-flux losses can be investigated in more detail through similar X-DECIMO simulations. To understand the physical mechanisms in action, it is essential to consider the total chain of losses in a detector. Figure 2.6a shows both the sensor and the readout losses, represented as efficiencies versus source energy. The readout efficiency is the ratio between the detector output and collected charge, which is converted into a percent or non-linearity error in Figure 2.4 and Figure 2.6b.




**(a)** Sensor and readout efficiency at low flux

**(b)** RNL error for increasing flux

**Figure 2.6.** Simulated losses in a digitally integrating detector with 1-mm CdTe sensor and 100 µm pixel pitch, as a function of the source energy. Graph (a) shows the readout efficiency at low-flux overlapped with the sensor efficiency with respect to incident photon dose. Graph (b) shows the readout percent error tending to zero as the flux, expressed in *X-ph/subframe/pixel*, is increased. The dashed line is the error for a $10^{-5}$ X-ph/subframe/pixel Gaussian-profile line illumination with 50 µm standard deviation.

Fluorescence translates to readout losses for digital integration. This is due to the Stokes shift: fluorescence photons are emitted with a predetermined energy that is always lower than the incident photon energy [98]. Consequently, after a fluorescence event, some energy is deposited in the sensor as photoelectrons. The amount of energy deposited in the sensor is of the order of the keV at the K-edge. This fluorescence deposit increases with the X-ray source energy since fluorescence photons have fixed wavelengths and energy is conserved. These electrons drift within the sensor and are collected at the cathode, where they are discarded if below the half-photon threshold.

From the readout perspective, a behavioural shift occurs at the energy point corresponding to twice the fluorescence photon energy, as depicted in Figure 2.7. Below this point, the majority of the initial photon energy is located in the re-emitted fluorescence photon. In the low-flux approximation, as soon as there is fluorescence escape or fluorescence redistribution, the collected electrons from the fluorescence deposit amount to a charge below threshold and are discarded. This participates in lowering the readout efficiency when the energy is increased up to twice the photon energy, around 46 keV with the most likely fluorescence photon being 23.2 keV. Above this point, the fluorescence deposit is the larger part of the initial photon energy and the readout starts counting the fluorescence deposit as a full incident photon and discards the re-emitted fluorescence photon. Similarly, the impact of fluorescence redistribution on spatial resolution also diminishes as the source energy is increased above the critical point.




**Figure 2.7.** Illustration of the behavioural shift of the IDI scheme with regard to fluorescence escape. When the source energy is below twice the fluorescence energy (*e.g.* 45 keV, left figure), the sensor deposit is below threshold and discarded. When above (*e.g.* 50 keV, right figure), the sensor deposit is counted.

Charge sharing brings additional losses at low flux because of fluorescence. A fluorescence event splits the charge in two smaller energy packets, while the readout is tuned for the original incident photon energy. The mismatch between these two packets and the threshold brings additional chances to discard information in the case of a shared event, increasing readout losses. This is most likely when fluorescence evenly splits the energy, *i.e.* in the 40 to 55 keV range.

As shown in Figure 2.6b, a flux increase reverses the non-linearity error trend over the energy range simulated, reaching a negligible value when over a few photons per subframe per pixel.

Figure 2.6b also compares how the low-flux losses behave with energy for uniform versus non-uniform illumination. The non-uniform illumination considered here is a

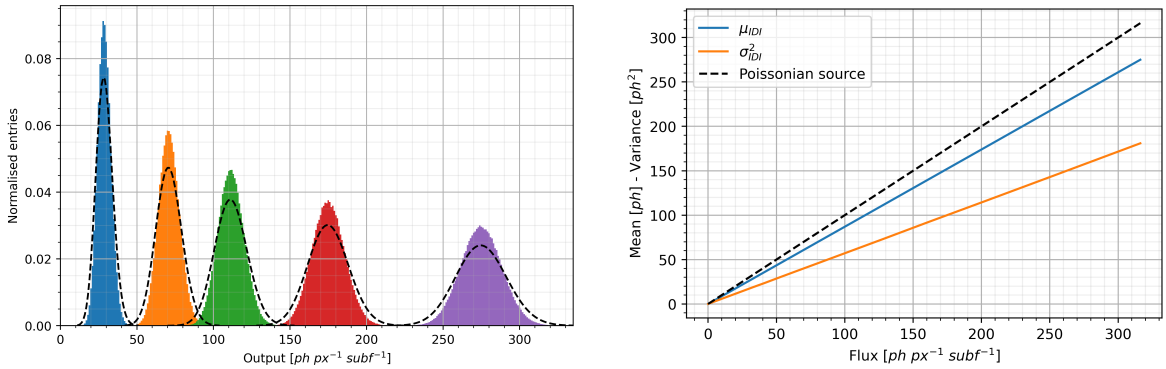
low-flux, matrix-centred Gaussian-profile line with 50 µm standard deviation, centred on the pixel edges. Overall, the same physical properties dictate the shape of the curve. Between the K-edge and twice the fluorescence energy, fluorescence is the dominant cause of readout losses and the uniform and non-uniform illumination curves differ negligibly. At lower and higher energies, as explained in Subsection 2.1.4, a smaller standard deviation means fewer shared events and thus fewer losses.

### 2.1.6 Statistics retrieved from a Poisson source with uniform illumination

The previous subsections have focused on the performance of a digitally integrating detector averaging over many subframes. The synchrotron X-ray source follows Poisson statistics, therefore, it is worth investigating not only the average subframe counts, but the standard deviation of subframe counts and the output distribution. The investigation of these aspects is necessary for the comprehension of the experimental characterisation, presented in Chapter 5.

X-DECIMO simulations were used to characterise the distribution of outputs recorded per subframe by a digitally integrating detector under uniform illumination. X-DECIMO generates a purely Poissonian source, but this does not imply that the digital output of the detector takes the shape of a Poisson distribution. Figure 2.8a shows the retrieved output distribution for several fluxes, fit with a Poisson probability mass function. These histograms were generated by simulating a 5×5 pixel matrix of 1-mm CdTe with 100 µm pixel pitch and looking at the distribution of counts per subframe in the central pixel. For all fluxes depicted, the retrieved histograms are narrower than their Poisson fit counterparts. Figure 2.8b compares the mean and standard deviation of the output distributions as a function of the 30 keV source flux. These two figures show how the retrieved output distribution are sub-Poissonian, as the variance is systematically below the mean.

Both mean and variance of the simulated output distributions are below the Poissonian source statistics, although scaling linearly with flux. In this example, at high fluxes is observed a 13% deviation in the output mean $\mu_{IDI}$ from the source mean $\mu_{source}$. This is consistant with the detector performance at 30 keV previously simulated in Subsection 2.1.3: $\eta(30\,\mathrm{keV}, high\text{-}flux) = \eta_{sensor} \times \eta_{collector} \times \eta_{readout} = 0.88 \times 0.99 \times 1 = 0.87$. The deviation of the output variance $\sigma^2_{IDI}$ from its mean $\mu_{IDI}$ is a measure of how close to an ideal Poisson distribution the output distribution is. To quantify this deviation can be used the Fano factor $F = \sigma^2/\mu$. A dataset is sub-Poissonian when $F < 1\,\mathrm{ph}$. Figure 2.8b shows that the output variance is about




**(a)** Per-subframe output distributions for several fluxes

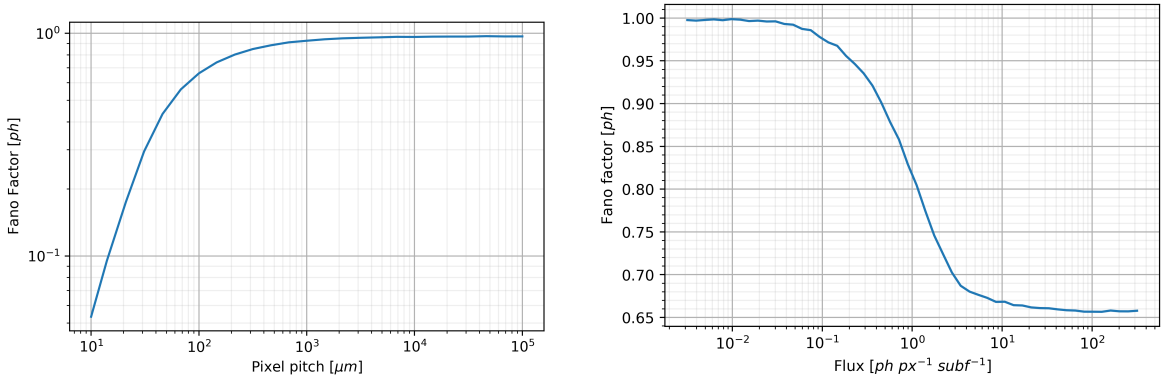
**(b)** Mean $\mu$ and variance $\sigma^2$ of output distributions vs. flux

**Figure 2.8.** Simulated output statistics for a digitally integrating detector with 1-mm CdTe sensor and 100 µm pixel pitch, as a function of the source flux, under 30 keV uniform illumination. Graph (a) shows that output distributions have a Gaussian shape narrower than Poisson distributions (dashed lines). Graph (b) compares the output statistics with that of the source.

34% below the output mean at high fluxes, meaning that these datasets have a Fano factor $F = 0.66$ ph.

The distribution becomes sub-Poissonian as soon as incoming signal spreads out over different pixels. An individual pixel sees a convolution of many Poisson distributions, resulting in a narrower distribution: the standard deviation of the per-pixel count distribution is lowered but its mean remains unchanged, which lowers its Fano factor in the process. In the X-DECIMO simulation, charge is shared between neighbouring pixels through electronic diffusion and fluorescence redistribution, which affects the digital readout. This information sharing is highest when fluorescence splits charge the most evenly, corresponding to an energy range of around 40 to 50 keV, where the Fano factor is $F \approx 0.60$ ph. This coincides with the peak of readout losses seen in Subsection 2.1.5, Figure 2.6. A bigger pixel pitch decreases the amount of signal shared between pixels. Figure 2.9a shows the simulated Fano factor at high flux as a function of the pixel pitch. The high-flux Fano factor is indeed found to tend towards an ideal Poissonian value of 1 as the pixel pitch is increased.

At lower fluxes, digitisation plays a significant role in shaping the output distribution. Figure 2.9b shows the Fano dependence with flux in log scale, for 30 keV uniform illumination. Much like the readout non-linearity error seen in Subsection 2.1.4, a transition from a low-flux to a high-flux regime is seen. For fluxes higher than 10 ph/subframe/pixel, in the purely charge-integrating regime, the Fano factor is then a constant of the pixelated sensor geometry and of the transverse mean travel of sig-




**(a)** High-flux Fano factor vs. pixel pitch

**(b)** Fano factor vs. flux (100 µm pixel pitch)

**Figure 2.9.** Simulated Fano factor of a digitally integrating detector with 1-mm CdTe sensor under 30 keV uniform illumination. Graph (a) demonstrates how the high-flux Fano factor gets closer to 1 as the pixel pitch is increased. Graph (b) highlights the Fano factor plateau at high fluxes.

nal. For the lowest fluxes in Figure 2.9b, signal discrimination through thresholding erases charge sharing: only 1 pixel records an event for a given input and the Fano factor is 1.

## 2.2 Readout limitations

In the previous section, readout performance for digital integration was investigated for an ideal system. A real readout will exhibit non-idealities, notably calibration imperfections, front-end electronic noise and sensor leakage. This section aims to evaluate the impact of these limitations on the readout functionality.

### 2.2.1 Role of calibration

All X-DECIMO simulations of Section 2.1 were performed with the assumption of a perfect calibration. This implies that the readout is configured to the exact amount of charge equivalent to a single monochromatic photon in CdTe, with a threshold perfectly set at the half-photon energy to have mid-tread quantisation. In a non-ideal system, a calibration routine must be carried out to configure the electronics to the single photon charge level at a given energy with an uncertainty.

The system presented in this work has two stages, as depicted in Figure 1.12: a coarse stage counting in packets of 8 photons for dynamic range, and a fine stage counting in packets of 1 photon for single-photon resolution. Consequently, this system requires the calibration of four parameters: the charge packet (CP, or LSB) size and

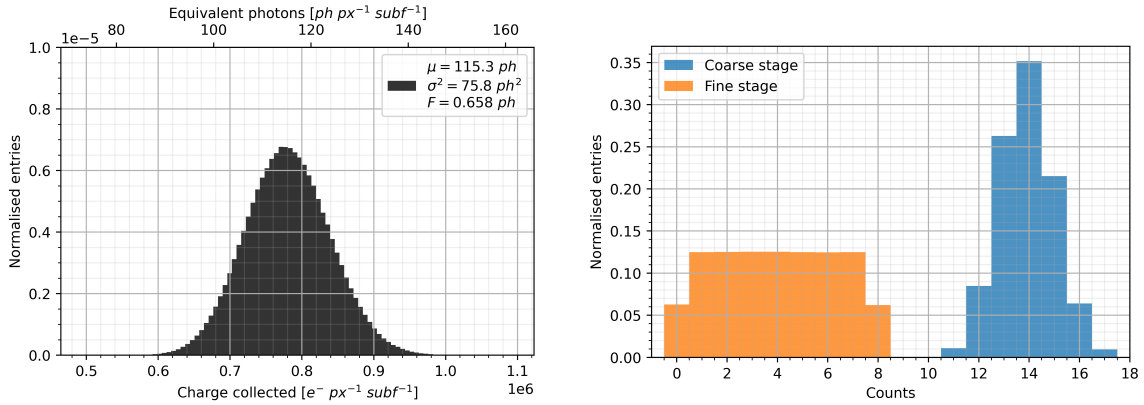
the threshold (THR) for each stage.

Ideally, these values should be:

- *CP0* (*LSB0*) = 8 ph and *THR0* = 8 ph in the coarse stage,
- *CP1* (*LSB1*) = 1 ph and *THR1* = 0.5 ph in the fine stage.

It is worth taking a look at the impact of eventual imperfections in the setting of these four parameters on the readout behaviour. With X-DECIMO is simulated a 30 keV uniform Poisson source illuminating a detector with a 100 µm pixel pitch over a 5×5 pixel matrix. At the collector level, the distribution of electrons collected per pixel per subframe is recorded, and rescaled to equivalent photons per pixel per subframe. This distribution has a Fano factor $F \approx 0.66$ ph, see Subsection 2.1.6. An example of such a distribution centred around $\mu \approx 115$ ph is shown by Figure 2.10a.

This distribution is then processed by a two-stage charge-pumping readout with a range of value for the four parameters *CP0*, *THR0* and *CP1*, *THR1*. When processed with the ideal calibration values for each parameter, the coarse stage has a shape matching the distribution of electrons collected, and the fine stage ranges from 0 to 8, see Figure 2.10b. It should be noted that, with *THR1* = 1 ph, the fine stage would range from 0 to 7 with a flat distribution. The total distribution reconstructed with $N = 8N_{coarse} + N_{fine}$ maintains its original shape, with its mean and Fano factor.




**(a)** Distribution of electrons collected per pixel per subframe

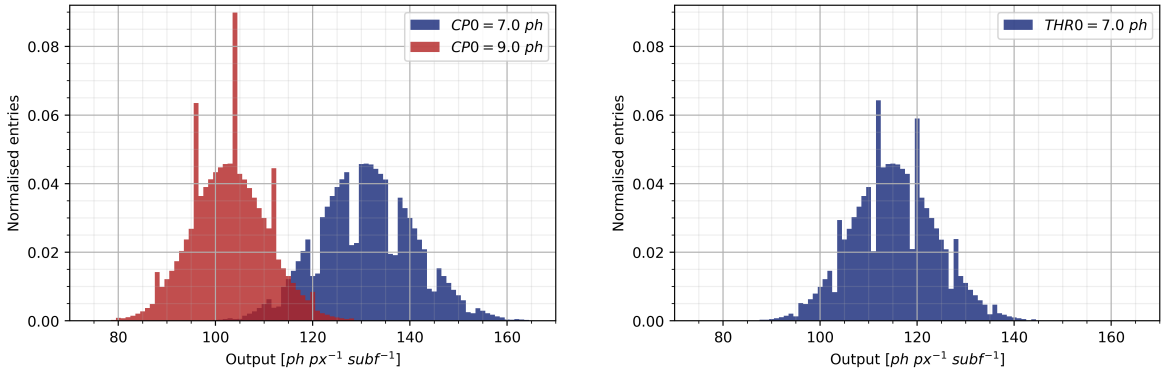
**(b)** Output distribution of the coarse and fine stages (perfect calibration)

**Figure 2.10.** Simulated distributions of counts per subframe under 30 keV illumination, at the collector level, and after using ideal CP and THR values for each stage.

Deviations from these ideal values can result in distortions of the retrieved distribution, as shown in Figure 2.11. The most notable changes arise from a miscalibration of the coarse stage charge packet size *CP0*, driving the dynamic range. As depicted by Figure 2.11a, when *CP0* is smaller than its ideal value, the readout overcounts

the number of photons and the output distribution is elongated to larger Fano factor values. Trough defects with a periodicity of 8 appear from the mismatch of the parameters since the fine stage is less likely to count 0 photon for any subframe. In the opposing case, the readout undercounts when *CP0* is larger than its ideal value and the Fano factor then decreases. Spike defects in turn appear in the distribution, due to the increased likelihood of the fine stage counting 0. Similar defects appear with miscalibration of the fine stage charge packet size *CP1*, although these do not change significantly the total distribution statistics, which are mostly determined by the coarse stage.

With an ideally calibrated fine stage, a miscalibration of the coarse stage threshold *THR0* is impactful only when set lower than its ideal value, as shown by Figure 2.11b. Indeed, when $THR0 \leq CP0$ there is a possibility to transfer negative charge to the fine stage, which is not handled. If *THR0* is too large, the fine stage compensates it and the total histogram is preserved. A miscalibration of the fine stage threshold *THR1* alone results in a translation of the distribution by the difference between *THR1* and 0.5 ph, and defects appear with values of $THR1 \geq CP1 = 1$ ph.




**(a)** Miscalibration of *CP0*

**(b)** *THR0* smaller than its ideal value

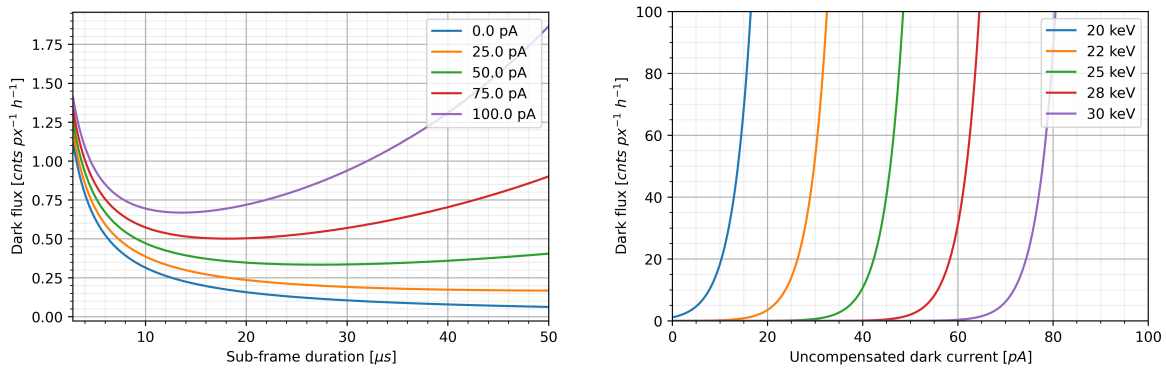
**Figure 2.11.** Output distributions of counts per subframe with simulated calibration imperfections.

To summarise, while closely matching the charge packet size values is needed to keep the original distribution shape, there exists a tolerance on the setting of the thresholds. In the coarse stage, the threshold should be above 8 ph, and in the fine stage it can be anywhere below the LSB, here 1 ph. The fine stage threshold can then be adjusted depending on the electronic noise in the prototype to avoid dark counts.

### 2.2.2 Effect of noise and dark current

A real hybrid pixel detector exhibits electronic noise and sensor leakage current, which become significant at low photon energies. Single-photon sensitivity at a given energy is only meaningfully achieved if it is statistically unlikely for the dark signal to be over threshold. The dark flux of a pixel is defined as its recorded output flux under zero illumination for a given threshold. To form a signal-to-noise ratio, this dark flux should be compared with a reference flux, typically the minimum expected flux per pixel.

On current XIDer prototypes, an equivalent noise charge of 350–375 $e^-$ rms has been measured. A first measure of this noise is mentioned in Section 3.4. An equivalent noise charge of 375 $e^-$ rms translates to a 1.66 keV equivalent noise energy in CdTe. This noise, assumed to be perfectly Gaussian, is added at the end of each subframe in the simulation. The likelihood of recording a noise hit at a 20 keV photon energy, *i.e.* the noise passes over the 10 keV threshold, is approximately 1 in 100 million. As shown in Figure 2.12a, this translates to a dark flux of approximately 1 cnt/hour/pixel for 1-10 µs subframes. Shorter subframes mean more subframes per unit time, and in turn a higher dark flux. For longer subframes, the front-end noise becomes negligible compared to the shot noise associated to the integration of (even fully-compensated) dark current, scaling as $\sqrt{\Delta t_{subframe} I_{dark}}$. These two phenomena explain the V-shape of Figure 2.12a.




**(a)** Dark flux vs. subframe duration at 20 keV

**(b)** Dark flux vs. uncompensated dark current

**Figure 2.12.** Digital integration dark flux in an ideal CdTe pixel, considering an equivalent noise charge of 375 $e^-$ rms. Graph (a) shows the behaviour at 20 keV with subframe duration and increasing, fully-compensated dark current. Graph (b) shows the dark counts increase for a 2.8 µs subframe if some dark current is left uncompensated.

Considering the use cases of XIDer envisaged, these dark flux values remain acceptable. As shown in Figure 2.12b, the main issue is uncompensated dark current

which, past a certain value, exponentially increases the dark counts. While readout noise is not worrisome, leakage compensation is a mandatory aspect to consider, especially in CdTe detectors. It is important for data quality to have a dynamic dark current compensation scheme in addition to the conventional static compensation.

## 2.3 Conclusion

Incremental digital integration is a robust readout scheme, which handles both single-photon resolution and a very high dynamic range, provided that the calibration is precisely performed. Calibration techniques on prototypes are explored in Chapter 4.

X-DECIMO simulations show that readout losses are present at low fluxes, *i.e.* below 1 to 10 ph/subframe/pixel. These readout losses are linked to partial charge collection and are inherent to any photon-counting scheme because of signal discrimination and quantisation. Partial charge collection is linked to physical phenomena such as charge diffusion and fluorescence, spreading charge transversally with a mean travel comparable to the pixel pitch. The more signal is shared between pixels, the more readout losses there are. As a consequence, readout losses are largest between 40 and 50 keV, where charge is redistributed the most due to fluorescence. This also means that low-flux readout losses are modulated by the sensor thickness and the pixel pitch: a thicker sensor translates to more charge diffused to neighbouring pixels, and a larger pixel pitch reduces the likelihood of signal shared between pixels.

The main limitation foreseen from this simulation study is uncompensated dark current. A dynamic leakage compensation scheme appears essential to mitigate dark counts in a fast high-dynamic range CdTe detector. Complex charge carrier dynamics at the origin of polarisation and aftersignal phenomena are difficult and computationally intensive to simulate and could not be a part of this study. The aftersignal phenomenon in XIDer prototypes is investigated in depth experimentally in Chapter 5.

# Chapter 3

# System Description

This chapter presents the hardware and software solutions that were implemented for the prototype detector system under study. This system is intended to be a flexible common platform for the characterisation of several ASIC/sensor hybrid XIDer prototypes with different high-Z sensor materials: CdTe, CdZnTe, and GaAs. Following the description of the ASIC functionalities and programming settings, the sensor prototypes and hybridisation procedure, as well as the data acquisition system, are discussed.

## 3.1 ASIC prototype

The XIDer readout ASIC prototype, designed in multi-project wafer TSMC 65 nm technology by Heidelberg University in collaboration with the ESRF, aims to validate the functionality of the incremental digital integration readout scheme and find its limitations. The research and engineering phase of a readout ASIC for a detector system like XIDer is an iterative process. This manuscript focuses on the fourth iteration ASIC prototype, which has a 16-channel parallel readout and includes elaborate features for characterisation.

### 3.1.1 Front-end

A core element of the ASIC prototype is the two-stage pixel front-end present in each of its 16 channels. Figure 3.1 shows a schematic of this front-end.

Each of the two stages behaves in the same way. They are both comprised of a charge-sensitive amplifier (CSA), a comparator threshold, a charge pump, and a reset switch. The two stages are separated by a transfer switch and a transfer capacitor, annotated $S_2$ and $C_2$ respectively on Figure 3.1. Input switch $S_3$ connects the sensor

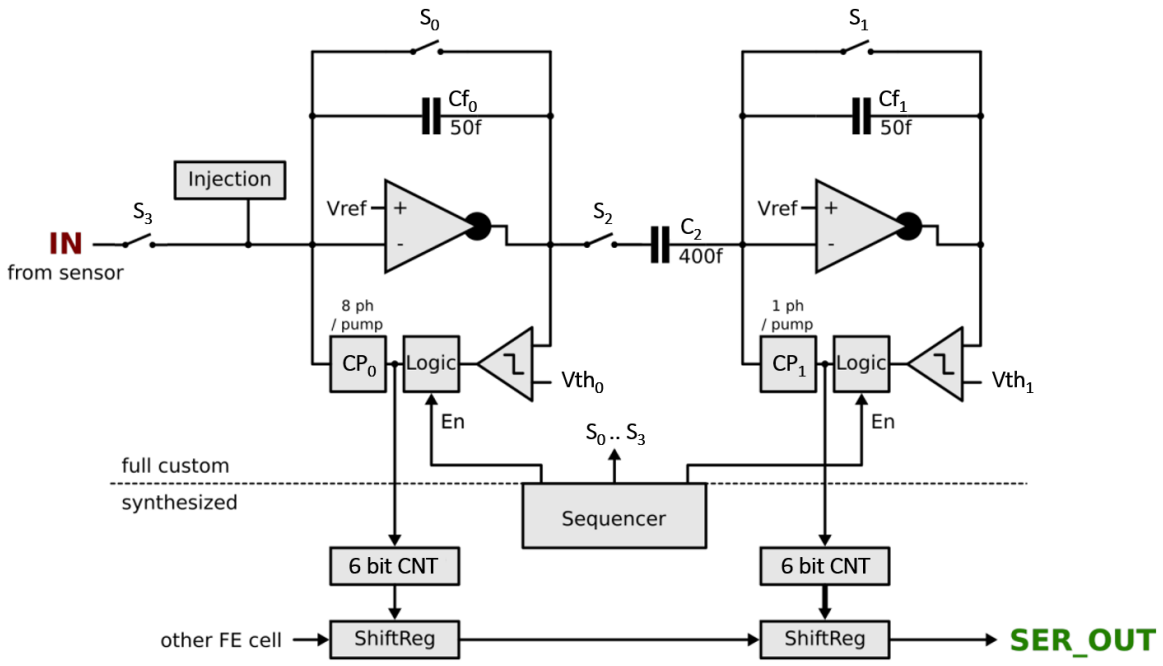



**Figure 3.1.** Schematic of ASIC T4 two-stage pixel front-end, implementing digital integration. In each stage, the input signal is integrated by a CSA, to then be compared to a threshold, which activates a charge pump and increments a counter. From [99] (modified).

to the input node of the first stage front-end. This working principle is akin to those of other detector systems, such as the MM-PAD [100] and the CIX [101]. An important difference with these detector systems lies in the data management of the ASIC T4, and its smart on-chip pre-processing capabilities allowing many different operation modes [102], detailed in Subsection 3.1.5.

When charge from the sensor arrives to the first stage (on the left-hand side of the schematic), it is integrated by the CSA, thus charging the 50 fF feedback capacitor $Cf_0$. The output voltage of the CSA is dynamically compared with a voltage threshold $Vth_0$. When the threshold is crossed, the logic increments a 6-bit counter and activates the charge pump circuit $CP_0$, removing a fixed amount of charge from the feedback capacitor $Cf_0$. If the pumping circuit is tuned so that each trigger removes an amount of charge equivalent to that generated by a single monochromatic photon, the counter in turn provides the digital number of monochromatic photons incident during that integration window.

To improve the dynamic range of the system, the first stage is intended to count in packets of multiple photons, 8 in this implementation. The charge pump $CP_0$ is, therefore, tuned to remove a charge packet for each activation equivalent to the charge generated by 8 monochromatic photons incident on the sensor. The threshold must be set accordingly, matching the voltage output of the amplifier after the integration

of 8 photons. The maximal dynamic range is largely limited by the driving frequency of the charge pump in the first stage. Circuit simulations with Cadence show that the charge pump can theoretically operate at driving frequencies reaching $f_{CP} = 200\,\mathrm{MHz}$ [99]. Pumping at this frequency with 8 photons per trigger translates to a maximum achievable flux of $\Phi_{max} = 1.6\,\mathrm{Gph/s/px}$, fulfilling the requirements for the XIDer detector system.

The residual charge from the first coarse stage, theoretically below 8 photons, is transferred to the second stage, depicted on the right-hand side of the schematic. The second stage digitises the transferred charge by removing packets equivalent to 1 photon and incrementing a second counter. Tuning the fine stage charge pump $CP_1$ to remove a charge packet of 1 photon is required to provide single photon resolution. The first stage counter value $N_{1st}$ and the second stage counter value $N_{2nd}$ are stored in shift registers, to be read out. The aggregate digital number representing the total number of photons counted is then given by $N = 8N_{1st} + N_{2nd}$.

As shown in the schematic, the designs of the two stages are identical, with both stages having a 50 fF feedback capacitor and the same charge pump circuit. The factor of 8 is provided by the capacitance ratio $C_2/Cf_1$, which amplifies the voltage output of the first stage by 8. In turn, the charge pump packet sizes should, in theory, be the same for each stage.

Before the stages integrate the input signal, they are reset by the closing of the switches $S_0$ and $S_1$ respectively, discharging their feedback capacitors and drawing the amplifier output to the virtual ground. The voltage output of the amplifiers then returns to their baselines. Switches $S_0$ and $S_1$, as well as the transfer switch $S_2$, are dynamically controlled by a programmable on-chip sequencer. The stages are reset with the periodicity of the subframe duration. To measure a longer exposition, several subframes can be recorded consecutively and their digital output summed. This subframe accumulation feature is already embedded in the T4 chip iteration, but, for the purpose of characterisation presented here, is performed in off-chip post-processing.

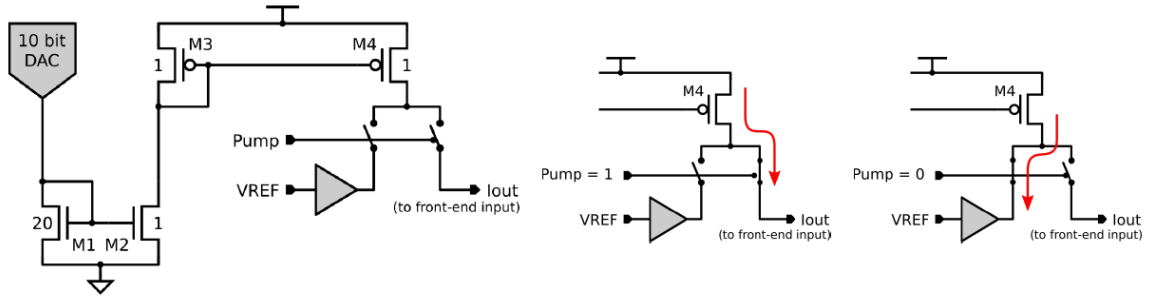
### 3.1.2 Front-end trimming

The functionality of each front-end relies on the proper setting of the comparator thresholds and the charge pump packet sizes. They must be finely tuned to make the coarse stage handle packets of exactly 8 photons, and the fine stage packets of 1 photon, at the specific monochromatic photon energy chosen for a given experiment.

The voltage level of the coarse stage comparator threshold, $Vth_0$, can be tuned using an on-chip 10-bit digital-to-analogue converter (DAC), in which 1 analogue-to-

digital unit (ADU) corresponds to a shift of 1 mV in $Vth_0$ by design. This DAC is named DAC:*COMP0*. Likewise, in the fine stage the threshold level can be tuned with the 10-bit DAC:*COMP1*.

The charge pump in this chip iteration is implemented as a four-transistor switched current source that delivers a current $I_{out}$ for a defined time period $t_{pump}$, thus generating a charge packet $Q = I_{out} \times t_{pump}$. The mechanism of the charge pump circuit is shown on Figure 3.2. The size of the charge packet is controlled by tuning the current $I_{out}$ using a 10-bit current DAC. The charge pump packet sizes of the coarse and fine stages can then be tuned with DAC:*CP0* and DAC:*CP1*.




(a) Circuit Schematics (b) PUMP State (c) DUMP State

**Figure 3.2.** Charge pump circuit, implemented as a four-transistor current source. A configurable current $I_{out}$, dynamically controlled by a *Pump* signal, flows to the front-end for a period of time $t_{pump}$, generating a charge packet $Q = I_{out} \times t_{pump}$. From [99].

These four DACs, *COMP0*, *COMP1*, *CP0*, and *CP1*, are shared with each of the 16 channels, and are programmed via a custom integrated JTAG interface. Table 3.1 summarises the DACs needed to trim the front-end. These need to be tuned according to the desired photon energy. The calibration techniques employed are discussed in detail in Chapter 4. These DACs were intentionally over-dimensioned at a high resolution of 10 bits for this prototyping phase. In later larger-scale chip iterations, these DACs will have a lower resolution.

**Table 3.1.** Summary table of key DACs.

| **Parameter** | **Corresponding DAC** |
|---|---|
| Coarse stage threshold | DAC:*COMP0* |
| Coarse stage charge packet size | DAC:*CP0* |
| Fine stage threshold | DAC:*COMP1* |
| Fine stage charge packet size | DAC:*CP1* |
| Internal charge injection size | DAC:*INJ1* |

### 3.1.3 Charge injection circuit

For the purposes of testing and calibrating XIDer ASICs without any sensor connected, a charge injection circuit was implemented in the chip design. It is depicted in Figure 3.1 at the input of the front-end.

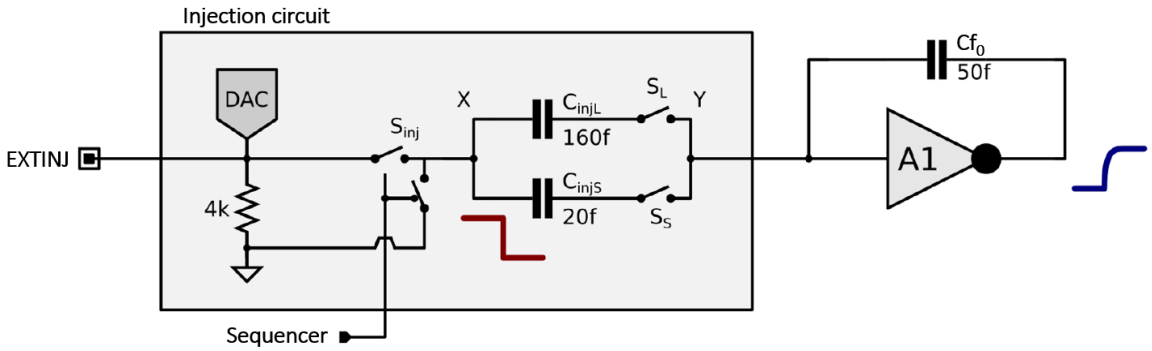



**Figure 3.3.** Schematic of the charge injection circuit connected to the front-end input. Injection can be provided internally from a current DAC:*INJ0*, or externally from the *EXTINJ* pad. $S_{inj}$ is comprised of two dynamic switches, connecting node $X$ to either the applied injection voltage or to ground. From [99] (modified).

Figure 3.3 shows the schematic of this charge injection circuit. Capacitors $C_{injS} = 20\,\text{fF}$ and/or $C_{injL} = 160\,\text{fF}$ are first chosen with the static switches $S_S$ and $S_L$, depending on whether a small or large injection is desired. A double-switch $S_{inj}$ is dynamically controlled by the sequencer to connect node $X$ to either the applied injection voltage or the ground. The injection voltage is either provided internally by a 10-bit current DAC *INJ0*, dumping a current in a $4\,\text{k}\Omega$ resistor, or externally from the *EXTINJ* pad. While the front-end is in reset, the injection voltage is applied to node $X$ which in turn charges the injection capacitor(s). When $S_{inj}$ switches from the applied injected voltage to the ground, the capacitor is discharged and charge moves from node $X$ to node $Y$ at the input of the first stage, to be integrated by the CSA.

### 3.1.4 Sequencer

A flexible on-chip sequencer provides the dynamic control of the system, generating programmable binary tracks for the operation of the front-end. In this ASIC T4 prototype, the sequencer can either follow the internal clock of frequency $f_{clk} = 311\,\text{MHz}$, or an externally-driven clock. It is essential to note that the subframe duration is defined as a multiple of the clock time period, and that it is thus necessary to use the synchrotron clock as an external clock to be able to synchronise with the X-ray timing distribution of the synchrotron. Relevant elements that can be dynamically controlled by the sequencer are given in Table 3.2.

**Table 3.2.** Dynamical controls by the on-chip sequencer, referring to items depicted in Figure 3.1

| Sequence | Item | Function |
|---|---|---|
| Res0 | $S_0$ | Reset of coarse stage |
| Res1 | $S_1$ | Reset of fine stage |
| Sw0to1 | $S_2$ | Transfer between stages |
| EnCP0 | $CP_0$ | Enable charge pump of coarse stage |
| EnCP1 | $CP_1$ | Enable charge pump of fine stage |
| InjB1 | $S_{inj}$ | Connect injection circuit to front-end or to ground |
| EnIN | $S_3$ | Switch connecting the sensor to the front-end |

### Two-stage pipeline

The coarse and fine stages work in a pipelined mode. During a transfer period controlled by the Res0, Res1 and Sw0to1 sequences, the residual charge from the coarse stage is transferred to the fine stage. This residual is digitised by the fine stage while the coarse stage is already back in operation for the following subframe. The gaps in the ESRF-EBS time structure, shown in Figure 1.3, are then exploited to achieve an effectively dead-time free operation of the front-end.

The typical sequencer tracks controlling the two-stage pipeline using 2 µs subframes are presented in Figure 3.4. The track for the injection is also defined here, providing charge injection shortly after the first stage is reset. Figure 3.5 shows the output voltage of the amplifier at the coarse stage and the fine stage level with these sequencer tracks, starting at $t = 0$ with the reset of the coarse stage, as shown in Figure 3.4.

Initially, the injection circuit is loaded by the rising edge of track InjB1, when switch $S_{inj}$ connects the injection circuit to the applied injection voltage, which has no influence on the front-end input as it is in reset. At the InjB1 falling edge, placed after the reset Res0, $S_{inj}$ switches to ground and the charge injection is provided at once to the first stage. This is observed at $t = 0.39\,\mu s$ on Figure 3.5. The charge is integrated in approximately 20 ns, with an overshoot stabilising over the course of a further 10 ns. The voltage has risen considerably above threshold, and the charge pump $CP_0$ is activated three times in a row, at the charge pump frequency $f_{CP}$. To have a clear picture in this example, the charge pump is used at the conservative frequency of $f_{CP} = f_{clk}/10 = 31.1\,\text{MHz}$, allowing $CP_0$ and $CP_1$ to pump every 32 ns.

The sequences Res1, Sw0to1 and Res0 at the beginning of the following subframe

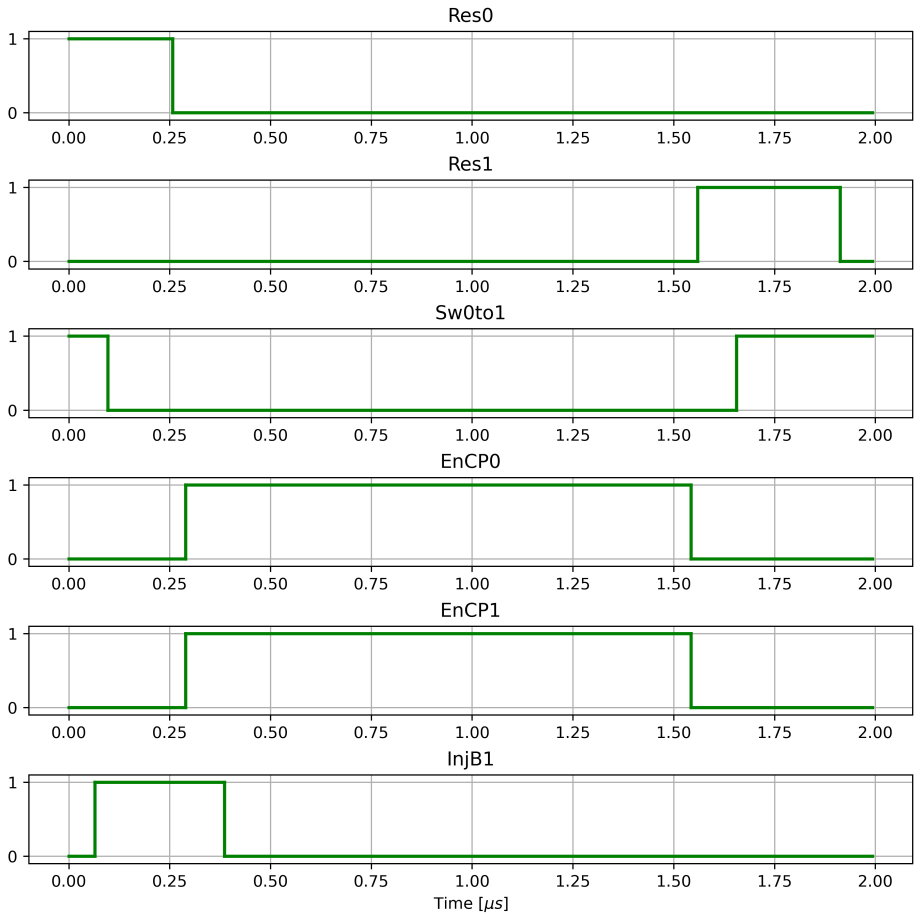



**Figure 3.4.** Sequencer tracks of two-stage pipeline, with charge injection provided shortly after the first stage is reset. Switches $S_0$, $S_1$, $S_2$ are closed when Res0, Res1, Sw0to1 are 1.

provide the transfer between the two stages.

- At $t = 1.56\,\mu s$, the transfer sequence is initiated with Res1, the reset of the fine stage. This discharges capacitor $Cf_1$ and brings the fine stage to ground, see Figure 3.6a.

- At $t = 1.66\,\mu s$, the transfer switch $S_2$ is closed, connecting transfer capacitor $C_2$ to the coarse stage output, see Figure 3.6b. A voltage is thus applied on $C_2$: virtual ground on its right, and on its left the coarse stage amplifier output voltage $V_{out_0} = Q_0/Cf_0$. This voltage charges $C_2$ with charge $Q_2 = C_2 V_{out_0} = \frac{C_2}{Cf_0} Q_0$, which is the residual charge from the coarse stage multiplied by the gain of 8 defined by the capacitor ratio.

- At $t = 1.91\,\mu s$, the fine stage reset switch $S_1$ is opened again, in time for $C_2$ to be finished charging.

- At $t = 2.00\,\mu s$, *i.e.* the start of the next subframe, Res0 is activated and the coarse stage moves to ground, discharging capacitor $Cf_0$ to be ready for the

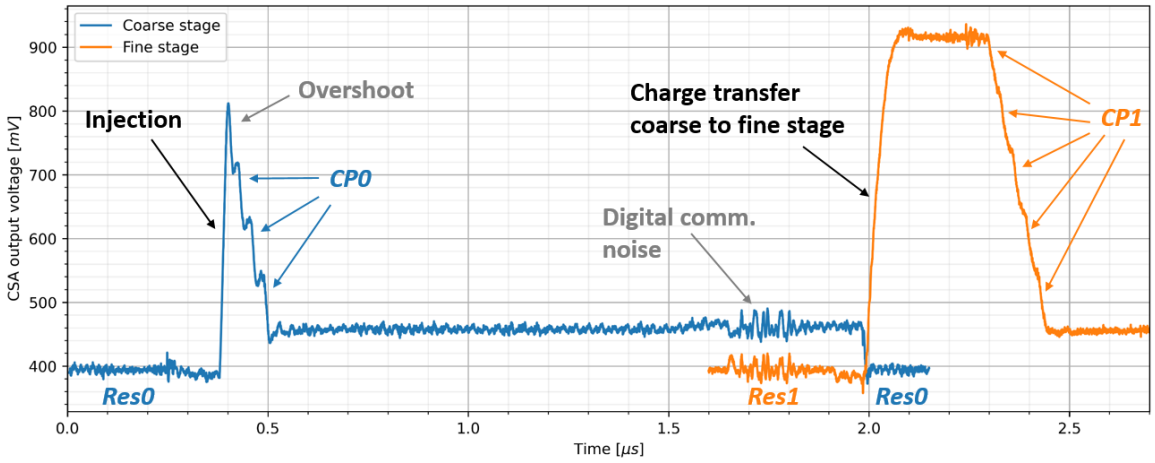



**Figure 3.5.** Example of oscilloscope trace from CSA output buffer in coarse and fine stages. The sequencer tracks are described by Figure 3.4; the charge injection size DAC:*INJ1* is set to 100 ADU. XIDer reads out $N = 8N_{coarse} + N_{fine} = 8 \times 3 + 5 = 29$.

next subframe. The left side of $C_2$ is now at virtual ground, and its right side, previously at virtual ground, is left floating. As a consequence, the charge on $C_2$ starts transferring to the fine stage feedback capacitor $Cf_1$, see Figure 3.6c. This charge transfer can be seen in the orange waveform of Figure 3.5 at $t = 2.00\,\mu s$. The transferred charge is pumped out by $CP_1$ shortly after, once EnCP1 is activated.

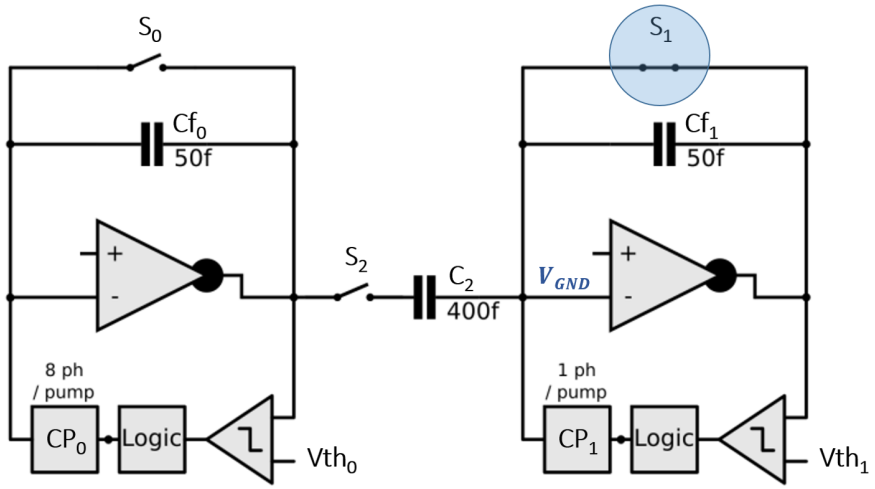
After the first subframe, both stages begin working in parallel: the fine stage handles subframe n while the coarse stage handles subframe n+1.

### Other useful sequencer configurations

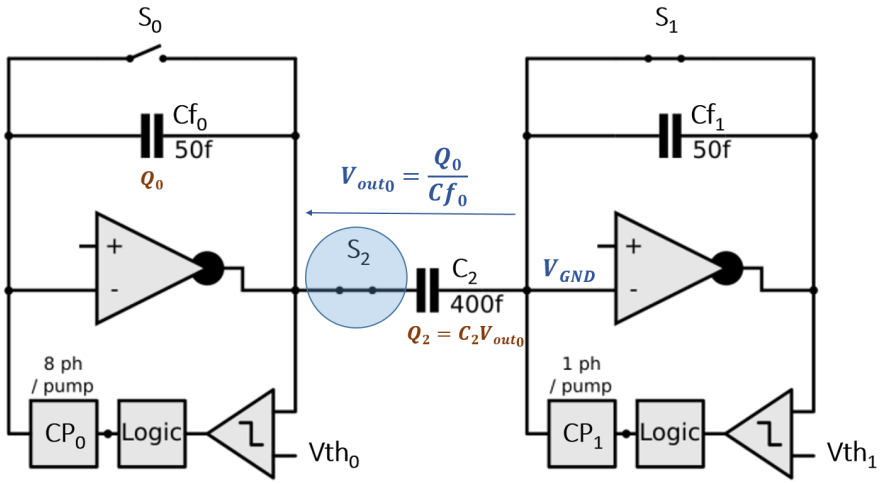
The sequencer can be tuned to operate XIDer as a simple charge integrating system. In CSA mode, only the coarse stage reset is defined, with the fine stage being in constant reset and the transfer and charge pumps disabled. This mode can be employed to observe the integration of incoming charge in the front-end through the amplifier output buffer on an external oscilloscope.

To measure the baseline and noise level in the coarse stage, with a DAC:*COMP0* sweep as shown in Section 3.4, the sequencer tracks to be used are given by Figure 3.7a. This is similar to the CSA mode, where the charge pump of the coarse stage is enabled for a short amount of time so that it may only trigger once per subframe, 10 clock cycles in the example given.

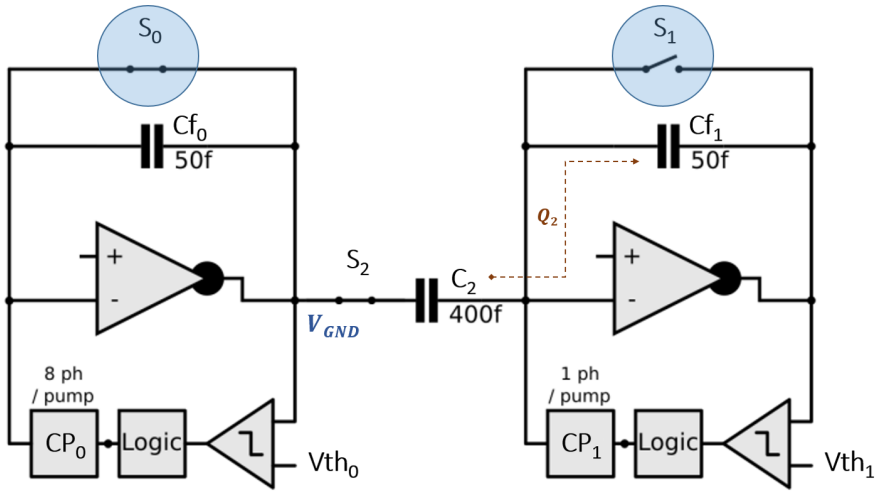
The baseline and noise can also be measured at the fine stage level with a DAC:*COMP1* sweep and using tracks described by Figure 3.7b. Here, the pipeline sequence is defined like in Figure 3.4 for the same reason, but it is the charge pump of the fine stage




**(a)** Switch $S_1$ is closed: capacitor $Cf_1$ is discharged and the fine stage input node is brought to ground.



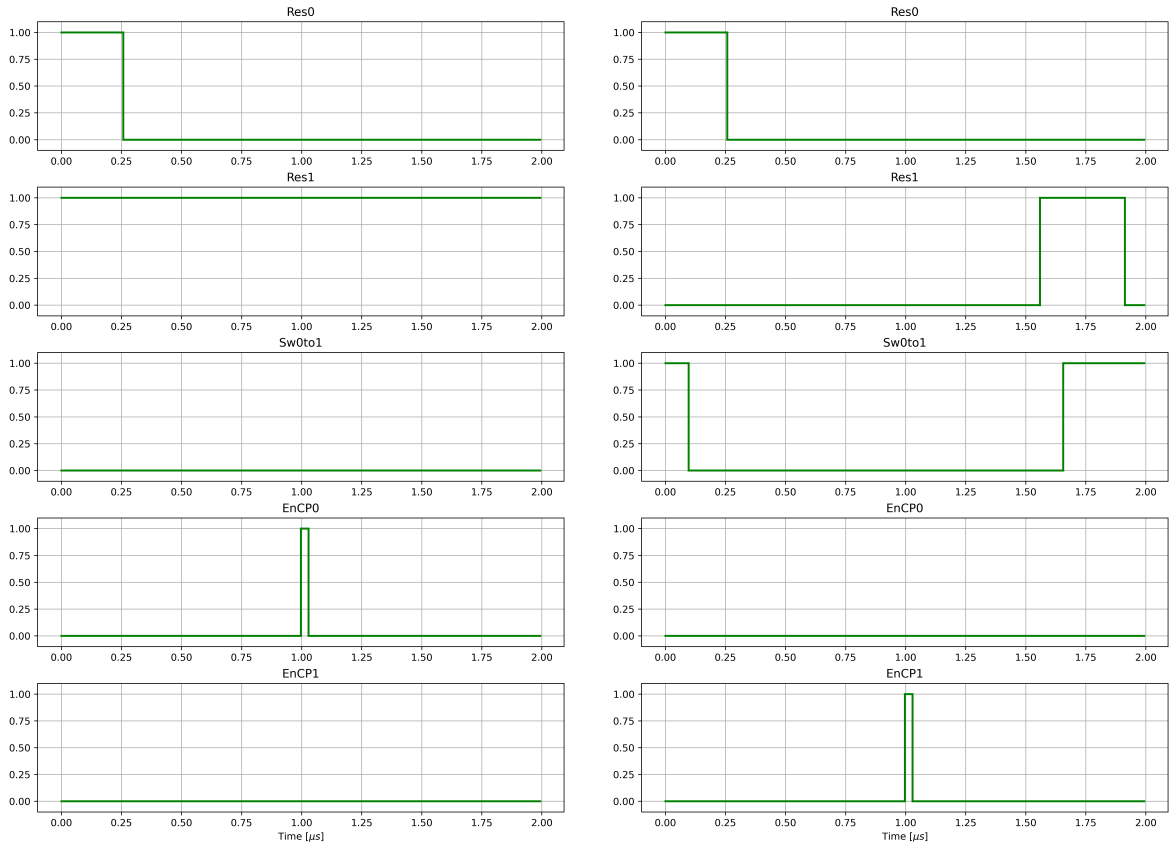

**(b)** Switch $S_2$ is closed: capacitor $C_2$ is charged with charge $Q_0$ stored on $Cf_0$ multiplied by transfer gain $C_2/Cf_0$.




**(c)** Switch $S_1$ is opened and $S_0$ closed: charge $Q_2$ gets transferred from capacitors $C_2$ to $Cf_1$.

**Figure 3.6.** Front-end schematics illustrating the transfer steps from coarse to fine stage.

that is enabled for only 10 clock cycles.




**(a)** Coarse stage baseline **(b)** Fine stage baseline

**Figure 3.7.** Useful sequencer configurations with a subframe duration of 2 µs.

### 3.1.5 Data handling: the telegram interface

The XIDer detector is designed to be a versatile tool able to function in several operation modes and suit the needs of the beamline users. What makes this versatility possible is the on-chip digital data management of the detector system, a schematic of which is presented in Figure 3.8.

As mentioned previously, the control block includes a sequencer for dynamic fast front-end control, and a JTAG interface for slow control. The focus of this subsection is the telegram interface inside this digital control block, allowing for a flexible and dynamic data flow control. In a pixel channel, the data storage and data readout is performed using a custom-designed in-channel RAM cell, with each cell able to store 192 16-bit words. At the beginning of each subframe, the ASIC receives instructions through a custom protocol detailing the procedure to follow for the storage and readout of the subframe digital data. Notably, these instructions specify what subframe

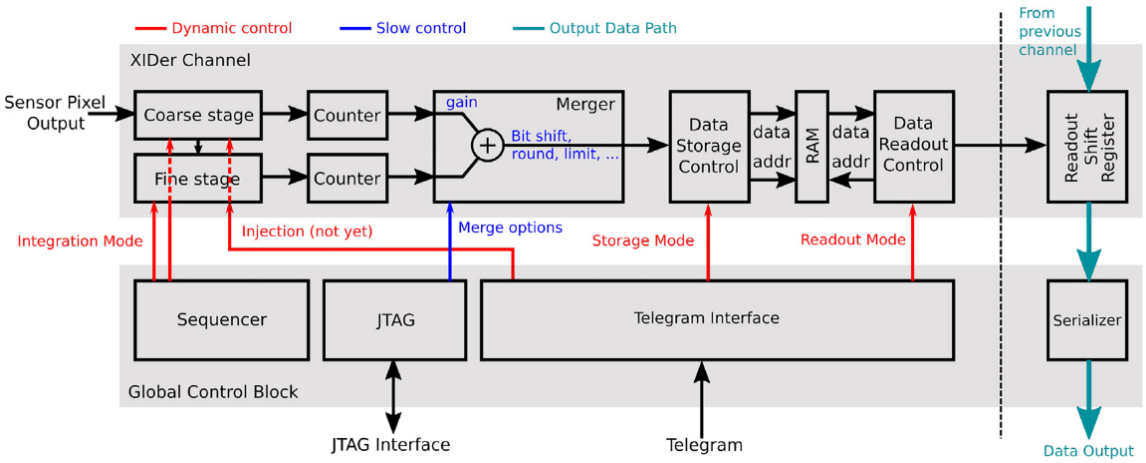



**Figure 3.8.** Schematic of the data control and handling paths of a pixel channel in ASIC T4. From [102].

information to write in storage and in which RAM address to store it. The writing operation functions include direct storing in the given RAM address, adding and subtracting the subframe value to the RAM address value, incrementing the RAM value, as well as discarding and clearing the RAM address.

Details of the telegram protocol and applications can be found in [102], but it is worth mentioning here some key modes enabled by the telegram interface. On the one hand, the incremental digital integration concept, as presented in Figure 1.10, is implemented with the addition operation enabling the accumulation of the many subframes that can make up one frame of exposure. On the other hand, when the focus is to push the fast time-resolved capabilities of the chip, for instance to follow processes with sub-microsecond time resolutions, the subframe accumulation is turned off and the storage operation is used instead. What is more, the increment operation enables the generation of on-chip histograms, where the RAM addresses become the histogram bins, and on-chip leakage correction can be performed with the subtraction operation. In combination of these modes, the telegram also handles the chip triggering, by discarding non-relevant subframes.

## 3.2 Sensor prototype

As discussed in Section 1.1, XIDer is intended to work at high photon energies of up to 100 keV, requiring the use of high-Z sensors. The main sensor material considered in this work is 1 mm-thick Cadmium Telluride (CdTe) from Acrorad Co., Ltd., with Ohmic Pt contacts on both the anode and cathode sides. CdTe sensors with Al Schottky anode and Ohmic Pt cathode contacts were also considered for

the XIDer project. The CdTe sensors with Schottky contacts were investigated extensively before being deemed impractical because of their greater instability due to polarisation [42,44,50,51]. The more promising Ohmic contacts were thus the favoured option. Chromium-compensated Gallium Arsenide (GaAs:Cr) from Tomsk State University was also briefly considered as a sensor material, but could not be the focus of the project because of its limited absorption efficiency at 100 keV, as well as its significant leakage current [103–105].

CdTe sensors are manufactured by Acrorad Co., Ltd. with a minimal area of $4 \times 4$ mm$^2$. A layout with this area was designed at the ESRF, shown in Figure 3.9. This design features two $4 \times 4$ pixel structures: one with 100 µm pitch, the other with 200 µm pitch. For each sensor, only one of these structures is to be bonded to an ASIC in order to produce a 100 µm-pitch or a 200 µm-pitch prototype 16-pixel assembly. Figure 3.9 is a picture of the sensor from the anode side, with the pixel pads used for sensor-ASIC hybridisation. To ensure a uniform electric field inside the bulk of the sensor, the full anode surface must be at the same voltage level. For this purpose, a guard ring is used to ground the non-pixelated surface of the sensor anode. Each pixel matrix is surrounded by two guard ring pads, and two additional larger pads can also be used to ground the anode, visible on the bottom of Figure 3.9.

Later in the XIDer project development, high-flux capable CdZnTe sensors with a similar layout were purchased from Due2Lab. The electrode processing was made by Due2Lab, but the CdZnTe material is itself manufactured at Redlen Technologies. While a very promising sensor material in the context of the XIDer detector requirements [52, 53, 106, 107], procuring high-flux CdZnTe sensors in the size and quality necessary has proven difficult.

## 3.3 Characterisation apparatus

### 3.3.1 Carrier and mezzanine printed circuit boards

A large number of XIDer ASIC/sensor assemblies are to be characterised using the same data acquisition system. Printed circuit boards (PCBs) were thus manufactured in order to easily test and switch between assemblies. These PCBs were custom-designed at the ESRF. Each ASIC is glued on its own carrier PCB and wire-bonded to its pads, as shown in Figure 3.10. This carrier PCB handles all data transfer and direct connections to the ASIC itself, including the two 1.2 V power lines for the digital part, and for the analogue part of the ASIC. These power lines are filtered by capacitors on the carrier PCB. It also provides the high-voltage connection to the top

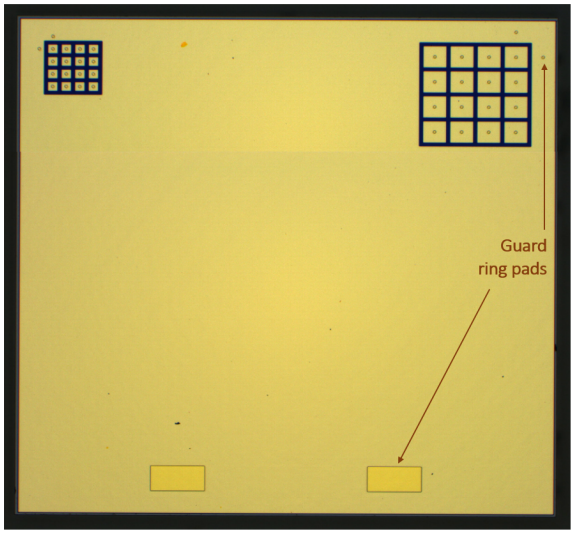



**Figure 3.9.** Picture of a prototype 1 mm-thick $4 \times 4$ mm$^2$ planar CdTe sensor, produced by Acrorad Co., Ltd., with a 100 µm-pitch 16-pixel matrix (top left), a 200 µm-pitch 16-pixel matrix (top right). Guard ring pads are present around each matrix and at the bottom of the sensor to ground the non-pixelated anode surface.

of the sensor — the cathode — from SMA connector *P0*, which must be connected to an external high-voltage power supply to bias the sensor.

To bridge between carrier PCB and data acquisition system (DAQ), another "mezzanine" PCB, shown in Figure 3.11, is used as a communication interface. The carrier PCB is mounted on the mezzanine PCB, and this second PCB handles the monitoring of the ASIC chip: voltages from the chip can be carried on connectors on this PCB for live monitoring and debugging purposes. On this current XIDer ASIC iteration, only one front-end, front-end number 15, can be monitored with an oscilloscope. In FE15, the voltage levels at the coarse and fine stage CSA outputs are carried through a buffer to SMA connectors P4 and P5 respectively. SMA connector P3 can provide digital signals, such as a sequencer track (useful to trigger the oscilloscope) or trigger signals from the charge pump of any channel. Charge injection from an external pulse generator can also be provided to the *EXTINJ* ASIC pad through SMA connectors on the mezzanine. This PCB handles the voltage translation from 3.3 V to 1.2 V, transferred to the carrier PCB through respectively the top and bottom board-to-board connector. It also handles the generation of the ASIC internal clock, as well as the biasing for the sensor ground plane, which is provided by an external 6 V supply through the power cables on the top-left corner. The voltage level of the grounding plane can be tuned with a trimmer on the PCB.

The role of each SMA connector on the carrier and mezzanine PCBs is outlined in Table 3.3.

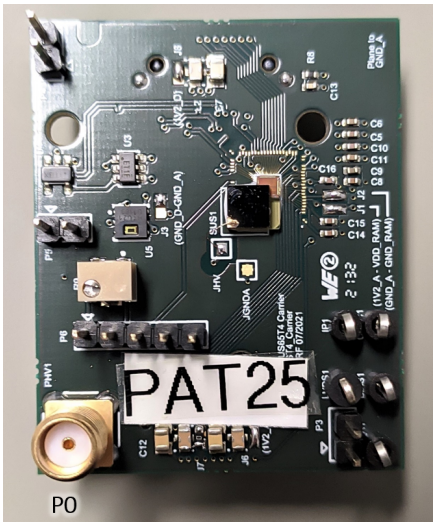



**Figure 3.10.** Carrier PCB, hosting and wire-bonded to the ASIC.

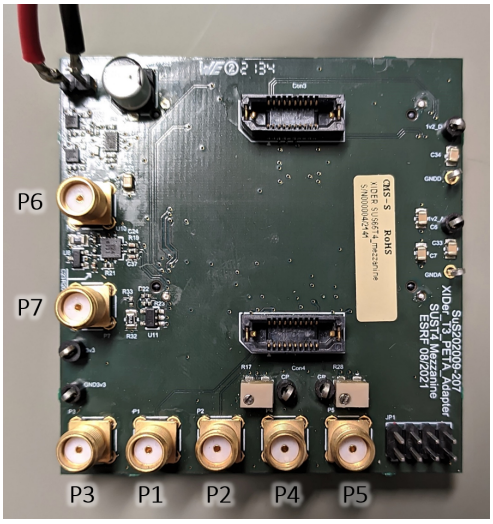



**Figure 3.11.** Mezzanine PCB, interface between carrier PCB and DAQ.

**Table 3.3.** SMA connectors on the PCBs.

| SMA connector | Function |
|---|---|
| P0 | High-voltage supply |
| P1 | External injection |
| P2 | External injection |
| P3 | Monitoring |
| P4 | Coarse stage CSA voltage output |
| P5 | Fine stage CSA voltage output |
| P6 | Clock synchronisation |
| P7 | Subframe trigger |

### 3.3.2 Complete setup

The mezzanine-carrier PCB stack is plugged into a generic readout FPGA-board called PETA, based on USB 3.0 communication and designed by Heidelberg University. The slow control of the system is provided by a JTAG chain accessed via a FT2232 chip, while the fast data transfer is handled by a FIFO-to-USB3 bridge via a FT601 chip. Both chips link to the FPGA, which communicates with the ASIC through the mezzanine-carrier PCB stack. The FPGA is programmed with a simple firmware to ask, receive, and transfer readout data packages.

As shown in Figure 3.12, the PETA board is directly connected via USB 3.0 to a dedicated computer. An interface was programmed in Python to control and read out the system. A Rigol DP832 programmable power supply provides the 3.3 V to

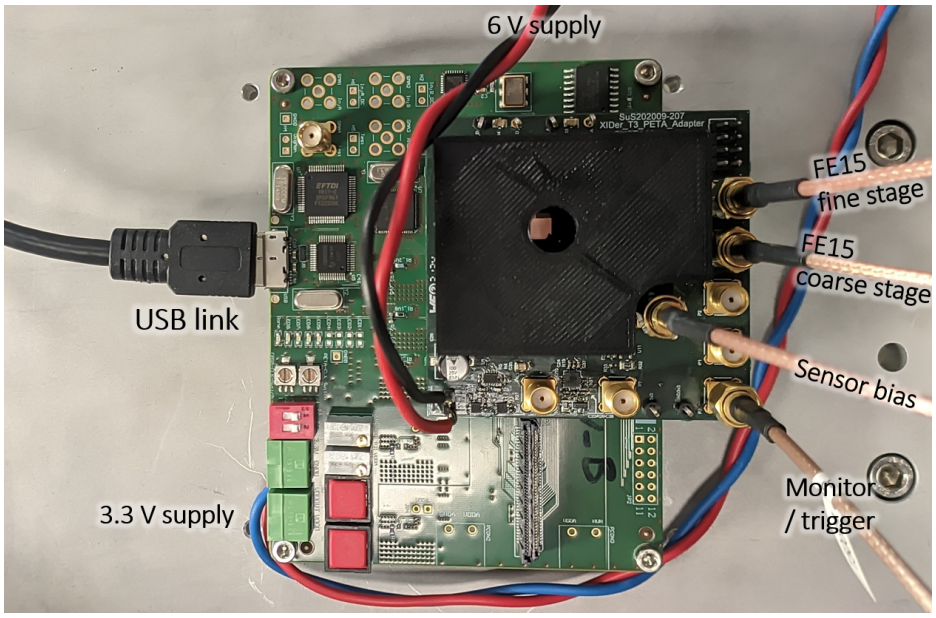



**Figure 3.12.** PETA data acquisition system, supplying power to the mezzanine card. Data transfer is performed by USB3. A custom-design 3D-printed plastic cover is used to protect the carrier PCB, only leaving a fitted sensor opening.

the PETA board, and also the 6 V to the mezzanine for the biasing of the sensor ground plane. An ISEG SHR high-voltage power supply is used to bias the sensor up to 2 kV. These power supplies are also controllable remotely through TCP/IP, which is particularly useful to automatise data acquisition procedures and to monitor, for instance, the sensor high-voltage current. For the analogue monitoring of the ASIC front-end, a high-bandwidth Teledyne-Lecroy WavePro 254HD oscilloscope is used. SMA to BNC cables are used to probe the voltage levels of the FE15 coarse and fine stage CSA output buffers, as well as trigger signals like the dynamically controlled Res0 switch.

## 3.4 Characterisation software

An elaborate Python package was developed at the ESRF to control and characterise the assemblies. It is organised in several modules, including: a Python-hardware interface, mainly implemented by Heidelberg University, an acquisition module, calibration and data-taking analysis modules, and a data saving module. Using this package, one can easily program the DACs and sequencer tracks, perform calibrations, and perform any other measurements with a XIDer assembly. All data and metadata can be automatically saved in HDF5 files.

**Example: Noise and baseline of the comparator threshold**

To illustrate the ease of use of this software, the experimental calculation of the baseline and noise of the comparator threshold, a typical measurement routinely performed on new assemblies, is used as an example.

In practice, the equivalent noise charge (ENC, as first introduced in Subsection 2.2.2) in the first stage can be measured at the comparator threshold level by performing a DAC:*COMP0* sweep. Here, only the coarse stage is used, with the transfer switch $S_2$ being always open. The coarse stage is reset periodically every 2 µs, therefore a subframe duration of 2 µs is used. In each subframe before the reset, the charge pump is enabled for a short amount of time. If the voltage level at the amplifier output is above the comparator threshold at that time, the charge pump will trigger. When the threshold DAC:*COMP0* is set low enough, the charge pump will always trigger, and, on the other hand, the charge pump will never trigger if DAC:*COMP0* is set high enough. This transition is shown in Figure 3.13, showing the the likelihood of charge pump triggering for such a DAC:*COMP0* sweep. Assuming the noise at the amplifier output is Gaussian, the transition takes the shape of an error function, more precisely the complementary cumulative distribution function of a normal distribution $\mathcal{N}(\mu, \sigma^2)$. Threshold scans in a photon-counting detector are typically analysed with the s-curve fitting method [108]. For this dataset, the following fitting function is used:

$$f_{fit} : x \mapsto \frac{1}{2}\left[1 - erf\left(\frac{x-\mu}{\sigma\sqrt{2}}\right)\right] \tag{3.1}$$

The fitting is successful on Figure 3.13, and the comparator threshold noise should be indeed close to Gaussian. For this specific front-end, FE05, the fitted ENC is $\sigma = 1.10\,\text{ADU}$ rms. Assuming that the design of DAC:*COMP0* is ideal with $1\,\text{ADU}_{COMP0} = 1\,\text{mV}$, this translates to a $1\sigma$ noise of 1.10 mV rms or $344\,\text{e}^-$ rms. For comparison, noise simulations of the T4 front-end show that the implemented amplifier design is expected in the voltage output of the amplifier to have a $1\sigma$ ENC of $350\,\text{e}^-$ rms. In a CdTe detector with $\epsilon_{CdTe} = 4.43\,\text{eV}$, this is equivalent to 1.55 keV rms, or approximately 5 % of a 30 keV photon. This is low enough to maintain single-photon sensitivity with this chip when setting the threshold at the half-photon level or above, as simulated in Subsection 2.2.2.

This fitting also provides the baseline of the coarse stage, which is the average value in units of $ADU_{COMP0}$ of the coarse stage amplifier output. For FE05, the baseline of the coarse stage is $\mu = 438\,\text{ADU}$.

Using the developed software, this procedure would be executed by these few lines of code:

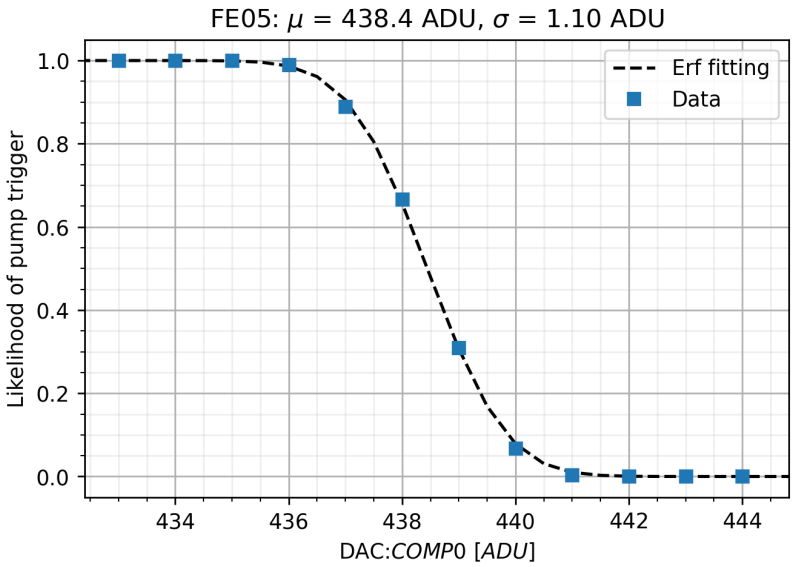



**Figure 3.13.** ENC measurement of front-end 5 using a DAC sweep of the coarse stage comparator threshold with error function fitting, giving $\sigma = 1.10$ ADU rms. For each DAC value, the likelihood of the charge pump triggering is shown, as an average over 20000 subframes.

```
# Define parameter dictionary
pars = {'assembly' : 'PAT25',                  # Assembly name
  'xider_config' : 'config.ini',       # Configuration ini file
  'data_file' : 'baseline_COMP0.h5'}   # Path for data saving
# Establish communication with hardware
xider = XiderT4()
# Program xider, perform sweep of DAC:COMP0 and save data file
calib = Calibration(xider, pars)
calib.baseline('BL0')
# Instantiate analysis class and perform erf fitting of sweep
analysis = CalibrationAnalysis(pars)
analysis.baseline('BL0')
```

## 3.5 Sensor-ASIC assemblies

### 3.5.1 Hybridisation procedure

CdTe starts degrading at temperatures over 150 °C [109], therefore, the conventional hybridisation method of solder flip-chip cannot be employed. The company Polymer Assembly Technology (PAT) provides a solution for low-temperature flip chipping: adhesive bonding using conductive epoxy [110]. All XIDer prototype assemblies mentioned in this work have been hybridised at PAT, hence the naming of the assemblies

taking the form of "PAT" plus a chronological numbering (see Appendix 7.1).

The $4 \times 4$ mm$^2$ sensor is significantly larger than its surface of contact with the ASIC. Only the pads of a 16-pixel matrix and its 2 surrounding ground plane pads are to be bonded to the ASIC. These pads represent a small portion of the sensor surface. To prevent mechanical stress from a cantilevered sensor, a custom-designed ULTEM plastic carrier is used to support the sensor-ASIC assembly, as shown in Figure 3.14. Prior to hybridisation, PAT mounts the ULTEM carrier to the carrier PCB with epoxy, and the ASIC chip to the ULTEM carrier. The ASIC is then gold wire bonded to the carrier PCB.

The complete hybridisation procedure performed by PAT is the following one:

1. Double gold stud bumping is carried out on 18 pads of the ASIC: 16 pixel pads + 2 surrounding ground plane pads, from either the 100 µm or 200 µm structures. As depicted by Figure 3.15, the same ASIC corner has the pads for both structures. The nominal bump height is 45 µm.

2. A conductive epoxy is applied directly on the CdTe sensor pads with a stencil printing technique.

3. The epoxy-bumped sensor is flipped, aligned and pressed on the gold studs of the ASIC.

4. The hybridised ASIC-sensor assembly is under-filled with (non-conductive) epoxy for mechanical rigidity.

Following sensor-ASIC hybridisation, the high-voltage connection is performed by wire bonding a corner of the CdTe sensor cathode to the PCB pad providing the high-voltage. Figure 3.16 shows examples of a completed 100 µm and 200 µm assemblies, mounted on their respective carrier PCB. The sensor covers a larger portion of the ASIC when the 200 µm-pitch pixel matrix is bonded, as shown also by Figure 3.15.

### 3.5.2 Hybridised assemblies of interest

A complete list of all hybridised XIDer assemblies produced up to the date of writing is given in Appendix 7.1. 25 assemblies have been produced with the ASIC T4 version. Before that, 17 assemblies were produced with a previous iteration of the chip « ASIC T2 » [99,111,112]. This earlier ASIC prototype did not have some key functionalities of ASIC T4, such as subframe trigger, synchronisation, and 16-channel parallel readout. XIDer assemblies with Schottky CdTe and GaAs:Cr sensors were first produced, with

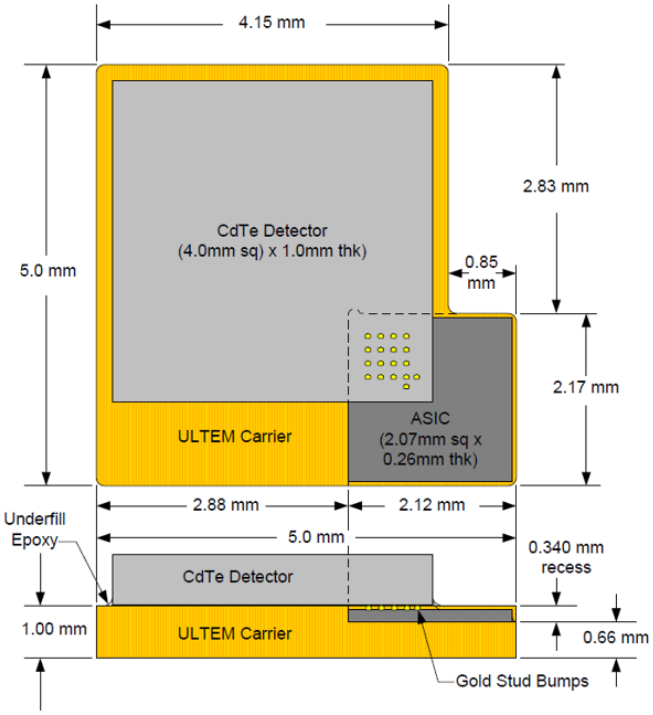



**Figure 3.14.** Schematic of sensor-ASIC hybridisation process.

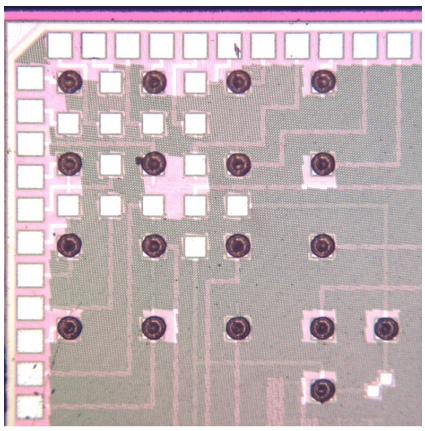
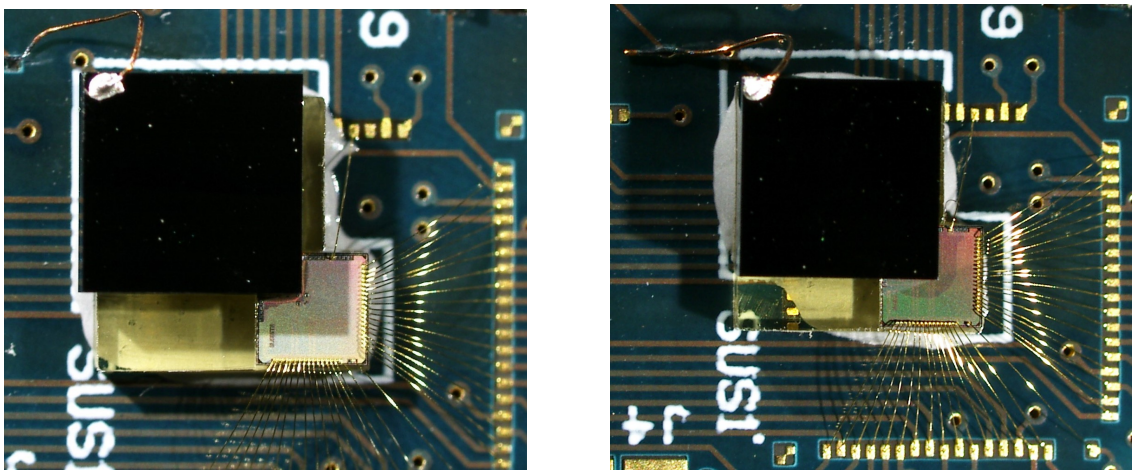


**Figure 3.15.** Gold studs applied to 200 µm structure pads.

Ohmic CdTe proving to be the most reliable and stable sensor material for the X-ray energy range of interest. 5 XIDer assemblies with a high-flux capable CdZnTe sensor were produced at a later time, once the material became available for purchase. In the next sections, only measurements using XIDer prototypes with an ASIC T4 chip and either an Ohmic CdTe sensor or a high-flux CdZnTe sensor will be shown. PAT18, PAT21, PAT25, and PAT39 were specifically picked for advanced characterisation because of their spatially uniform response to illumination.

## 3.6 Light sources used for characterisation

Since the final detector system is intended to be used under high-energy monochromatic X-rays, it is a mandatory step to characterise the XIDer prototypes in a relevant synchrotron beamline. As part of the ESRF Detector Unit, the XIDer team has dedicated slots per year to test the prototype assemblies in the ESRF beamline BM05. Outside of these few slots, in-lab characterisation can be routinely performed using an X-ray generator or other light sources, notably light-emitting diodes (LED). X-ray generators output a wide polychromatic spectrum and thus do not represent the real use-case scenario for this detector. Since CdTe and CdZnTe are sensitive to visible light, LEDs in the visible spectrum are preferred for the in-lab characterisation.



**(a)** 100 µm pixel pitch assembly **(b)** 200 µm pixel pitch assembly

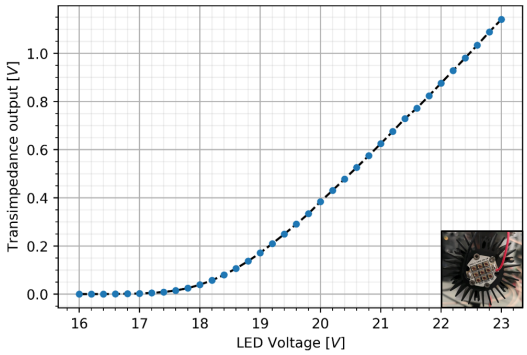
**Figure 3.16.** Pictures of two CdTe sensor-ASIC assemblies mounted on their carrier PCB.

### 3.6.1 Visible LED in-lab setup

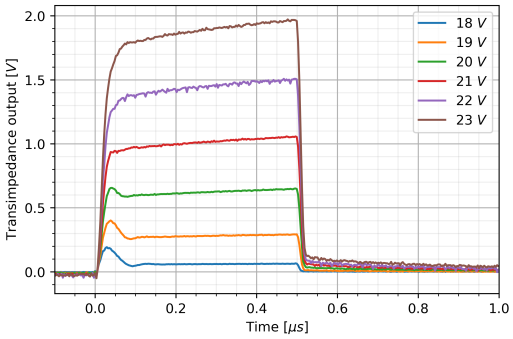
A commercial *ILH-ON09-FRED-SC211-WIR200* compact LED module comprised of an array of nine 730 nm LEDs is routinely used to characterise the light sensitivity of hybridised assemblies. A wavelength of 730 nm represents a photon energy of 1.70 eV, which is above the band gap energies of CdTe and CdZnTe (around 1.5 eV at room temperature) [113, 114]. Visible light illumination should emulate accurately low-energy X-ray illumination in CdTe/CdZnTe, as they are both absorbed superficially in the sensor material. It is an appropriate light source for the characterisation of the front-ends under illumination. This light source is characterised with a silicon photodiode, to provide the reference profile shown in Figure 3.17a. The LED module can be controlled with a waveform generator via a custom-designed PCB to provide a modulated light output. The LED light output can then be modulated with a Gaussian noise to provide a time-varying tunable light output, or with a square waveform to provide a short light pulse. For instance, Figure 3.17b shows the waveforms recorded by a silicon photodiode when turning on the LED for 500 ns. While the detected pulse profiles do not quite resemble square waveforms, these pulses are still mostly confined over that 500 ns time window, with aftersignals rapidly reaching negligible values. In that way, a LED pulse can be synchronised and provided during a single XIDer subframe, which is essential for the later probing of signal-induced sensor leakage.

### 3.6.2 Beamline setup

During allocated time slots of a few days, XIDer prototypes are tested at the BM05 beamline under the ESRF machine X-rays. The schematic of the setup is drawn on




**(a)** DC light output versus bias voltage




**(b)** Waveforms of 500 ns light pulses for different LED bias voltages

**Figure 3.17.** Characterisation of the LED module with a silicon photodiode. Graph (a) shows the non-linear dependency of the LED light output with its bias voltage. Graph (b) shows the waveforms retrieved with the photodiode, when the LED is controlled with a 500 ns square signal.

Figure 3.18, and Figure 3.19 shows a picture of the detector prototype system in place in the beamline hutch. The machine beam is first filtered using the beamline silicon monochromator to a chosen photon energy between 20 and 100 keV. A multi-layer monochromator can be used to have an increased flux output, at the expense of beam uniformity and a lengthy energy calibration. The beam size, typically on the scale of 1 $mm^2$, is regulated with the primary and secondary slits built in the beamline. A beamviewer is used to shape the beam as desired, with an example beam given by Figure 3.20.

The beam flux can be adjusted in two ways. It can be detuned using the beamline control software *bliss*. This method changes the flux in a few seconds, with the beam position also varying slightly in the process. To attenuate the beam flux on the fly, a set of remotely controllable filter boxes is used. The filters inside the boxes are put into the beam path by a mechanical air-pressured system. The filter material employed depends on the beam energy set as to provide the appropriate level of attenuation, and is typically aluminium for a 20 to 30 keV X-ray beam or molibdenum for higher X-ray energies. The hybridised assembly of choice, mounted on the DAQ system, is on the other side of the hutch installed on a translating stage. As the prototype detector is a few meters away from the 1 $mm^2$ beam, centring the detector on the beam is tricky and usually performed using a laser alignment system.

In front of the detector is placed a 500 µm-thick silicon photodiode that measures a current proportional to the beam flux and provides a reference that can be compared to XIDer data. Equation 3.4 gives the derivation of the number of photons $N_{ph}$

arriving on the detector prototype during a subframe of duration $\Delta t_{XIDer}$ from the measured photodiode current. Indeed, the current $I_{diode}$ measured by this diode can be expressed by equation 3.2, and the flux on the XIDer prototype $\Phi XIDer$ behind the diode by equation 3.3, where:

- $e = 1.6 \times 10^{-19}$ C is the electron charge
- $E_{ph}$ is the photon energy in $eV$ (or $eV/ph$)
- $\epsilon_{Si} = 3.61$ eV is the pair creation energy in silicon
- $\eta_{diode}$ is the absorption efficiency of the photodiode at energy $E_{ph}$
- $\eta_{air}$ is the absorption efficiency of air at energy $E_{ph}$ for the distance separating diode and XIDer prototype
- $A_{beam}$ is the area of the beam spot on the diode in $mm^2$
- $A_{pixel}$ is the XIDer pixel area in $mm^2$
- $\Delta t_{XIDer}$ is the XIDer subframe active integration window in $s$
- $I_{diode}$ is the picoammeter measurement of the diode photocurrent when illuminated, and $I_{dark}$ in dark conditions, in $A$
- $\Phi_{diode}$ is the X-ray photon flux arriving on the diode in $ph/s/mm^2$
- $\Phi_{XIDer}$ is the X-ray photon flux arriving on the XIDer prototype in $ph/s/mm^2$

$$I_{diode} = I_{dark} + e\ \frac{E_{ph}}{\epsilon_{Si}}\ \eta_{diode}\ A_{beam}\ \Phi_{diode} \tag{3.2}$$

$$\Phi_{XIDer} = (1 - \eta_{diode})(1 - \eta_{air})\ \Phi_{diode} \tag{3.3}$$

$$N_{ph} = \Phi_{XIDer}\ A_{pixel}\ \Delta t_{XIDer} = \frac{I_{diode} - I_{dark}}{e\ \frac{E_{ph}}{\epsilon_{Si}}}\ \frac{1 - \eta_{diode}}{\eta_{diode}}(1 - \eta_{air})\ \frac{A_{pixel}}{A_{beam}}\ \Delta t_{XIDer} \tag{3.4}$$

The XIDer computer, directly connected by USB to the detector, is in the hutch next to the oscilloscope that provides the monitoring of the chip signals. Both instruments are well shielded with lead panels and are controlled remotely from a computer in the BM05 control room behind thick shielding walls. Every element in the setup was designed to be controllable via the *bliss* software so that, once the alignment is made and the filter boxes are in place, all measurements can be performed from the control room.

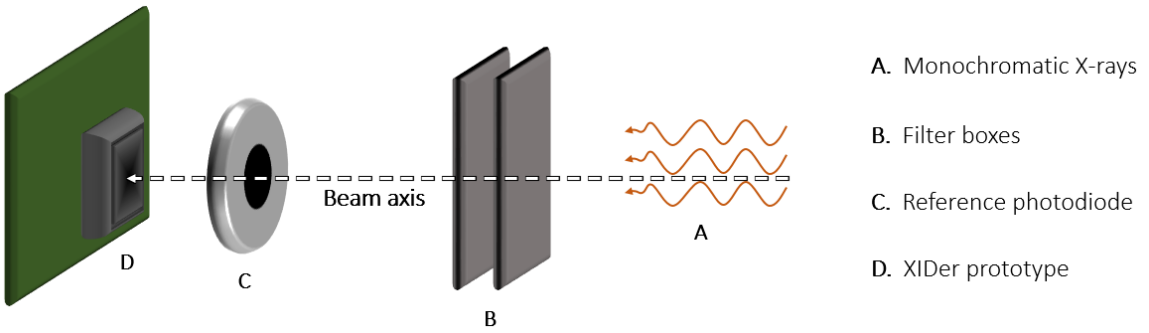



**Figure 3.18.** Schematic of the BM05 beamline setup. The flux of the monochromatic X-ray source is adjusted with a set of filters. The XIDer prototype is placed directly behind a 500 µm-thick silicon photodiode providing a flux reference.

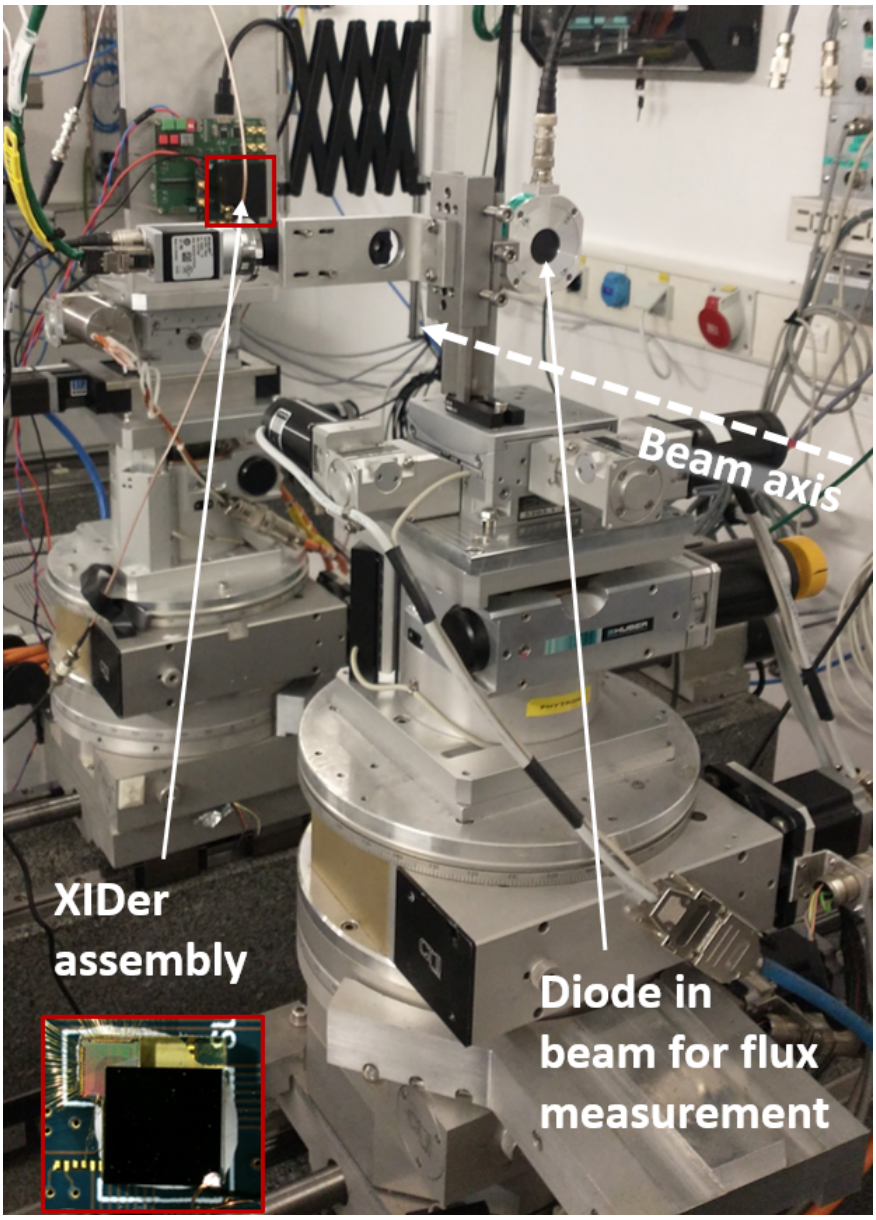



**Figure 3.19.** Picture of the BM05 beamline setup.

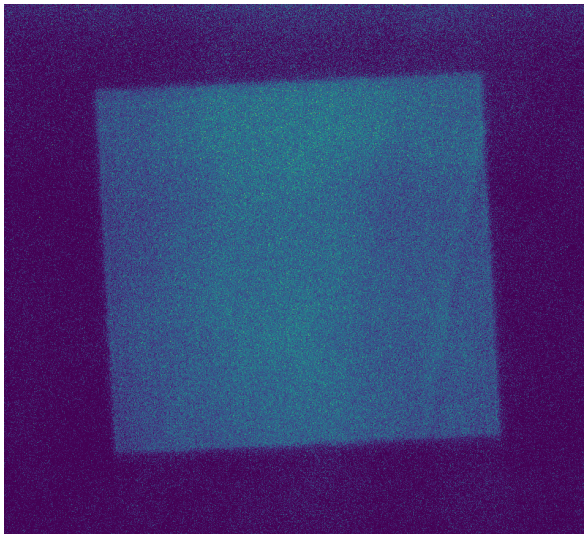


**Figure 3.20.** Image of the slitted X-ray source captured with a Basler scintillator-based beamviewer with 1.875 µm effective pixel size. Here, the beam is measured to be 635 px × 590 px = 1.19 mm × 1.11 mm.

# Chapter 4

# Calibration

For the proper functioning of the XIDer detector at a given photon energy, each front-end must be calibrated so that the coarse stage handles charge packets of 8 photons and the fine stage charge packets of 1 photon. This concept was introduced in Subsections 2.2.1 and 3.1.2. A thorough calibration study is needed to provide input for the iterative process that is detector system research and development. The calibration procedure should be automated, fast, and scalable to larger systems with millions of pixels. This chapter presents the procedures and assessment of a first-level calibration relying on the internal injection circuit of the XIDer ASIC T4.

## 4.1 Calibration procedure

In each front-end, four parameters must be calibrated, all depicted in Figure 4.1: the comparator thresholds *COMP0* and *COMP1*, and the charge pump packet sizes *CP0* and *CP1*. Since the calibration procedure needs to be fast and scalable, it cannot rely entirely on synchrotron-generated X-rays, which are not frequently available. An internal charge injection circuit is present in the ASIC design purposely to emulate a monochromatic X-ray source, and can be used to provide a first level of calibration. As discussed in this section, the use of internal injection has limitations, however, it provides a calibration that is acceptable to proceed with the characterisation of XIDer prototypes. A refinement of this calibration would require the use of a source of precisely known energy and taking into account the physical effects at work during the process, including fluorescence, charge trapping/detrapping and charge sharing. Such a refined calibration procedure is out of the scope for this work.

In this section, this first-level calibration procedure, based on the use of the internal injection circuit inside the ASIC, is described. After the initial calibration of the injection circuit, the comparator threshold and the charge pump packet size can be

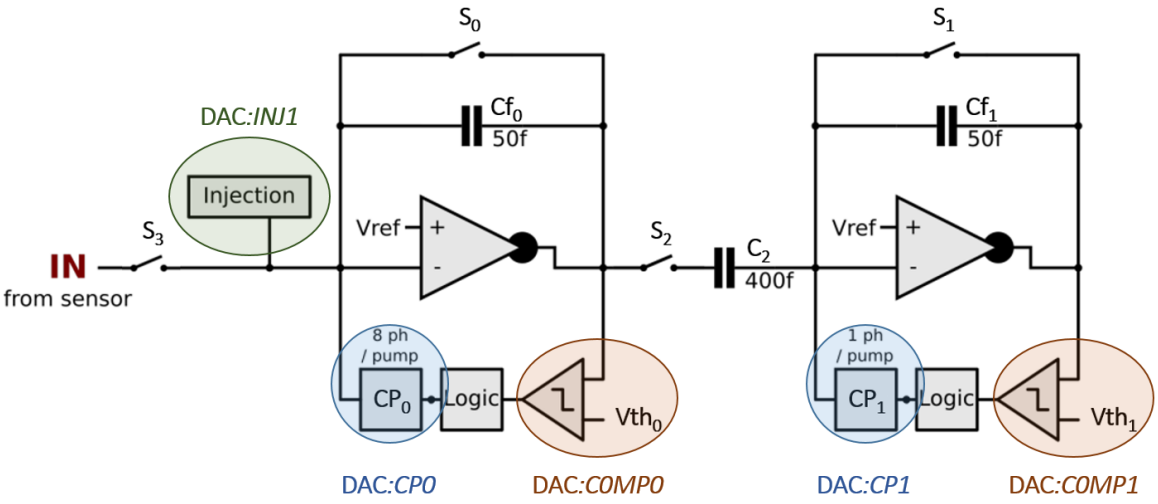



**Figure 4.1.** Schematic of ASIC T4 two-stage pixel front-end, with the DACs to be calibrated are highlighted. First, the shared injection circuit DAC:*INJ1* is calibrated. Then for each front-end, the thresholds DAC:*COMP0*, DAC:*COMP1* and the charge pump packet sizes DAC:*CP0*, DAC:*CP1* are calibrated. From [99] (modified).

calibrated for both stages of each channel.

### 4.1.1 Calibration of the internal injection circuit

When the internal injection is enabled, the amount of charge injected into the front-ends is controlled by the 10-bit DAC:*INJ1*. The calibration of the comparator thresholds and the charge pump packet sizes relies on the injection of charge equivalent to whole numbers of photons. The conversion factor from units of $ADU_{INJ1}$ to units of photon energy must, therefore, be known first. To probe the highest dynamic range possible, both the small and large injection capacitors are used in parallel, amounting to a total injection capacitance of 180 fF (see Subsection 3.1.3).

DAC:*INJ1* is swept over its 10-bit range. For each value of *INJ1*, the front-end baseline after integration of the injected charge pulse is measured, using the mean value $\mu$ of an error function fit to the DAC:*COMP0* sweep, as presented in Section 3.4. Figure 4.2 shows a plot of the retrieved DAC:*COMP0* versus DAC:*INJ1*. The slope of the linear regression, represented as a dashed black line, is the conversion factor in units of $ADU_{COMP0}/ADU_{INJ1}$, equivalent to units of $mV/ADU_{INJ1}$. Indeed, by design of the coarse stage comparator threshold DAC, a difference of 1 $\mathrm{ADU}_{COMP0}$ is a difference of 1 mV in the front-end voltage output. This means that for the front-end example shown, an injection pulse of size 1 $\mathrm{ADU}_{INJ1}$ translates to a baseline shift of 3.43 mV. The behaviour is linear for values of *INJ1* below approximately 110 ADU, at which point it becomes super-linear. For values of *INJ1* above 160 ADU, the retrieved

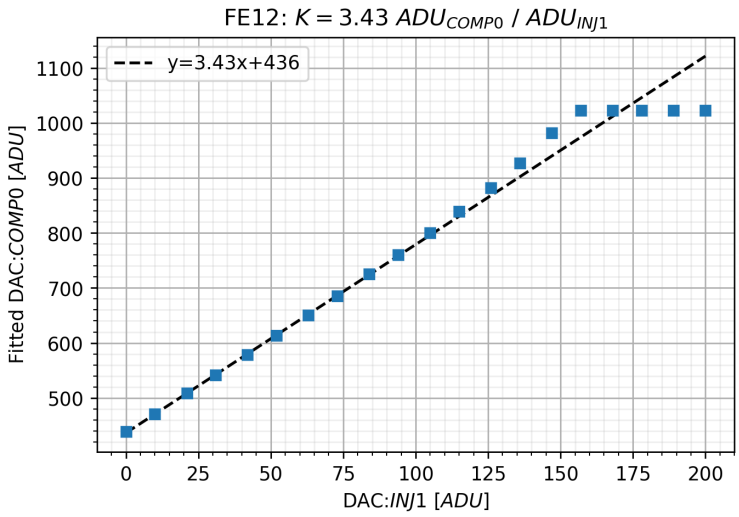



**Figure 4.2.** Sweep of injected charge pulse size DAC:*INJ1*. For each DAC value, the baseline in ADU is found with a sweep of DAC:*COMP0*.

baseline plateaus at $COMP0 = 1023$ ADU, the upper limit of the 10-bit DAC.

To compute the conversion factor into the useful units of $ph/ADU_{INJ1}$, this value must be renormalised by the front-end voltage increase expected after the integration of 1 ph in the coarse stage, given by Formula 4.1, where:

- $E_{ph}$ is the photon energy in $keV$
- $e = 1.6 \times 10^{-19}$ C is the electron charge
- $\epsilon$ is the electron-hole pair creation energy in $eV$ in the material in question ($\epsilon_{CdTe} = 4.43$ eV, $\epsilon_{CdZnTe} = 4.64$ eV [95])
- $C_f = 50$ fF is the front-end feedback capacitor
- $CCE$ is the charge collection efficiency

$$V_{1\,\mathrm{ph}} = E_{ph} \times \frac{e}{\epsilon\ C_f} \times CCE \tag{4.1}$$

Assuming 99% charge collection efficiency in 1-mm CdTe (see Subsection 2.1.3), the voltage increase after one 30 keV photon is integrated in the front-end is calculated to be $V_{1\,\mathrm{ph}} = 21.5$ mV. The conversion factor derived from Figure 4.2 is $K = 3.43\,\mathrm{mV/ADU}_{INJ1} = 0.160\,\mathrm{ph/ADU}_{INJ1}$.

This procedure is repeated for each of the 16 front-ends to take into account dispersion of the feedback capacitors, mentioned in Subsection 4.2.3. With the conversion factor derived for all channels, the following sections will mention injected charge directly in units of equivalent photons.

#### A priori assumptions

The calculation of the conversion factor from the DAC:*INJ1* sweep is based on three assumptions:

- $1\,\mathrm{ADU}_{COMP0} = 1\,\mathrm{mV}$. This is the nominal value from the design of the coarse stage comparator threshold DAC:*COMP0*. In reality, there is a $\pm 10\%$ uncertainty on this value because of the quoted resistor tolerance in the DAC circuit.
- $C_f = 50\,\mathrm{fF}$. The feedback capacitors used in the front-ends have a quoted tolerance of $\pm 10\%$ of the 50 fF nominal value.
- $\epsilon_{CdTe} = 4.43\,\mathrm{eV}$. This value is well accepted value in the community [95].

The uncertainty around these components nominal values are in reality hard to determine precisely, as they are technology-dependent and not provided by the foundry. According to certain sources, the uncertainties could be as high as $\pm 20\%$ of the nominal value [115, 116]. A cumulative uncertainty of $\sqrt{(\frac{\Delta R_{COMP0}}{R_{COMP0}})^2 + (\frac{\Delta C_f}{C_f})^2} = \sqrt{10^2 + 10^2} = 14.1\%$ is expected in the calibration of the internal injection given the quoted uncertainties. This uncertainty impacts the final calibration, but it was considered acceptable to proceed with assembly characterisation.

### 4.1.2 Calibration of the threshold

#### Coarse stage

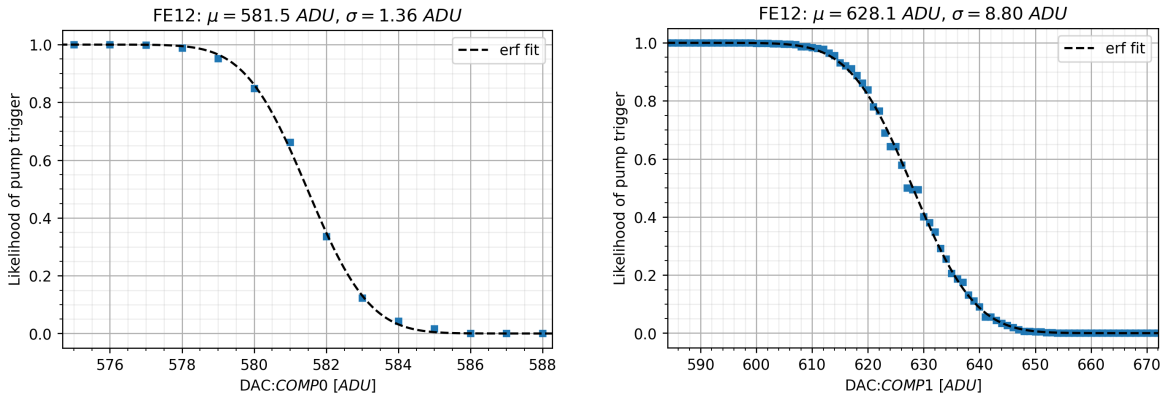
The coarse stage charge pump should trigger as soon as the front-end voltage reaches an equivalent of 8 photons above its baseline. The coarse stage comparator threshold, controlled by DAC:*COMP0*, is swept over its 10-bit range under the injection of charge equivalent to 8 photons in each subframe. The procedure presented is similar to the procedure explained in Section 3.4, but here with injection. Figure 4.3a shows an example DAC sweep: over the range of about 10 ADU, the coarse stage charge pump goes from pumping in all subframes to pumping in none of the N subframes. The transition is fitted with an error function with parameters $\mu$ and $\sigma$. The calibrated threshold is set when there is a 50% likelihood of charge pump trigger, which is the $\mu$ of the fit.

#### Fine stage

The fine stage charge pump should trigger as soon as the front-end voltage reaches an equivalent of 1 photon above its baseline. Similarly, the fine stage comparator threshold, controlled by DAC:*COMP1*, is swept over its 10-bit range under the injection

equivalent to 1 photon in each subframe. The calibrated threshold is calculated with an error function fit. As shown in Figure 4.3b, the transition happens over a wider range of ADU than the coarse stage since the gain between coarse and fine stages also amplifies the noise by a factor 8.

In this case, the threshold is chosen at the whole photon level. A threshold slightly below 1 photon can also be chosen, for instance at the half-photon level to emulate mid-tread type uniform quantisation.




**(a)** Coarse stage: injection of 8 ph

**(b)** Fine stage: injection of 1 ph

**Figure 4.3.** DAC sweep of the comparator thresholds with an error function fit. For each DAC value, the likelihood of the charge pump triggering is shown, as an average over 20000 subframes.

### 4.1.3 Calibration of the charge pump packet size

#### Coarse stage

The coarse stage charge pump should remove a charge packet of an equivalent 8 photons to match the coarse stage threshold, previously calibrated to 8 ph for the channel in question. The coarse stage charge pump packet size, controlled by DAC:*CP0*, is swept over its 10-bit range under an injection of 64 equivalent photons in each subframe. The injection value of 64 photons is used as it is a multiple of 8 photons: the charge pump should trigger exactly 8 times to remove the injected charge. Other multiples of 8 could be chosen for this procedure, provided that the injection stays in its linear regime, where the conversion factor remains meaningful. To minimise any low-to-high non-linearities, a midrange value of photons was chosen.

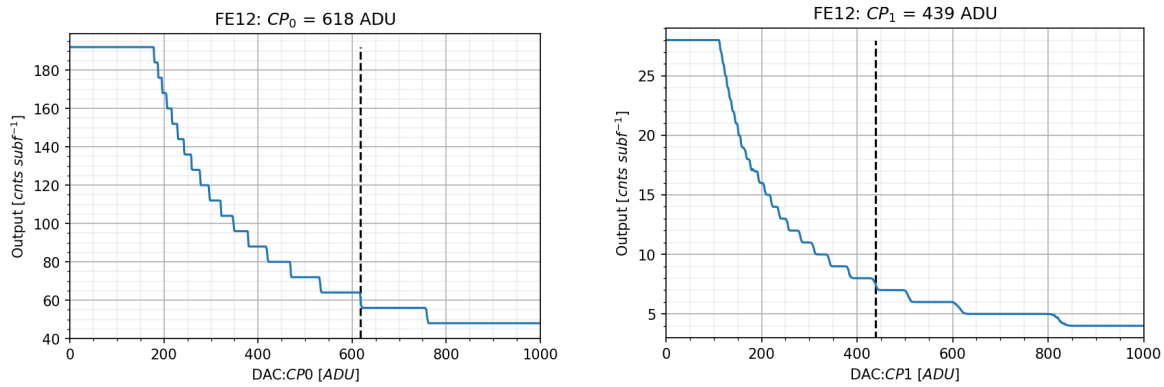
Figure 4.4a shows an example of such a DAC sweep. If the charge packet size is set too high, the charge pump removes the injected charge in too few triggers meaning the stage outputs values below 64. As the charge packet size is decreased, additional

charge pump triggers are needed to remove the injected charge, translating in steps of 8 counts in the figure. In this specific sequencer configuration, the charge pump has time to trigger only 24 times to remove charge before the stage is reset, which is why a saturation at $24 \times 8 = 192$ counts is observed for values of charge packet sizes below 180 ADU. Supposing a low enough front-end noise, the ASIC counts exactly 64 in a certain range of *CP0* values. The calibrated charge packet size is the maximum DAC value for which the ASIC counts 64. To handle a larger noise, the calibrated charge packet size is set at the transition between the pump triggering 8 times and 7 times, as indicated by the black dashed line in Figure 4.4a.

### Fine stage

The fine stage charge pump should remove a charge packet equivalent to a single photon. The fine stage threshold is set at the previously calibrated 0.5–1 ph value for the channel in question. Similarly, the fine stage charge pump packet size, controlled by DAC:*CP1*, is swept over its 10-bit range under the injection of charge equivalent to 8 photons in each subframe. The charge pump of the coarse stage is disabled, so that the injected charge is directly transferred to the fine stage. The charge pump of the fine stage should trigger exactly 8 times to remove the injected charge in packets of 1 photon.

As shown in Figure 4.4b, the results are analogous to those of the coarse stage, but with steps of 1 count per subframe. The calibrated charge packet size is set at the transition between the ASIC recording 8 counts and 7 counts, highlighted by the dashed line.




**(a)** Coarse stage: injection of 64 ph

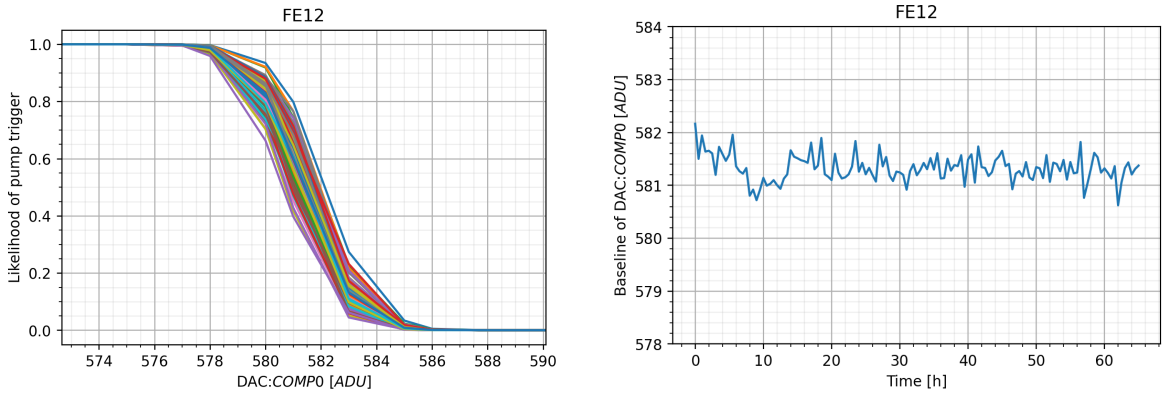
**(b)** Fine stage: injection of 8 ph

**Figure 4.4.** DAC sweep of the charge pump packet sizes. For each DAC value, the digital output is recorded as an average over 20000 subframes.

## 4.2 Preliminary assessment

### 4.2.1 Baseline stability

To assess the stability in time of the threshold calibration, the procedure was repeated for both stages every 30 minutes for 65 hours. Figure 4.5 shows an overlap of the DAC sweeps for the coarse stage of front-end 12 and the time-dependence of the threshold derived from the error function fits. For this front-end, the $5\sigma$-variation of the calibrated threshold is $1.3\,\mathrm{ADU}_{COMP0}$ in the coarse stage and $12\,\mathrm{ADU}_{COMP1}$ in the fine stage. The $6\sigma$-variation in the coarse stage varies between channels, and is always found to be below $5\,\mathrm{ADU}_{COMP0}$, *i.e.* in CdTe an equivalent 7 keV photon or 23% of a 30 keV photon. IT should be noted that the temperature of the assembly was not controlled during this experiment.




**(a)** Overlap of 131 DAC:*COMP0* sweeps.

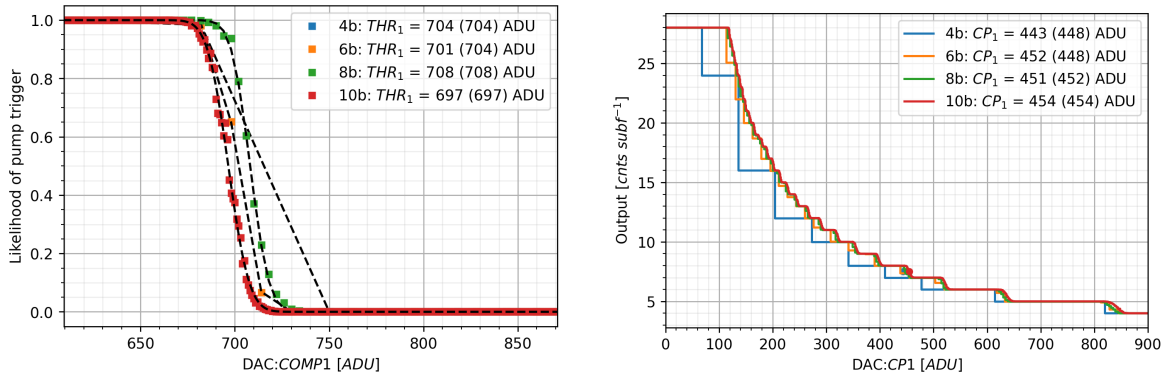
**(b)** Retrieved threshold versus time.

**Figure 4.5.** Stability with time of the coarse stage comparator threshold. A DAC:*COMP0* sweep is performed every 30 minutes for 65 hours.

### 4.2.2 Influence of DAC resolution

DACs *COMP0*, *COMP1*, *CP0* and *CP1* have a 10-bit resolution in the prototype system studied. The final, larger-scale system cannot have 10-bit DACs for space management and power consumption reasons. As part of the iterative prototype R&D, lower resolutions are investigated with this T4 system. Datasets shown previously have been complete scans of each DAC, where all 1024 values were tried. The DAC range are here probed with fewer values, for instance 256, 64, and 16 values, emulating 8-bit, 6-bit, and 4-bit resolution DACs respectively. Figure 4.6 shows an example comparison for the fine stage. Although the data curves get smoother as the resolution increases, the calibrated parameters are still retrieved with a good accuracy. The resolution

can be deemed sufficient as soon as the transitions and plateaus can be identified. A resolution to 6-8 bits (depending on the DAC in question) is found to be enough, which also speeds up the 16-channel calibration significantly.




**(a)** Threshold **(b)** Charge packet size

**Figure 4.6.** Calibration of the fine stage threshold and charge packet size, using different DAC resolutions. In legend appears the calibrated parameter on 10 bits, and in parentheses the value with the specified resolution remapped on 10 bits.

### 4.2.3 Dispersion of individual calibrated parameters

#### Conversion factor

Figure 4.7 shows for PAT38 (200 µm pitch CdTe assembly) the calibrated internal injection conversion factor for all front-ends. For this assembly, the conversion factor is found to be 3.42 mV/ADU in average over the 16 channels, with a standard deviation of 70 µV/ADU or 2% of the mean value. This spread is explained by the dispersion between channels of the feedback capacitors, typically on the order of a few percent.

Additionally, the value of the conversion factor can be cross-checked for front-end 15, the only front-end whose output can be directly monitored. For this accessible front-end, the coarse stage output voltage level can be measured on an oscilloscope, averaging over thousands of subframes to reduce noise. Then, the DAC:*INJ1* sweep can be re-performed, measuring manually with the oscilloscope for each DAC value the voltage level following injection. Using the second method for assembly PAT38, the conversion factor of FE15 is measured to be 3.12 mV/ADU, which is 7% lower than the value from Figure 4.7. These values are in agreement as they stand below the 10% uncertainty originating from assuming $1\,\mathrm{ADU}_{COMP0} = 1\,\mathrm{mV}$.

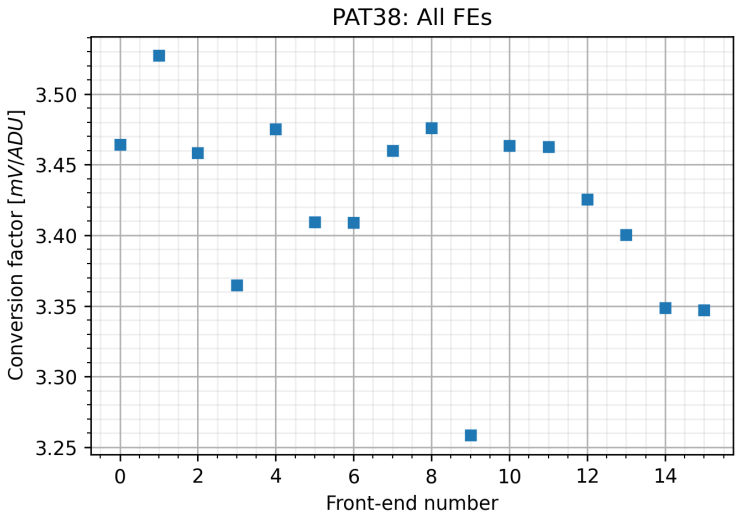


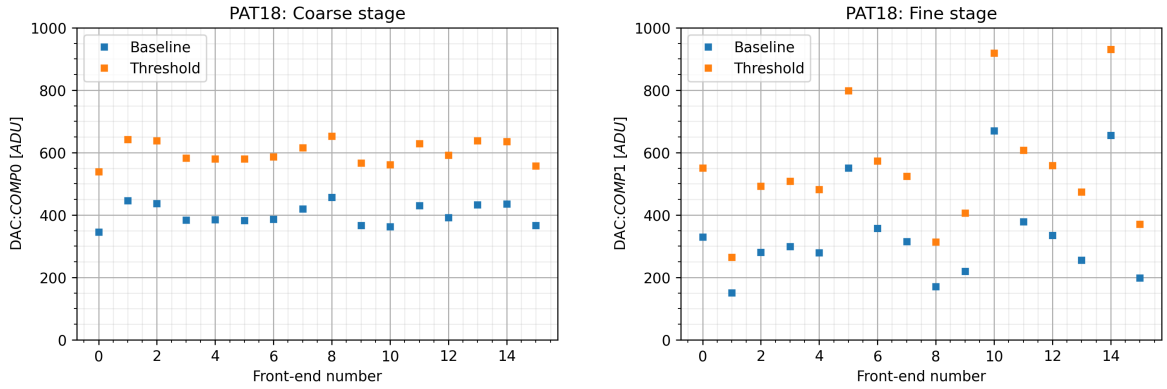

**Figure 4.7.** Internal injection conversion factors in $mV/ADU_{INJ1}$ for the 16 channels of assembly PAT38.

### Baseline/Threshold

Figure 4.8 shows for both stages of assembly PAT18 the calibrated baselines and thresholds. The thresholds are measured the same way as the baselines, but with a charge pulse injection of 8 and 1 photon for the coarse and fine stages respectively. Expectedly, the thresholds follow the same trend as the baselines, only shifted by a fixed amount originating from the injected charge. The baselines peak-to-peak dispersion in the coarse stage is approximately $100\,\mathrm{ADU}_{COMP0} \approx 100\,\mathrm{mV} \approx 5 \times 30\,\mathrm{keVph}$. In the fine stage this dispersion is approximately $500\,\mathrm{ADU}_{COMP1} \approx 500\,\mathrm{mV}$, with other assemblies showing similar results. This dispersion is higher than foreseen, and arises from fabrication mismatches between transistors in differential configurations, notably the comparators and the transfer switch. This is an issue with the design of this ASIC version — the operation regime being 300–500 mV — fixed in next iterations by having a larger surface on these critical transistors, reducing the fabrication mismatch.

### Charge pump packet size

Figure 4.9 shows for assembly PAT18 the calibrated charge pump packet sizes in the coarse and fine stages. A descending trend of both calibrated DAC:$CP$ with front-end number is observed, from around 650 ADU for FE0 to 450 ADU for FE15, a drop of approximately 30%. This trend, seen in all assemblies, is due to the parasitic resistance of the narrow DAC bias current line going from FE15 to FE0. The current drops from one front-end to the next, resulting in FE0 needing bigger DAC values




**(a)** Coarse stage baselines and thresholds (8 ph injection)

**(b)** Fine stage baselines and thresholds (1 ph injection)

**Figure 4.8.** Calibrated baselines (without injection) and thresholds (with injection) for the 16 channels of assembly PAT18.

than FE15 for the same effective charge pump packet size. This problem is fixed by increasing the width of the bias lines, thus decreasing the parasitic resistance and the current drop. Another option would be to use bias voltages instead of bias currents.

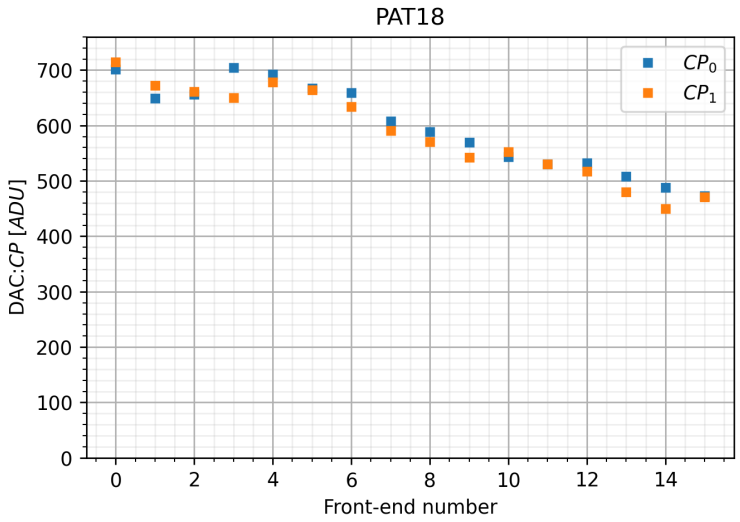



**Figure 4.9.** Calibrated charge pump packet sizes for both coarse and fine stages, for the 16 channels of assembly PAT18.

### 4.2.4 Dispersion of front-end linearity with internal injection

The digital output of all 16 front-ends is probed simultaneously against injection size, such as shown on Figure 4.10. This ASIC version has 16-channel readout but does not have per-channel trimming, which means that only one channel is perfectly

calibrated at a time. For Figure 4.10, the ASIC was trimmed with the calibrated *COMP0*, *COMP1*, *CP0*, and *CP1* DAC values of FE6. The counts trend for FE6, depicted as a dashed black line, is quite linear for the entire range explored here of 0–160 cnts subf$^{-1}$. The 15 other channels (coloured lines) are miscalibrated, which is highlighted by the presence of irregularities in the lines. Front-ends 7–15 standing below the dashed line always count less than the calibrated front-end 6, as these are trimmed for higher DAC:*CP* values than their calibrated values, in accordance with the trend shown in Figure 4.9. Likewise, FEs 0–5 count more than FE6. Offsets of a few counts in the digital outputs can also be noticed, resulting from the disparities in thresholds discussed previously.

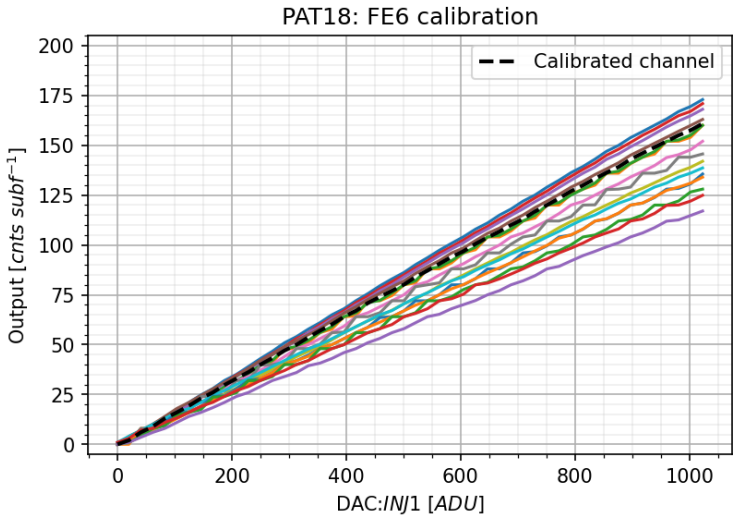



**Figure 4.10.** Digital output of assembly PAT18 for different values of injection, recorded as an average over 20000 subframes. The complete 16-channel output is shown, but the system is trimmed only for FE6.

These large disparities in calibrated DAC values are a big limitation to the 16-channel readout of this ASIC iteration. Per-channel trimming is planned for the next ASIC iterations. For this T4 iteration, a workaround is still possible by applying an offset and a slope correction to the 15 miscalibrated channels so that they overlap the calibrated channel in plots like Figure 4.10.

## 4.3 Calibration assessment with charge injection

To thoroughly assess the calibration procedures, the ASIC is first considered by itself, in order to eliminate potential side-effects caused by the sensor that is hybridised to the ASIC. In this section, the sensor is always disconnected from the front-end electronics with the use of the input switch $S_3$, as depicted in Figure 4.1.

### 4.3.1 Assessment with internal injection circuit

Similarly to the previous section, the digital output of a calibrated front-end is measured for increasing values of input charge injected internally. This front-end was calibrated for a photon energy of 30 keV, and the threshold of the fine stage was set at the half-photon level. The resulting DAC sweep, which can be interpreted as the ADC transfer function of the system, is given by Figure 4.11, where the coarse stage and the fine stage values, as well as the total value, are shown. Digitisation steps can be observed in the figure, as the smallest unit in the injected charge sweep is much lower than the charge equivalent to one 30 keV photon. These plateaus are apparent in the figure: plateaus with a step height of 8 ph for the coarse stage and 1 ph for the fine stage and also the aggregate output. The fine steps are centred on the integer numbers of injected photons because of the half-photon fine stage threshold level. The fine stage only takes values between 0 and 8, as it should. The digitisation process is seen to indeed replicate a mid-tread uniform quantiser, with the added influence of electronic noise smoothing the edges.

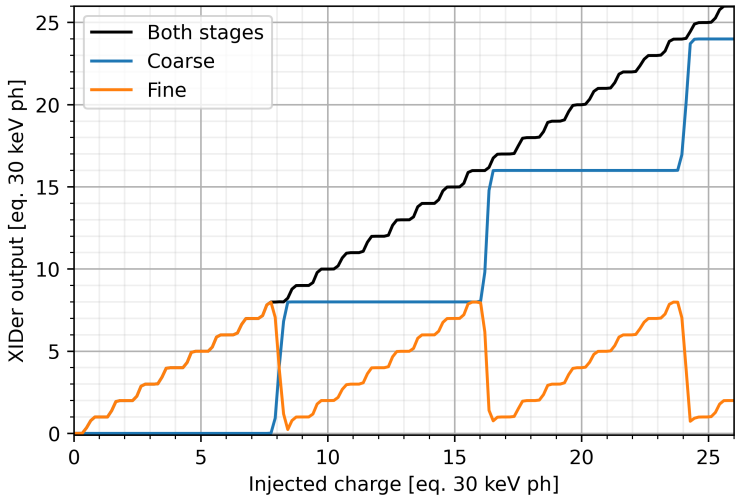



**Figure 4.11.** Digital output of calibrated front-end for different values of injection, recorded as an average over many subframes. The output from coarse and fine stages are also shown separately.

### 4.3.2 Assessment with external injection circuit

The internal injection circuit can only provide a fixed charge all at once during the subframe, that cannot be modulated in consecutive subframes. To assess the consistency of the calibration as a whole, it is worth investigating how an input distribution with a meaningful statistical spread is handled by the front-end electronics. As seen on

Figure 3.11, the mezzanine PCB is equipped with the functionality to inject charge externally through an SMA connector directly to the ASIC front-ends. The same circuit handles both internal and external charge injection and is detailed in Figure 3.3. The statistics of this Gaussian signal is tuned to have a Fano factor $F = \sigma^2/\mu = 0.7\,\text{ph}$, in order to emulate the charge distribution read out by the front-end when the sensor is illuminated with a Poissonian X-ray source (this is explained by charge sharing, see Subsection 2.1.6). Then, a calibrated front-end is programmed to acquire thousands of subframes under five increasing mean levels of Gaussian signal with $F = 0.7\,\text{ph}$.

The retrieved distributions of XIDer subframe output is shown by Figure 4.12. The coloured histograms are shown alongside their fits to a Gaussian probability density function represented in dashed black lines. The total number of subframes recorded is different for each distribution, therefore, the histograms are normalised in amplitude for presentation purposes.

Qualitatively, the shapes of the input Gaussian charge distribution are properly retrieved by the front-end electronics, and the output distributions closely match their respective Gaussian fit. This is a clear sign of a successful calibration for the front-end in use.

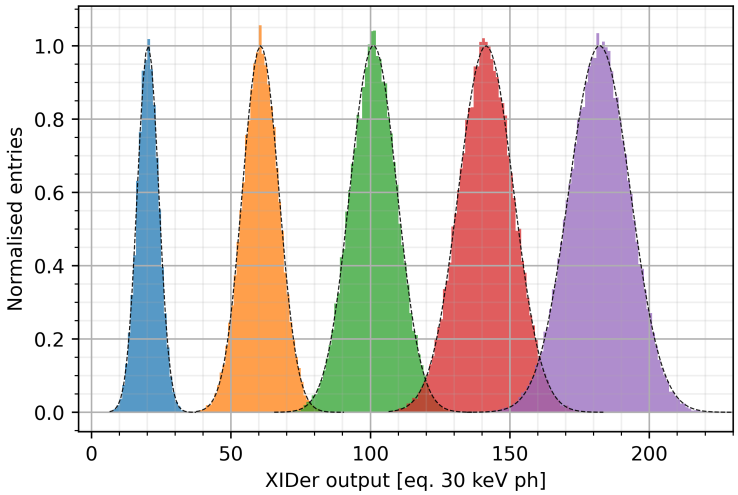


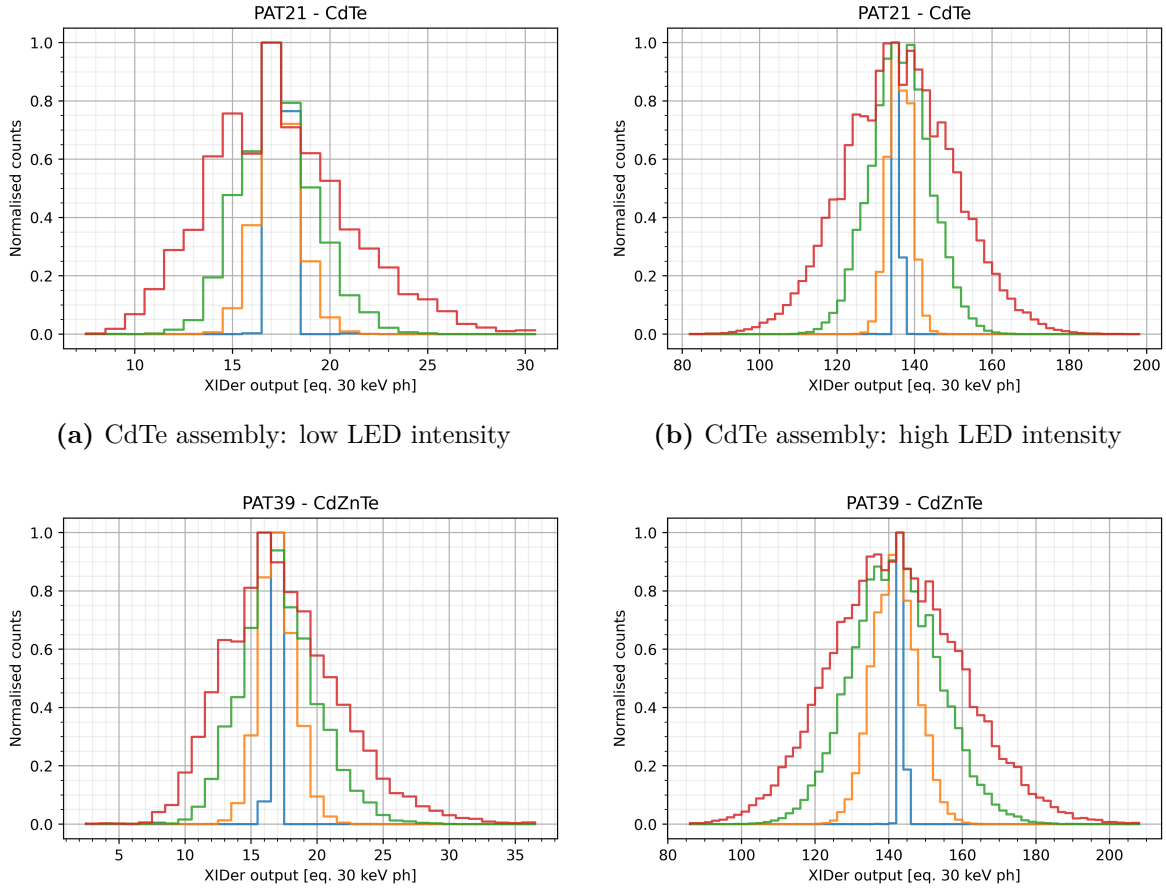

**Figure 4.12.** Normalised distributions of counts per subframe in calibrated front-end, for different external injections with Gaussian distribution. Each of the five histograms are shown alongside a fit of a Gaussian probability density function in black dashed line.

## 4.4 Calibration assessment with LED illumination

In a second step, the calibration is assessed using the whole detector system: an LED module, described in 3.6.1, is used to illuminate the biased sensor hybridised to the

assembly under testing. Two assemblies are investigated: PAT21, assembly with a 1-mm thick Ohmic CdTe sensor, and PAT39, assembly with a 2-mm thick CdZnTe sensor. Both assemblies have a pixel pitch of 200 µm. The CdTe assembly is biased with −500 V voltage and undergoes an initial 20 minutes of stabilisation without illumination. The CdZnTe assembly is biased with −1000 V voltage in order to have an equivalent electric field inside the sensor.

For both assemblies, in order to provide an illumination with a wide distribution and properly assess the complete detector system, the LED power supply is modulated with a Gaussian noise with increasing standard deviation. The LED distributions shown in Figure 4.13 are centred around two flux points: around 17 equivalent 30 keV photon per 2 µs subframe (Figures 4.13a, 4.13c), and around 140 such photons per subframe (Figures 4.13b, 4.13d).




**(a)** CdTe assembly: low LED intensity

**(b)** CdTe assembly: high LED intensity

**(c)** CdZnTe assembly: low LED intensity

**(d)** CdZnTe assembly: high LED intensity

**Figure 4.13.** Distributions of counts per subframe in calibrated front-end of CdTe and CdZnTe assemblies under LED illumination modulated with Gaussian noise.

For both mean LED intensities probed and both CdTe and CdZnTe assemblies, the XIDer output distributions are shown to get wider as the standard deviation of

the input modulating noise is increased. The output mean is conserved for all four distribution sets, only the output standard deviation varies significantly.

Using a Gaussian-modulated LED is an intermediate step taking into account the sensor, which can be easily and routinely performed, contrary to using an X-ray source. However, a limitation of this calibration assessment procedure is the imperfect Gaussian modulation, caused by the non-idealities of the modulation circuit and the LED, and by the non-linearity of the LED light output versus its bias voltage (see Figure 3.17a) resulting in an asymmetric output distribution. In addition, the sensor dynamics at place when illuminating the sensor also explains that qualitatively, the shape of these distributions is not as optimal as those obtained under external injection.

## 4.5 Calibration assessment with X-rays at a beamline

The final calibration assessment step is to use the ESRF beam itself, which is a light source that follows Poisson statistics. In the BM05 beamline, the synchrotron X-rays are used to assess the behaviour of the front-end under Poisson illumination. Because of the scarcity of beamtimes, the dataset presented in this section was elaborated prior to the datasets of the previous section. For these results was used the CdTe assembly PAT25, that was calibrated with a slightly less refined procedure than presented previously. CdZnTe assemblies were not available at that time.

Assembly PAT25 was calibrated for an expected photon energy of 30 keV. In accordance, to assess this set of calibration, the beamline monochromator is used to fix the source photon energy at approximately 30 keV. The 1-mm thick Ohmic CdTe sensor of PAT25 had an applied bias of −500 V, and after an initial stabilisation period of 20 min, the sensor was irradiated with X-rays. The flux was chosen to count several tens of photons per pixel per 2 µs subframe. The assembly was programmed with the calibration parameters of a chosen front-end for 30 keV. A frame of 100000 consecutive 2 µs subframes was recorded: Figure 4.14a shows the distribution of counts per subframe for the calibrated front-end, spreading from approximately 35 to 80 photons per subframe. The distribution retrieved here is close to a Poisson distribution, but some imperfections are apparent. Notably troughs at the vertical lines of 44, 52, 60 and 68 counts per subframe are observed. From this periodicity of 8 in the troughs, it can be inferred as a miscalibration in the coarse or fine stage charge pump packet size.

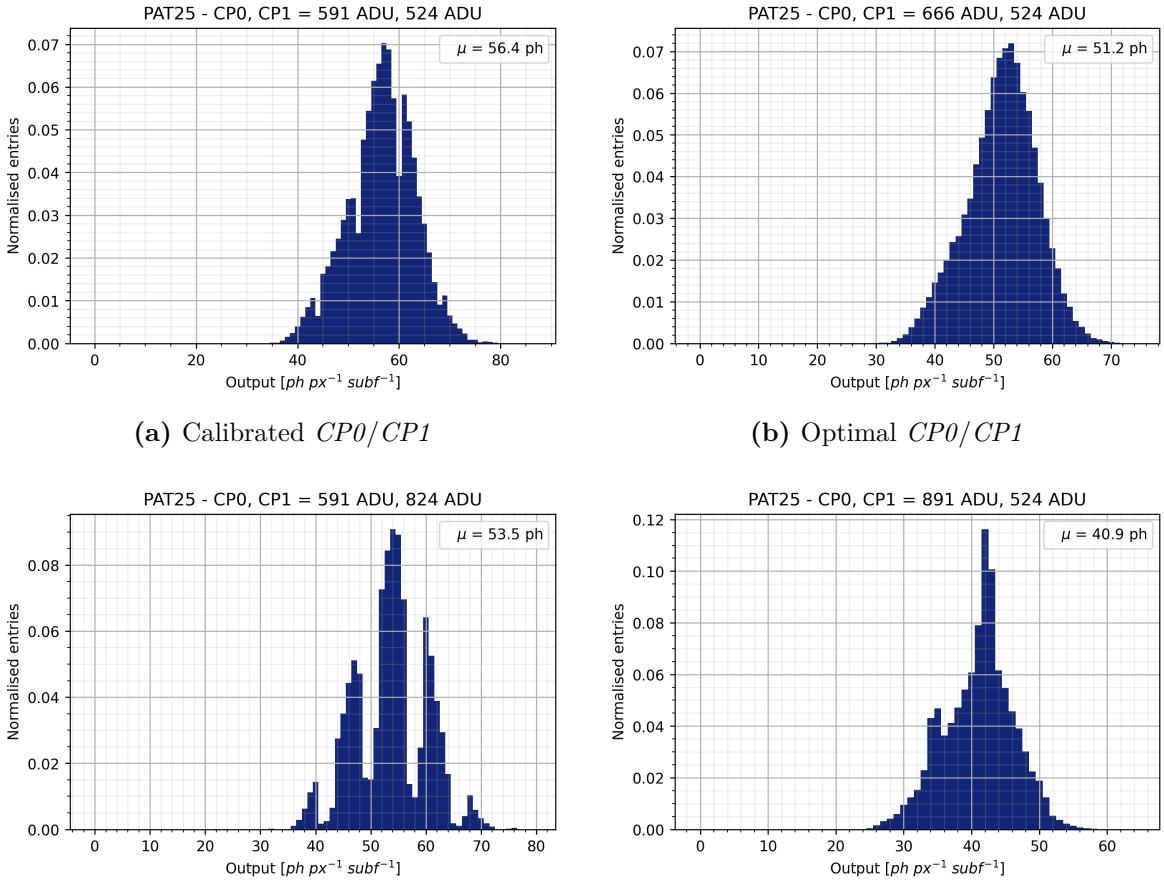
Furthermore, the charge pump packet sizes from both stages are swept in increments of 75 ADU around the calibrated values for this specific front-end: *CP0* = 591 ADU and *CP1* = 524 ADU. Some example of histograms are shown in Figures 4.14b, 4.14c, 4.14d. Qualitatively, one optimal histogram has a shape closer to the expected than the calibration reference, shown by Figure 4.14b. There are no obvious defects in the shape of this distribution, and it is likely that the DAC parameters used here are closer to the ideal calibration parameters. The calibrated DAC:*CP0* is approximately 11 % lower than the optimal DAC:*CP0* found with this sweep, whereas the values of DAC:*CP1* are the same. This lies within the uncertainty range of the calibration procedure previously described. The overall shape of the distribution is slightly different to what was simulated in Subsection 2.1.6 and also what was measured with external injection or with modulated LED illumination. This is explained by the 4-bunch mode time structure of the synchrotron beam that was in place for this measurement (see Figure 1.3). At the time, the subframes were not synchronised with the synchrotron bunches: during a single subframe is integrated the charge coming from either two or three consecutive bunches, depending on the timing. The integration of three bunches per subframe being the most likely, a small bump, linked to the less likely integration of only two bunches, is observed on the left-hand side of the distribution.

Figures 4.14c and 4.14d show two cases where the charge pump packet sizes are quite far from the calibration. In Figure 4.14c, *CP1* was programmed too high, and there appears large hole defects with 8-count periodicity in the histogram shape. On the contrary, Figure 4.14d shows that when *CP0* is much larger than calibration, spike defects can appear, still with 8-count periodicity.

## 4.6 Conclusion

Calibration of the XIDer digital integration readout electronics requires the calibration of the threshold and the charge pump packet size for both coarse and fine stages. During this work, calibration procedures based on the internal charge injection circuit were conceived, implemented, and tested.

Calibration assessments with charge injection, LED illumination, and monochromatic X-ray illumination have proven that the presented procedures are successful within the specified tolerance, which is linked to the uncertainty on the values of electronic components in the front-ends. To gain further precision, this first-level calibration procedure based on internal charge injection must be completed with a secondary calibration strategy using an external source of precisely-known energy,




**(a)** Calibrated *CP0/CP1*

**(b)** Optimal *CP0/CP1*

**(c)** Calibrated CP0, too large CP1

**(d)** Too large CP0, calibrated CP1

**Figure 4.14.** Distributions of counts per 2 µs subframe for a picked out calibrated channel of assembly PAT25 under 30 keV illumination, for different *CP0/CP1* configurations. The calibrated *COMP0* and *COMP1* are used. Each distribution is derived from a total frame of 100000 consecutive subframes.

which is out of scope of this work.

# Chapter 5

# Assembly characterisation

The XIDer detector is designed to work with X-ray photon energies between 30 keV and 100 keV, requiring the use of high-Z sensors. Several cadmium telluride assemblies, with 100 µm or 200 µm pixel pitch, have been produced and calibrated as detailed in the previous chapter. These XIDer prototype assemblies implement the digital integration readout using the T4 chip and are characterised and evaluated in this chapter with reference to the target requirements of noise-free operation, high-dynamic range, single-photon resolution and fast time-resolved detection. The target detector specifications are reminded in Table 5.1.

**Table 5.1.** Target detector specifications

| **Main features** | **Target** |
|---|---|
| **Sensor** | |
| Sensor material | Cd(Zn)Te, GaAs |
| Energy range | 30–100 keV |
| Pixel size | 100–200 µm |
| Noise | single-photon sensitivity |
| **Pulsed mode operation** | *16-bunch mode* |
| Maximum photon flux | $\sim$ 250 ph/pulse/pixel |
| Cycle dead time | $\leq$ 170 ns |
| Internal frame rate | $\geq$ 5.68 MHz |
| **Continuous mode operation** | *7/8+1 mode* |
| Maximum photon flux | $\sim$ 1500 Mcps/pixel |
| Cycle dead time | $\leq$ 170 ns |

Although numerous prototype XIDer hybrids have been produced (see Appendix 7.1), this chapter focuses on only a handful of prototypes, selected for their most

uniform response to illumination. These include three Ohmic CdTe assemblies: PAT18 with a 100 µm pixel pitch, PAT21 and PAT25 with 200 µm pixel pitch. The 1-mm thick CdTe sensors are biased with a −500 V high voltage. In some sections, a CdTe assembly is also compared to the high-flux CdZnTe (HF-CZT) assembly PAT39, which was produced at a later time. PAT39 has a 200 µm pixel pitch and its thicker 2-mm CdZnTe sensor is biased with a −1000 V high voltage, in order to have a similar internal electric field.

## 5.1 Noise considerations

The XIDer detector should be sensitive to single photons with energy higher or equal to 30 keV. This requires a low equivalent noise charge, with the target of 350 $e^-$ rms, and a low dark signal to distinguish the single-photon input signal to the background image. This section goes over measurements of equivalent noise charge and dark flux in XIDer prototype assemblies.

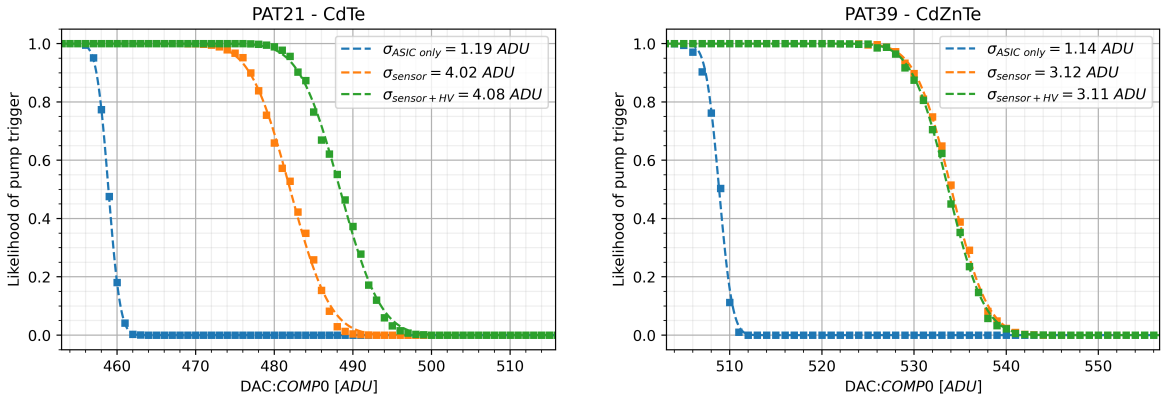
### 5.1.1 Equivalent noise charge

The equivalent noise charge (ENC) is a measure of electronic noise, used to characterise the front-ends of XIDer assemblies. The ENC of a front-end can be measured at the comparator threshold level in the coarse stage, with a DAC:*COMP0* sweep, as described in Subsection 3.4 and as performed for the threshold calibration. The standard deviation parameter retrieved from the error function fit of the threshold sweep yields the ENC in units of $\mathrm{ADU}_{COMP0}$. With the assumptions (detailed in Subsection 4.1.1) of the feedback capacitor value $C_f = 50\,\mathrm{fF}$ and $1\,\mathrm{ADU}_{COMP0} = 1\,\mathrm{mV}$, $1\,\mathrm{ADU}_{COMP0}$ is equivalent to $C_f/e \cdot 1\,\mathrm{mV} = 312.5\,e^-$. The value of this ENC is linked to the noise level of the front-end charge sensitive amplifier, as well as the capacitance at the input of the amplifier, and the shot noise of the sensor leakage current [117].

To characterise the noise level of a XIDer assembly, it is worth to disentangle potential noise contributions by looking at the three following scenarios:

1. ASIC front-end by itself, with the sensor disconnected,
2. ASIC front-end with the sensor connected but not biased,
3. ASIC front-end with the sensor connected and biased.

For CdTe assembly PAT21 and CdZnTe assembly PAT39, Figure 5.1 shows the coarse stage threshold sweeps and their error function fit for these three scenarios.




**(a)** ENCs of CdTe assembly

**(b)** ENCs of CdZnTe assembly

**Figure 5.1.** Coarse stage threshold sweeps and retrieved ENCs of CdTe and CdZnTe assemblies under three scenarios. Blue: sensor disconnected. Orange: sensor connected but not biased. Green: sensor connected and biased with high voltage.

The six threshold sweeps depicted by Figures 5.1a and 5.1b all closely match their error function fit, which means that for all three scenarios probed, the electronic noise in the front-end remains close to a Gaussian noise with standard deviation $\sigma$.

In the scenario 1 (ASIC only), both assemblies have a measured ENC of approximately 1.2 ADU rms, which translates to 370 $e^-$ rms or 1.7 keV rms in Cd(Zn)Te material ($\epsilon_{CdTe} = 4.43$ eV and $\epsilon_{CdZnTe} = 4.64$ eV [95]). In comparison, in the scenarios 2 and 3, when the sensor is connected to the front-end, the measured ENC is 2 to 4 times higher, depending on the front-end. This sharp increase to approximately 1 k$e^-$ rms or 5 keV rms, can be explained by the capacitance of the multiple input pads of the T4 chip, as well as the long wires connecting the input pads to the front-ends. In scenarios 2 and 3, a parasitic capacitance on the order of 1 pF is added at the input of the front-end preamplifier, which significantly increases the capacitive load and thus the noise level. In the next iterations of the chip, the design was optimised to reduce the parasitic capacitance to approximately 150 fF. Still, the equivalent noise of 5 keV rms obtained with the T4 assemblies is low enough to have single photon resolution for energies of 30 keV and higher.

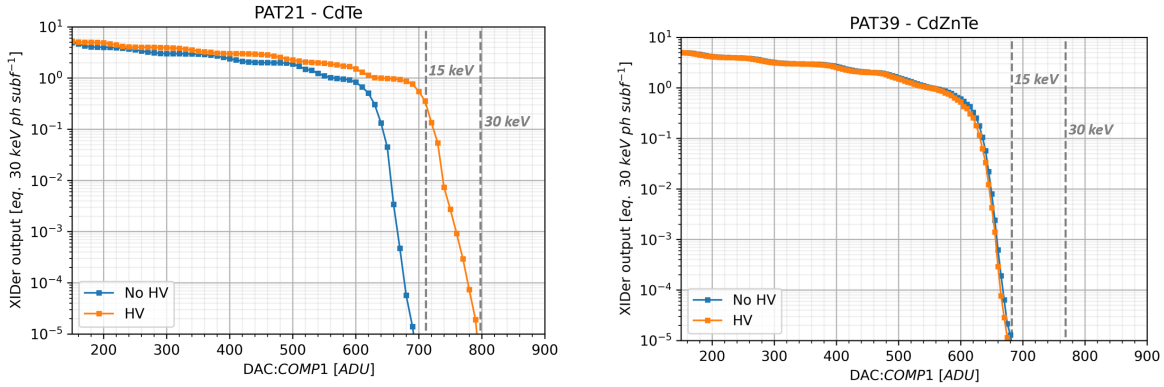
As shown in Figure 5.1, when connecting the sensor, there is also an apparent baseline shift of approximately 25 ADU $\approx$ 25 mV. This is due to the use of the dynamic switch connecting the sensor to the front-ends. In this chip iteration, flipping on or off any dynamic switch provides a non-negligible charge injection, translating the baseline by an amount that depends on the capacitive load. To take into account these injections, it is thus important to calibrate the front-ends with the exact set of dynamic switch sequences.

Biasing the sensor with high voltage appears to have no influence on the ENC measured in the front-ends. However, the baseline can be changed as sensor leakage is integrated. For this measurement, the comparator is set to be active for a short duration in the middle of the subframe (see Figure 3.7a), here after an integration period of approximately 350 ns. Figure 5.1 shows that CdTe sensor leakage integration during 350 ns provides a shift of 6 ADU $\approx$ 6 mV, which translates to a leakage current of 0.9 nA in the given pixel, or a 20 nA mm$^{-2}$ current density. In comparison, CdZnTe sensor leakage is negligible, with a recorded shift below 0.5 ADU, corresponding to a current density lower than 70 pA px$^{-1}$ or 2 nA mm$^{-2}$.

### 5.1.2 Dark flux

As mentioned in Subsection 2.2.2, single-photon sensitivity at a given energy is only meaningfully achieved if it is statistically unlikely for the dark signal to be over threshold. In that regard, the chosen figure of merit is the dark flux, defined as the recorded output flux of a pixel in dark conditions at a given threshold.

For one selected front-end of CdTe assembly PAT21 and CdZnTe assembly PAT39, the threshold of the fine stage is swept. For each threshold value, the average output value is recorded over 1.4 million 2 µs subframes. The threshold sweep is performed twice, with and without the high-voltage bias of the sensor, and the resulting dark fluxes are depicted in Figure 5.2. For these data, the non-biased assemblies were calibrated for an energy of 30 keV and the default sequencer tracks were used.




**(a)** Dark flux of CdTe assembly

**(b)** Dark flux of CdZnTe assembly

**Figure 5.2.** Fine stage threshold sweeps and retrieved average dark fluxes of CdTe and CdZnTe assemblies. Sweeps are performed first without high-voltage sensor bias (blue line), then with high-voltage bias (orange line). Dashed grey lines indicate baselines after the injection of an equivalent 15 keV (0.5 ph) and 30 keV (1 ph).

The comparator sweeps show a well-defined trend that can be divided in two parts

with their respective slope. The transition point corresponds to a dark flux value of approximately 1 equivalent 30 keV photon per subframe. Above 1 photon of dark flux, the threshold is lower than the fine stage baseline, which triggers the charge pump in every subframe. The chip is here in an unsuited working zone. Lowering the threshold further below this value increases the dark flux in steps of 1 photon, the digitisation step. On the contrary, when the threshold is increased above this value, signal discrimination starts playing a role and the dark flux drops with a steep slope, as noise fluctuating above threshold becomes less and less likely.

In the examples shown with no high voltage, a threshold set at 15 keV, *i.e.* the half 30 keV photon level, is high enough to have dark flux values below $10^{-5}$ equivalent 30 keV photon per subframe. This corresponds to approximately 5 false counts per second.

The dark flux depends on the electronic noise, but is also worsened by the presence of uncompensated leakage current as the sensor is biased. For the CdZnTe assembly, biasing the sensor has no impact on the dark flux as the leakage current integrated during the 2 µs subframe is insignificant. For the CdTe assembly front-end however, the threshold sweep is translated by approximately 80 ADU when the sensor is biased. This translation varies depending on the chosen front-end leakage current.

Because of the high leakage current of a biased CdTe sensor, the dark flux value is approximately 0.4 photon per subframe (or 200 k false counts per second) with a half 30 keV photon threshold. This highlights the need of a leakage current compensation system, particularly in detectors based on CdTe. To have better sensitivity at 30 keV with these prototypes, it is preferred to increase the fine stage threshold from 0.5 ph to 0.8–1 ph.

## 5.2 Characterisation of transfer phase

The digital integration readout as implemented in the ASIC T4 chip is a pipelined two-stage front-end, intended to function synchronously with the synchrotron bunch modes, detailed in Figure 1.3). Ideally, there would be no charge arriving to the front-ends during the transfer and reset phases. However, this is not always the case in experiments, for instance under high-flux illumination if many photons arrive right before the transfer initiates, or simply when synchronisation is not possible. To understand the behaviour of the pipeline and particularly of its transfer phase between stages, the following measurement is performed: using the internal injection circuit, a fixed amount of charge is injected in the front-end input at different moments in the subframe sequence. The sequencer tracks used are shown in Figure 5.3 and follow

a similar structure as those detailed previously in Subsection 3.1.4, with a 1.6 µs subframe duration and a conservative reset and transfer periods. The charge injection is provided at the falling edge of track InjB1. This falling edge is swept in time across the subframe, in steps of 5 clock cycles with a frequency $f_{clk} = 389\,\text{MHz}$ or approximately 13 ns.

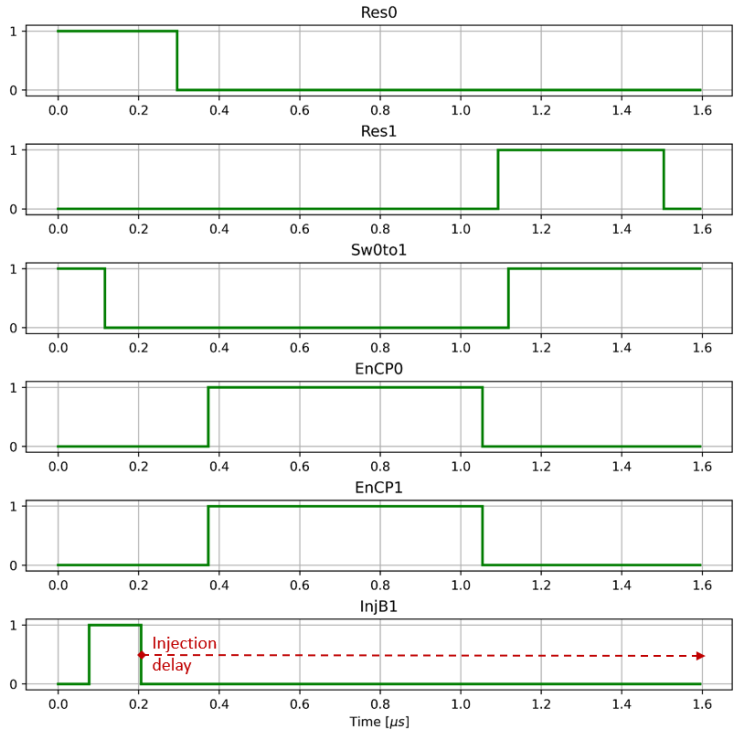



**Figure 5.3.** Sequencer tracks of the two-stage pipeline with charge injection.

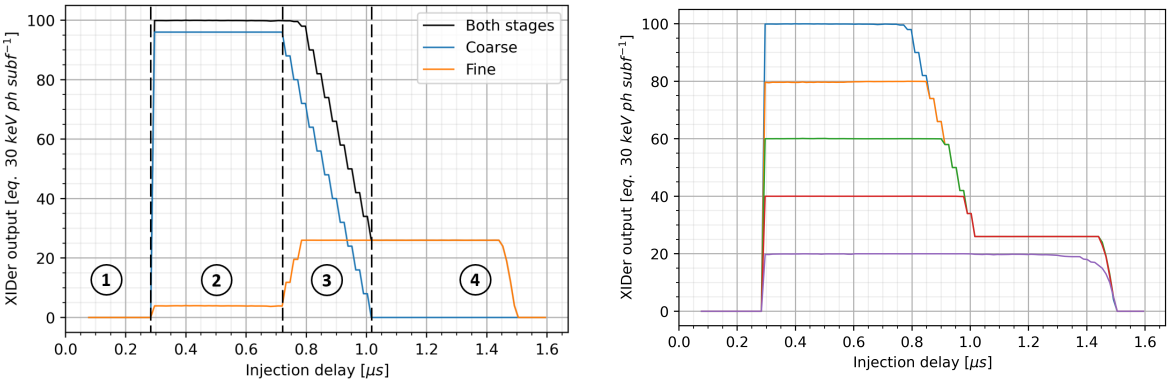
Figure 5.4a shows such an injection delay scan using a charge injection equivalent to 100 ph in a calibrated front-end. 100 ph is a lot of charge to inject at once but is on the order of magnitude of the charge that can arrive on one front-end following a strong X-ray bunch in very high flux conditions.

The delay scan can be divided in four sections, as depicted in Figure 5.4a:

- Section 1. The injection is provided while Res0 is still active, meaning the coarse stage is being reset. The injection is fully lost.
- Section 2. The injection is provided shortly after the coarse stage reset. The coarse stage has sufficient time to pump out all 12 packets of 8 ph out of the 100 ph injected charge. The fine stage pumps out the remaining 4 ph.
- Section 3. The frequency of the charge pump chosen here is $f_{CP} = f_{clk}/10$. Consequently, it takes 120 clock cycles or 310 ns to pump 12 times. During this section, consisting of the last 310 ns during which the charge pump (EnCP0

track) is enabled, the injection arrives too late for the coarse stage to pump 12 times. The coarse stage left-over gets progressively bigger as the charge is injected later, which is compensated by the fine stage until it saturates. Once the fine stage saturates, the total counts start dropping and part of the injection is discarded.

- Section 4. The injection is provided after the period of activation of the coarse stage charge pump. The whole 100 ph is transferred to the fine stage, which only has time to pump out and count 26 ph. When injecting at the subframe very end, there is no time for the injected 100 ph to be transferred before the resets and the total counts falls to zero.




**(a)** Coarse / fine stages with 100 ph injection

**(b)** Total output with 20, 40, 60, 80, and 100 ph injection

**Figure 5.4.** Injection delay scans, where fixed amounts of charge are injected in a calibrated front-end after a delay that is swept.

Section 3 lasts for the duration it takes the coarse stage to pump out all possible coarse charge packets from the integrated charge. Consequently, this duration depends on the amount of charge injected, as depicted by Figure 5.4b, which shows total counts for different levels of injection. For the same reason, the duration of section 3 also depends on the charge pump frequency.

A charge injected too late in the subframe is directly transferred to the fine stage, which can easily saturate if this charge is too big for the fine stage to handle during the following subframe. Saturation is a real issue for the system as it makes data differ from statistics, and create artefacts in counts distributions.

To mitigate this problem, two solutions can be employed. The first solution is the synchronisation of the subframes with the source time structure. Indeed, the ESRF filling patterns have built-in gaps in them during which no photons are emitted. When synchronising the subframe duration with the synchrotron clock, the phase of the

subframes can be tuned to have no X-rays arriving during this direct transfer period. Similarly, for visible light, LED illumination can be modulated in pulses synchronised with the integration pattern. When this first solution is not possible or not sufficient, a second option is to use the dynamically-controllable switch $S_3$ connecting the sensor to the front-ends (see Figure 3.1). This switch is programmed to have the sensor connected to the electronics only from the coarse stage reset Res0 until close to the end of the charge pump activation period EnCP0. Charge stored on the sensor side during the time of sensor disconnection is discarded during the coarse stage reset. This increases the dead time, but prevents data corruption from fine stage saturation.

## 5.3 High dynamic range and linearity

Dynamic range is a crucial aspect of the XIDer detector. The dynamic range of XIDer prototypes is first assessed with the charge injection circuit, and then with beamline monochromatic X-rays.

### 5.3.1 Maximum dynamic range under charge injection

Probing the dynamic range using the charge injection circuit allows to evaluate the ASIC performance in ideal conditions, with no influence of the sensor dynamics. As seen in Section 4.3, charge can be injected to the ASIC front-ends either internally or externally through an SMA connector. External injection is preferred here, since internal injection in this ASIC iteration is not able to provide sufficient charge levels to probe the maximum dynamic range.

Shortly after the coarse stage reset Res0, a waveform generator provides external injection to a calibrated front-end. Figure 5.5 shows the XIDer front-end output when sweeping the provided voltage from 0 V to 1.9 V. The XIDer output is converted to units of equivalent $\mathrm{ph\,s^{-1}}$, where the considered active subframe duration is 750 ns (the charge pump is activated for 750 ns following the injection). Figure 5.5 shows two such sweeps, for the charge pump frequencies of 39 MHz and 78 MHz. For both sweeps, the XIDer response is linear with $R^2 \geq 0.999$ until saturation, which occurs at approximately $0.35 \times 10^9\,\mathrm{ph\,s^{-1}}$ and $0.68 \times 10^9\,\mathrm{ph\,s^{-1}}$ for the two sweeps. These values depend on the charge pump frequency $f_{CP}$: the coarse stage is able to remove 8 ph and the fine stage 1 ph with every tick of the charge pump. With $f_{CP} = 39\,\mathrm{MHz}$, the maximum dynamic range is directly given by $9\,\mathrm{ph} \times f_{CP} = 0.351 \times 10^9\,\mathrm{ph\,s^{-1}}$. The same calculation gives a maximum dynamic range of $0.702 \times 10^9\,\mathrm{ph\,s^{-1}}$ with the doubled charge pump frequency 78 MHz, however, the observed value is slightly lower.

This is explained by the saturation of the transfer stage, which is only able to transfer 40 to 50 ph because of the 1.2 V internal maximum voltage, whereas the charge pump could trigger up to 59 times in the allowed 750 ns.

The objective for XIDer is to reach $10^9$ ph $s^{-1}$ $px^{-1}$. With the current prototypes where the coarse stage is intended to remove 8 ph charge packets, the charge pump frequency must be increased to approximately 112 MHz to fulfil the objective. The designed charge removal circuit was simulated to handle driving frequencies as high as 200 MHz [99], but other limitations in the electronics prevent from using such frequencies in the T4 ASIC version.

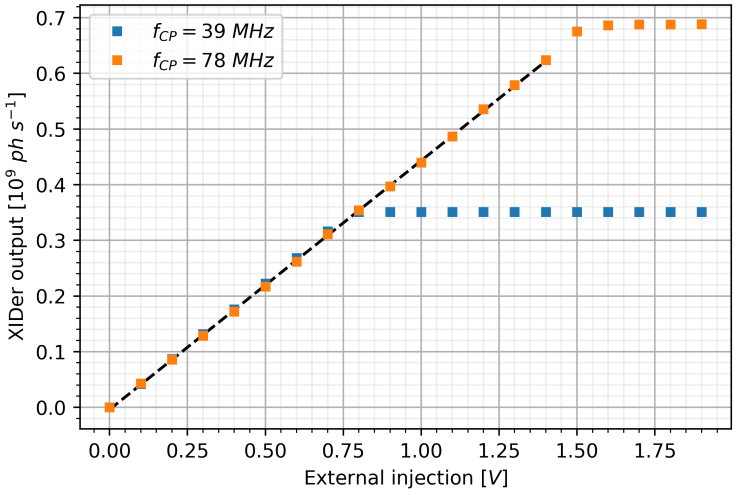


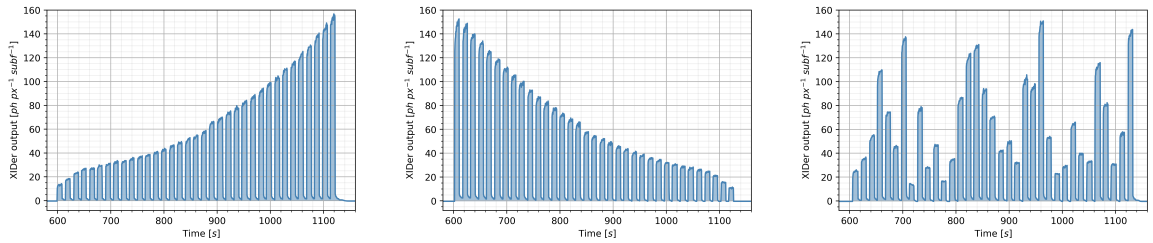

**Figure 5.5.** Digital output of calibrated front-end for different values of injection, recorded as an average over many subframes, where the charge pump is active for 750 ns after injection. The output and linear fit are shown for 39 MHz and 78 MHz charge pump frequencies.

### 5.3.2 Linearity under 30 keV X-ray irradiation

This subsection presents the linearity of XIDer prototype PAT18, a 1 mm thick Ohmic CdTe assembly with 100 µm pixel pitch, under monochromatic 30 keV X-ray irradiation, in the quasi-uniform 7/8+1 ESRF filling mode (see Figure 1.3). As detailed in Subsection 3.6.2, a set of aluminium filters, put in the beam path by a remotely-controlled mechanical system, is used to adjust the flux incident on the assembly. The beam is slitted down to approximately 1 $mm^2$ and is centred on the 16-pixel matrix. The results shown here focus on one central pixel, which was calibrated for the energy of 30 keV. A subframe duration of 2 µs with 1.65 µs active integration window is used, unsynchronised to the beam time structure. The XIDer output flux in units of photons per pixel per subframe is compared to the current of a silicon photodiode, placed

in front of the XIDer assembly, converted to similar units (see conversion formula in Subsection 3.6.2).

The beam flux is adapted by using 35 different configurations of Al filters attenuating the beam between approximately 4 and 100 ph px$^{-1}$ subf$^{-1}$, which translates to between $2 \times 10^8$ and $6 \times 10^9$ ph mm$^{-2}$ s$^{-1}$. Each flux is measured for 6 s, with a gap of a couple of seconds between each flux with the beam shutter closed, to change filter configurations. During this measurement procedure, PAT18 is programmed to acquire and average a burst of 9000 subframes every 0.5 s. As shown by Figure 5.6, the measurement is repeated three times: (a) with increasing fluxes, (b) with decreasing fluxes, (c) with shuffled fluxes. Each iteration is preceded by a reset of the sensor high-voltage bias and a stabilisation period of 10 minutes.




**(a)** Increasing fluxes **(b)** Decreasing fluxes **(c)** Shuffled fluxes

**Figure 5.6.** Three iterations of probing the linearity of a calibrated PAT18 front-end, under 30 keV X-ray irradiation. The 35 fluxes are each measured for 6 s. Data points are taken every 0.5 s and are the average of 9000 subframes.

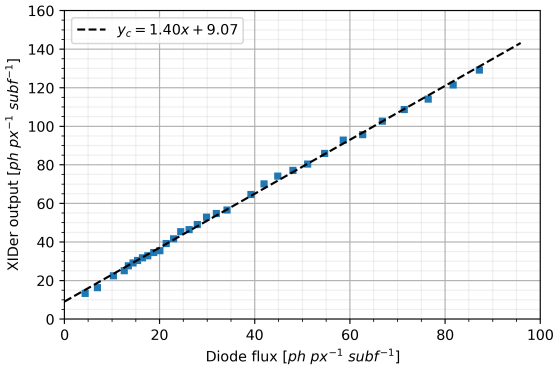
For each of the 35 flux points, the XIDer output mean value is calculated (over the second half of the 6 s measurement period to minimise instabilities) and compared to the reference diode flux, to produce a linearity plot. The datasets are corrected for beam decay and refills. Figure 5.7a shows the retrieved data points and the resulting linear fit from the shuffled fluxes measurement (Figure 5.6c). A couple of points that correspond to the diode fluxes above 90 ph px$^{-1}$ subf$^{-1}$ are not shown in Figure 5.7a, as the fine stage was slightly saturated and the data points consequently sub-linear. This early fine stage saturation is due to charge arriving late in the subframe structure and being transferred directly to the fine stage, as explained in Section 5.2.

All three measurements data have good agreement with their respective linear fit, which have $R^2 \geq 0.998$. As shown by Figure 5.7b, all three fits yield a slope of $1.43 \pm 0.03$ and an intercept of approximately 9 ph px$^{-1}$ subf$^{-1}$ for increasing and shuffled fluxes, and closer to 7 ph px$^{-1}$ subf$^{-1}$ for decreasing fluxes. This intercept value can vary between pixels and assemblies, depending on the leakage current observed for a given pixel. A part of this positive intercept comes from the third-harmonic generation

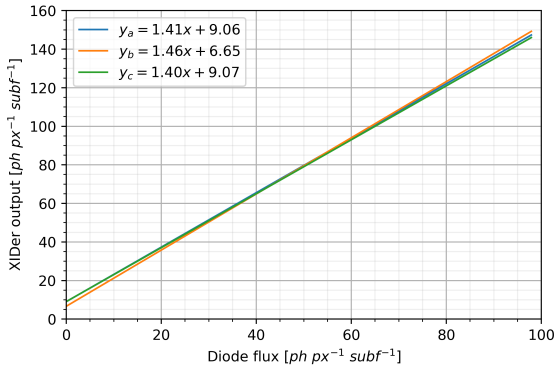
in the beamline: 90 keV photons are negligibly absorbed by the 500 µm thick silicon photodiode but absorbed at 65% by the 1 mm CdTe sensor. This creates a discrepancy not included in the diode current to reference flux conversion formula.

What is more, while measurements (a) and (c) provide very closely-matching results, measurement (b) seems to slightly deviate. This is thought to be explained by the complex CdTe sensor dynamics as the slowly-decreasing flux-induced sensor leakage, which can be seen in between the flux steps of Figure 5.6, depends on the dose of irradiation. However, the slope, which one would expect to be close to 1, is consistently measured at values of 1.4–1.5. Similar measurements performed with other front-ends, as well as a longer two-minute irradiation period, have provided similar results. It can be noted that third-harmonic generation cannot alone explain this increased slope, as the Al filters transmit almost all 90 keV photon energy.

Each point of the linearity datasets presented here comes from averaging over thousands of subframes. To understand the origin of this slope, it is worth investigating the count distributions of XIDer acquisitions.




**(a)** Data points retrieved from Figure 5.6c and linear fit




**(b)** Linear fits from Figures 5.6a, 5.6b, 5.6c

**Figure 5.7.** Linearity plots derived from measurements presented in Figure 5.6. Linear fits against the reference diode flux reveal a consistent slope of $1.43 \pm 0.03$ and an intercept of 6–9 ph px$^{-1}$ subf$^{-1}$, with $R^2 \geq 0.998$.

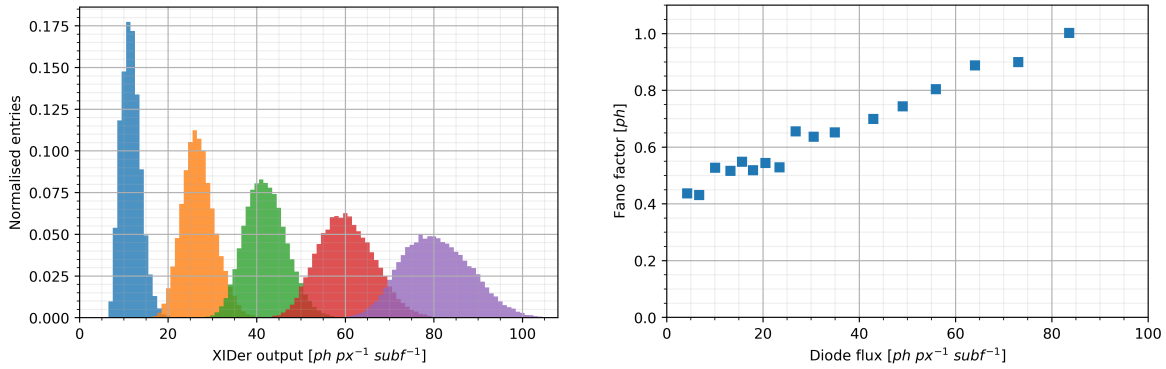
### 5.3.3 X-ray counting statistics

A similar procedure is conducted here, using the same Ohmic CdTe PAT18 prototype assembly with 100 µm pitch, and 30 keV X-ray irradiation in 7/8+1 filling mode. The beam flux is adapted by using 17 different configurations of Al filters attenuating the beam between approximately 4 and 85 ph px$^{-1}$ subf$^{-1}$, as converted from the measures of a reference silicon diode. For each flux, PAT18 is programmed to record and save

in full 50000 subframes.

Figure 5.8a shows the counts distribution of the 50000-subframe sets from five example fluxes. Qualitatively, these distributions take the shape of the Poisson X-ray source distribution, with no apparent defects in the histogram structure, sign of good calibration.

Quantitatively, such datasets with mean $\mu$ and standard deviation $\sigma$ can be characterised by their Fano factor $F = \sigma^2/\mu$. It was seen in Subsection 2.1.6 and more specifically Figure 2.9b that the Fano factor is simulated in such conditions to stay relatively constant at values of 0.66–0.68 ph over the flux range in consideration. However, the experimental data presented in Figure 5.8b show that the derived Fano factor increases from approximately 0.4 ph at a reference diode flux of 4 ph $\mathrm{px}^{-1}$ $\mathrm{subf}^{-1}$ to 1.0 ph at 84 ph $\mathrm{px}^{-1}$ $\mathrm{subf}^{-1}$.




**(a)** Five example counts distributions

**(b)** Fano factor vs. diode flux

**Figure 5.8.** Probing the statistics of a calibrated PAT18 front-end, under 30 keV X-ray irradiation. For each of the 17 fluxes probed, a 50000-subframe dataset is acquired, its Fano factor is calculated and compared to a reference diode flux. Contrary to simulations, the Fano factor is observed to increase with flux.

## 5.4 Time-resolved capabilities

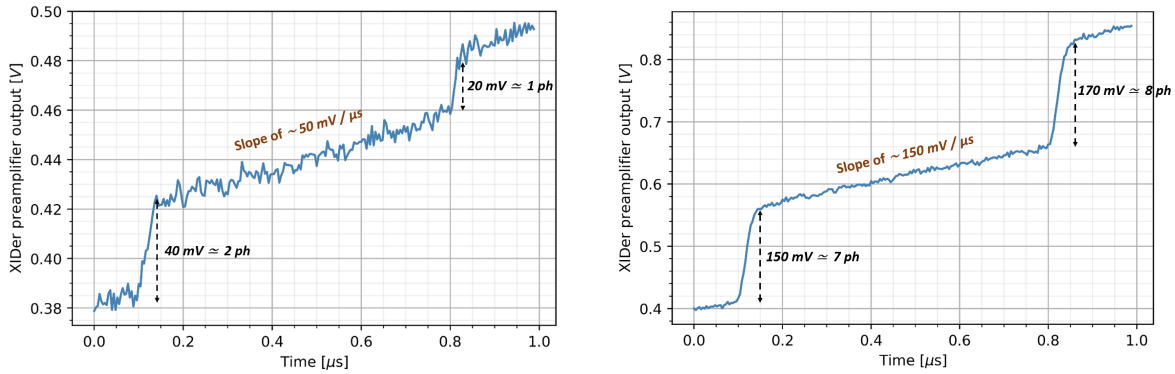
In the previous section, the Fano factor $F = \sigma^2/\mu$ was observed to increase with incident photon flux. A conceivable explanation is that the Fano factor is modulated by the presence of flux-induced sensor leakage, providing a significant extra contribution to the measured average flux $\mu$. To substantiate this, the following subsections move away from continuous illumination to explore pulsed irradiation, with the 4-bunch ESRF filling mode as well as the fast pulsed LED setup, in order to manage to separate signal contributions from the light pulse itself and from flux-induced sensor leakage.

### 5.4.1 Charge collection in a front-end

To investigate the charge collection dynamics in a pixel front-end, the 4-bunch ESRF filling mode is utilised, in which photons are emitted in bunches separated by 704 ns (see Figure 1.3). The collection of photo-generated charge arriving at the bottom electrode can be measured directly at the front-end preamplifier output buffer. For this purpose, the investigated front-end is used as a simple charge-sensitive amplifier, in which the charge pump and the transfer stage are disabled. Figure 5.9 shows two waveform examples of the front-end preamplifier output voltage from PAT18 (Ohmic CdTe prototype assembly with 100 µm pixel pitch) as recorded by an oscilloscope. In these two examples, the monochromatic 30 keV beam flux was adapted with aluminium filters to have fluxes of only a few photons per bunch per pixel, in order not to reach the front-end 1.2 V maximum value.

In CdTe, assuming a pair-creation energy of $\epsilon_{CdTe} = 4.43\,\text{eV/pair}$ [95], the integration in the 50 fF feedback capacitor of the charge generated by one 30 keV photon results in a 21.7 mV electric potential difference. This value is modulated by the charge collection efficiency, and, at the pixel level, by spatial charge sharing. In Figure 5.9a at $t_1 = 0.1\,\mu\text{s}$ and $t_2 = 0.8\,\mu\text{s}$, voltage steps corresponding to the fast integration of 2 photons and 1 photon of charge are clearly observed. Similarly, Figure 5.9b shows voltage steps corresponding to 7 and 8 photons. These two steps are consecutive bunches separated by 704 ns and are easily distinguished by the front-end. Averaging over thousands of such waveforms, the mean rise-time for a single bunch integration is measured to be 36 µs, which is fast enough to also distinguish bunches in the faster 16-bunch filling mode.

Between each bunch, a significant leakage current is integrated in the front-end, resulting in slopes of 50 mV/µs and 150 mV/µs for Figures 5.9a and 5.9b respectively. These translate to leakage currents of 2.5 nA and 7.5 nA for the given pixel, or current densities of $250\,\text{nA mm}^{-2}$ and $750\,\text{nA mm}^{-2}$. Strikingly, over the 1 µs of waveform shown in these figures, more charge is integrated between the bunches than during the bunches themselves. This leakage current appears to be a constant value, as the signal integration is linear in time. The higher the incident flux is, the steeper the slope is, *i.e.* the higher the leakage is. To remove contributions arising from this flux-dependent leakage, a fast dynamic leakage compensation system will then be required.




**(a)** Flux 1 **(b)** Flux 2 (higher than flux 1)

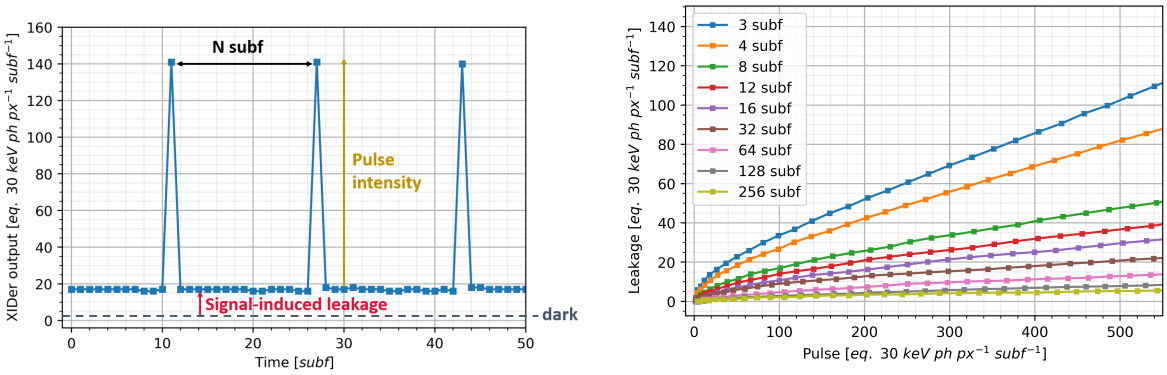
**Figure 5.9.** Oscilloscope waveforms of PAT18 (Ohmic CdTe prototype assembly with 100 µm pixel pitch) front-end preamplifier output buffer, for which the charge pumps and the charge transfer are disabled, under 30 keV 4-bunch irradiation. Individual bunches are integrated at $t_1 = 0.1$ µs and $t_2 = 0.8$ µs, and a constant leakage is integrated in-between.

### 5.4.2 Quantifying flux-induced leakage with a pulsed LED

As seen in the previous subsection, in bunch-mode illumination, a significant part of the total collected charge is due to inter-bunch leakage originating from the CdTe sensor. To quantify the contribution of this flux-induced leakage, the programmable LED in-lab setup presented in Subsection 3.6.1 is used. The Ohmic CdTe PAT21 prototype assembly with 200 µm pitch is repeatedly irradiated with a 1 µs LED square light pulse with a period of N subframes. The LED pulse is provided in synchronisation with the subframe structure so that the entire 1 µs light pulse is reliably integrated entirely during a single 2.8 µs subframe. The LED setup allows the easy control of the LED power output and the pulsing frequency, as well as the use of a relaxed subframe duration.

The goal is to measure and compare in steady state for increasing LED light output the direct pulse intensity with the flux-induced leakage, as depicted by Figure 5.10a. The output signal values are all converted to 30 keV equivalent photons, energy at which the prototype assemblies are calibrated, although they were irradiated with visible light. The value of the flux-induced leakage is calculated as the average of the non-illuminated subframes, from which the dark leakage value is removed. Figure 5.10b shows a plot of the retrieved leakage versus pulse intensities, for several values of periodicity from 3 to 256 subframes.

Flux-induced leakage is seen to increase with light intensity and with pulsing frequency. After interpolation of the data presented in Figure 5.10b, it is worth looking at a slice of this graph. Figure 5.11 shows plots of the retrieved flux-induced



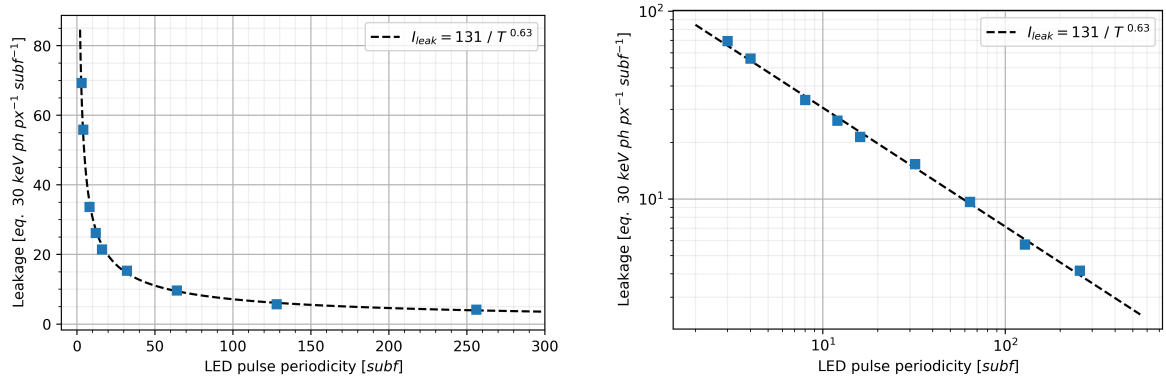

**(a)** Digital output with N = 16 subframes. **(b)** Flux-induced leakage vs pulse intensities

**Figure 5.10.** Synchronised 1 µs pulsed LED irradiations with period N subframes of Ohmic CdTe PAT21 assembly. Graph (b) shows the overlap of flux-induced leakage vs pulse intensities, calculated as shown in Graph (a), for several values of periodicity N.

leakage values when the pulse intensity is 300 ph versus the LED pulse periodicity in number of subframes, in linear and in log scale. For each value of pulse intensity, the dataset of the leakage $I_{leak}$ against the periodicity $T$ can be fitted with the following function:

$$f_{fit} : T \mapsto I_{leak1} \; / \; T^{\alpha} \tag{5.1}$$

In this function, $\alpha$ describes how fast the leakage decreases with pulse period $T$ at a given pulse intensity. On the other hand, $I_{leak1}$ corresponds to the leakage value for $T = 1$ subf, *i.e.* for the extrapolated case in which LED illumination is provided every subframe.




**(a)** Linear scale **(b)** Log scale

**Figure 5.11.** Flux-induced leakage corresponding to a 300 ph pulse intensity values versus the LED pulse periodicity in number of subframes. Leakage values are retrieved from an interpolation of the dataset presented in Figure 5.10b.

This fit is repeated for a range of pulse intensities above 25 ph px$^{-1}$ subf$^{-1}$, for

which the leakage datasets match the chosen function. The value of $\alpha$ is observed to have little variance, staying between 0.62 and 0.67, and is thought to be a constant of the material. A similar study using high-flux CdZnTe assembly PAT39 showed $\alpha_{PAT39} \approx 0.80$, which is significantly above $\alpha_{PAT21} \approx 0.64$.

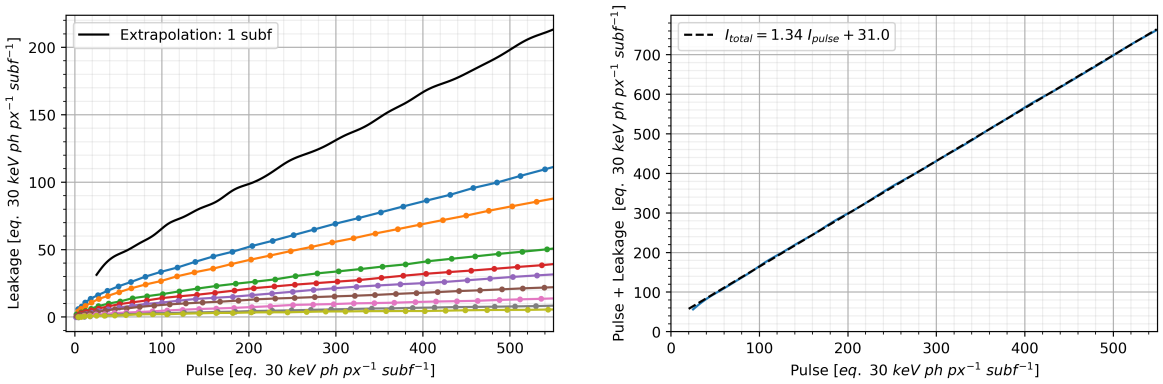
The value of $I_{leak1}$ can be investigated as a function of the input pulse intensity. Then, the extrapolated data for a pulsed LED periodicity of 1 subframe can be overlapped with the real measurements of flux-induced leakage versus pulse intensity, as shown in Figure 5.12a. This gives a prediction of the proportion of flux-induced leakage for the scenario where LED illumination is provided in each subframe. This scenario is what happens when continuously irradiating with X-rays as provided by the ESRF beam patterns, and in this scenario the pulse and flux-induced leakage cannot be easily retrieved experimentally.

This extrapolated data shows that the flux-induced leakage in continuous illumination would be higher than a third of the isolated pulse intensity. Figure 5.12b shows a plot of the total signal, *i.e.* the sum of the isolated pulse intensity and the extrapolated flux-induced leakage, as a function of the pulse intensity. A linear fit of this dataset reveals a slope of 1.34, which approaches the 1.4 slope values achieved experimentally with assembly PAT25, as seen in Subsection 5.3.2. An intercept of $31\,\mathrm{ph\,px^{-1}\,subf^{-1}}$ is extrapolated here, which is roughly 4 times higher than the 6–$9\,\mathrm{ph\,px^{-1}\,subf^{-1}}$ intercepts retrieved for assembly PAT25 that has a twice smaller 100 µm pixel pitch.

The origin of this very large flux-induced leakage current is not yet well understood, but could be due to the material bulk and contact technology in the hybridised sensor. Trapping and detrapping of charge carriers in the material bulk cannot alone explain the slope being increased above 1, whereas an added leakage contribution, arising from the modulation of the junction barrier height, and that is not detected by the reference photodiode, could explain the slope discrepancy observed in Subsection 5.3.2. The photodiode would then give a measurement of the flux corresponding to the isolated X-ray pulses, whereas the illuminated assembly digital output takes into account the significant flux-induced leakage current, justifying the comparison between Figure 5.7 and Figure 5.12b.

## 5.5 Flux-induced leakage transients

So far has only been discussed stationary behaviour under stabilised conditions. Complementarily, this section focuses on sensor leakage transient behaviour, here specifically, the dynamic evolution in time of flux-induced leakage when the irradiation is suddenly stopped. Sensors based on cadmium telluride compounds indeed suffer from




**(a)** Flux-induced leakage $I_{leak1}$ vs pulse intensity

**(b)** Retrieved total signal $I_{total} = I_{pulse} + I_{leak1}$ vs pulse intensity

**Figure 5.12.** Extrapolated data from fits as presented in Figure 5.11 for the scenario in which LED illumination is provided every subframe. Graph (a) shows the extrapolated flux-induced leakage $I_{leak1}$ versus pulse intensity, overlapped with data shown in Figure 5.10b. Graph (b) is a reconstruction of the total signal: pulse + flux-induced leakage $I_{leak1}$, versus pulse intensity. A linear fit reveals a slope of 1.34.

residual aftersignal, or afterglow, where charge keeps being released from the sensor after the irradiation has stopped. The study of residual aftersignal after stopping abruptly X-ray irradiation requires the use of an X-ray shutter. Beamlines at the ESRF dispose of a X-ray beam shutter, but it can take up to a few seconds for such a shutter to completely close. Fast X-ray shutters were not easily available at the time of the X-ray aftersignal studies presented in this manuscript, notably due to their very expensive price point.

This section thus presents first the long time scale X-ray aftersignal for a CdTe assembly, using the slow X-ray beam shutter. Secondly, to probe the fast afterglow components and at the same time the timing capabilities of the XIDer readout, are then presented measurements using the pulsed LED setup, permitting microsecond-fast light switching. These measurements were performed at a later time, which allowed the comparison of a CdTe assembly with a newer high-flux capable CdZnTe (HF-CZT) assembly. Part of this second subsection is taken from [1].

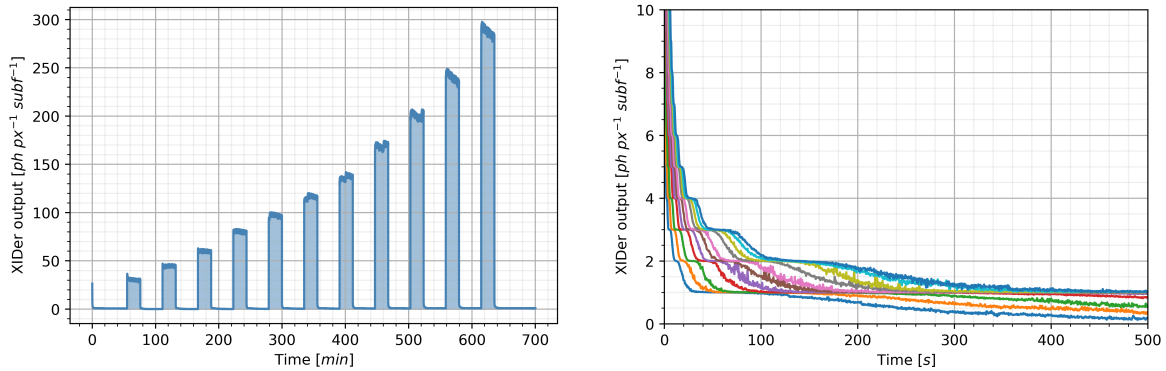
### 5.5.1 Measuring the slow afterglow components under X-ray irradiation

This subsection presents the residual afterglow of XIDer prototype PAT25, a 1 mm thick Ohmic CdTe assembly with 200 µm pixel pitch, under monochromatic 30 keV X-ray irradiation, in the quasi-uniform 7/8+1 ESRF filling mode (see Figure 1.3).

The same aluminium filter system as in the previous section is used to adjust the flux incident on the assembly. The beam is slitted down to approximately $1\,\mathrm{mm}^2$ and is centred on the 16-pixel matrix. The results shown here focus on one central pixel, which was calibrated for the energy of 30 keV. A subframe duration of 2 µs with 1.65 µs active integration window is used, unsynchronised to the beam time structure, similarly to the measurements presented in Subsections 5.3.2 and 5.3.3, which were performed during the same beamtime.

The beam flux is adapted by using 11 different configurations of Al filters attenuating the beam between approximately 30 and $300\,\mathrm{ph\,px^{-1}\,subf^{-1}}$, which translates to between $5 \times 10^8$ and $5 \times 10^9\,\mathrm{ph\,mm^{-2}\,s^{-1}}$. Each flux is left to stabilise for 20 min, after which the beam shutter is closed. The complete process of closing the beam shutter takes a couple of seconds, but the slitted down beam is entirely shut within a few hundreds of milliseconds. During this measurement procedure, PAT25 is programmed to acquire and average a burst of 9000 subframes every 0.5 s. The total acquisition is represented in Figure 5.13a. Because of the long time scale investigated here, the beam decay and beam refill period can be observed on the flux steps.

For the 11 different fluxes probed, the aftersignal once the illumination is stopped can be compared. Figure 5.13b shows the overlap of the 11 such aftersignals retrieved, with the larger the preceding beam flux, the larger the aftersignal amplitude.




**(a)** Fluxes probed **(b)** Aftersignals retrieved

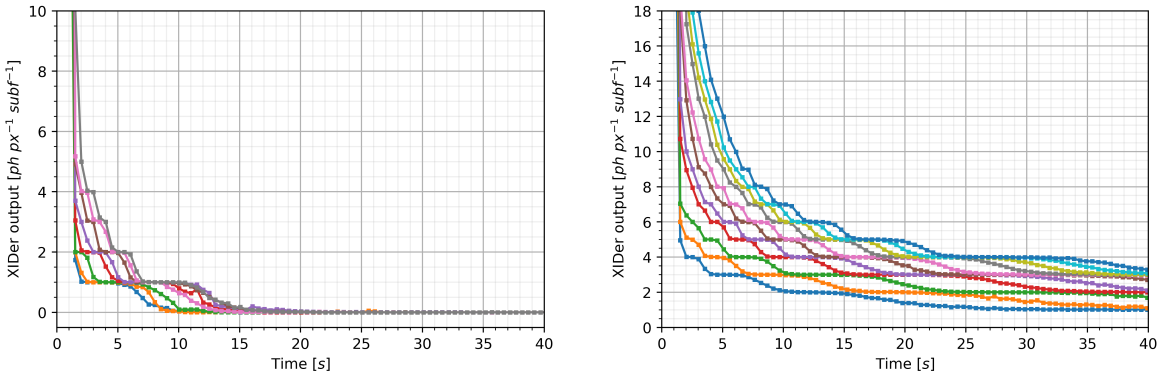
**Figure 5.13.** Probing the slow afterglow of a calibrated PAT25 front-end, under 30 keV X-ray irradiation. The 11 fluxes are each measured for 20 min. Data points are taken every 0.5 s and are the average of 9000 subframes.

The aftersignals are observe to decrease over the course of minutes, in steps due to digitisation. The aftersignals have multiple time components, with contributions from a continuum of trap energies, and a non-linear dependence on the previous irradiation.

The same experiment can be repeated with the 100 µm pixel pitch assembly PAT18.

The zoomed-in aftersignals for PAT18 and PAT25 are shown in Figure 5.14. The afterglow is much lower for the smaller pitch assembly, which is largely due to the difference in pixel area and digitisation. This is a convincing argument for the smaller pixel pitch size.

It should be noted that at this time scale, the HF-CZT assemblies would not show any significant residual aftersignal [1].




**(a)** 100 µm pixel pitch assembly PAT18 **(b)** 200 µm pixel pitch assembly PAT25

**Figure 5.14.** Slow afterglow of a 100 µm and a 200 µm pixel pitch assemblies under 30 keV X-ray irradiation.

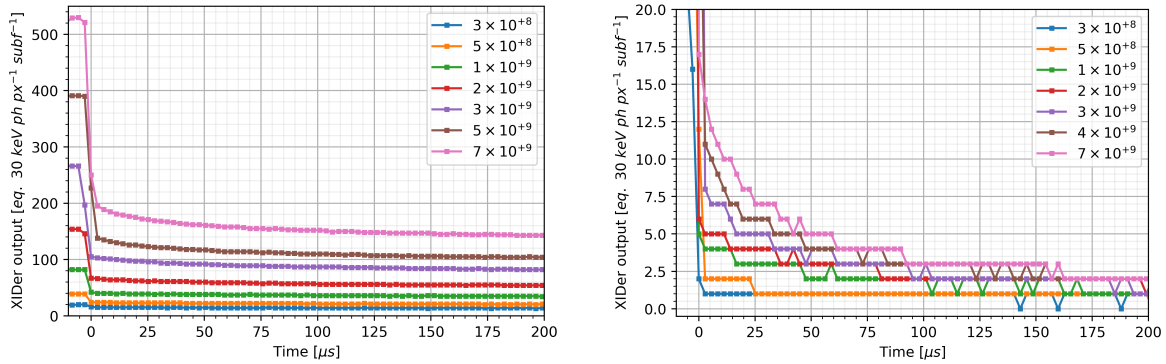
### 5.5.2 Measuring the microsecond time scale afterglow components under pulsed LED irradiation

This subsection presents the evaluation of the fast component of the photocurrent aftersignal transients of HF-CZT and CdTe pixelated sensors. For this purpose, the following results were obtained from the 200 µm pixel pitch XIDer assembly PAT21 (CdTe) and PAT39 (HF-CZT), both calibrated to operate with 30 keV photons. The measurements were performed by illuminating the assemblies with LED light emulating low-energy X-rays. Again, despite the use of visible light, all intensity values for both incident and measured intensities in this example are referenced to 30 keV equivalent photons. Values of incident intensity are those measured by the XIDer prototype assemblies, which are assumed to be well calibrated for the photon energy of 30 keV. It is worth noting that this would not be fully valid to provide accurate absolute flux values if the charge generation or the collection efficiency in the sensors is not ideal, but it can be taken as an adequate approximation to investigate the dynamic performance of the leakage current and the aftersignal effects.

During the measurements, the assemblies are illuminated with a 5 Hz square waveform of 50% duty cycle that corresponds to light pulses of 100 ms duration. The XIDer

readout is set to acquire single subframes with a repetition period of 2.80 µs. In those conditions, the active integration window within each subframe period is of 1.97 µs. The LED source was independently characterised with a silicon photodiode to verify the proper waveform shape and that the actual light emission fully decayed to zero in less than 1 µs at the falling edges of the illumination pulses.

Figure 5.15a shows the falling edges of sensor current under the pulsed illumination for the CdTe and HF-CZT assemblies, for several light intensities ranging from 20 to 530 equivalent 30 keV photons per pixel per subframe, as measured by the assemblies. For the given pixel pitch and integration window, these correspond to fluxes from $3 \times 10^8$ to $7 \times 10^9$ ph mm$^{-2}$ s$^{-1}$. The figure shows the response of one of the 200 µm pixels of each assembly once the steady state has been reached after several cycles of pulsed illumination. The plots present the pixel signal integrated at each 2.80 µs subframe during the time interval immediately following the falling edge of the incident illumination. They illustrate the level and temporal evolution of the aftersignal from the sensors. The vertical axis in the plot for the HF-CZT assembly is expanded to reveal the aftersignal decay, which is between one and two orders of magnitude weaker than in the case of CdTe. Because the subframe acquisition is not synchronised with the periodic 5 Hz illumination pulses, the first subframe recorded after the initial signal drop is likely to include partial illumination and should be disregarded.




**(a)** CdTe assembly **(b)** HF-CZT assembly

**Figure 5.15.** Falling edges of the pulsed irradiation of hybridised HF-CZT and CdTe XIDer assemblies. Graph (a) shows the aftersignal of CdTe assembly PAT21, and graph (b) the zoomed-in aftersignal of HF-CZT assembly PAT39. In the legend, the incident flux in ph mm$^{-2}$ s$^{-1}$.

The aftersignal in HF-CZT is observed to decay very rapidly: for the highest flux probed, the HF-CZT aftersignal 50 µs after the LED illumination is stopped drops to 5 equivalent 30 keV ph, or 1% of the incident flux. After 200 µs, the same aftersignal drops to 2 ph, and then stays below 1 ph after 1 ms. Figure 5.15a also shows that

for the more moderate flux of $5 \times 10^8$ equivalent 30 keV ph mm$^{-2}$ s$^{-1}$, the HF-CZT aftersignal reaches the value of 1 ph within 25 µs. For all fluxes probed here, after a few hundred microseconds, the HF-CZT aftersignal integrated during one subframe drops below the preset discrimination threshold, corresponding to a photon energy of approximately 15 keV, which results in an effective null readout value. This illustrates how the analogue-to-digital conversion in the XIDer readout can completely discard residual signals by exploiting the intrinsic quantisation of the X-ray illumination. This is the key feature of the incremental digital integration readout that enables the aggregation of multiple subframes without accumulating undesired contributions such as aftersignal or leakage current, as long as they remain below the discrimination threshold.

In contrast, CdTe aftersignal is much higher and stays high for much longer. This is highlighted by Figure 5.16, which presents the aftersignal of CdTe and HF-CZT pixels, 10 and 100 µs after LED irradiation was stopped, as a function of incident X-ray flux, as recorded by the XIDer prototypes. Figure 5.16 shows that for the same fluxes, the aftersignals after 10 or 100 µs are 1 to 2 orders of magnitude higher in CdTe compared to HF-CZT. The CdTe aftersignal 100 µs after irradiation still represents 30 to 75% of the input irradiation signal, decreasing with increasing flux.

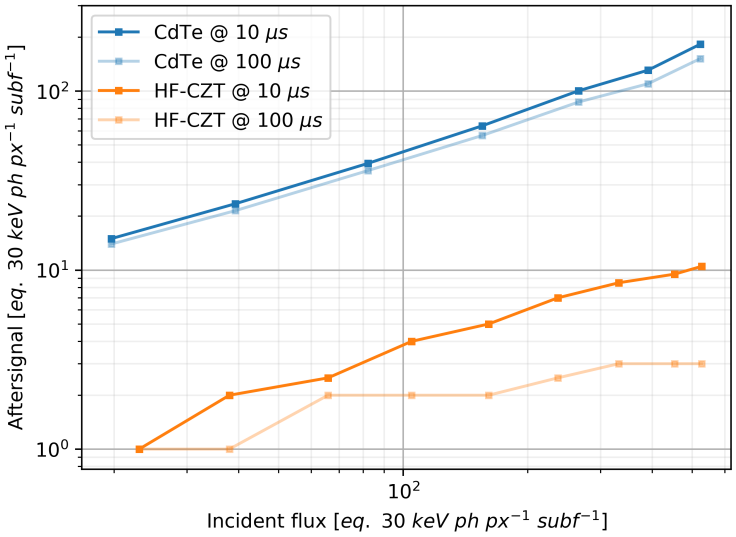



**Figure 5.16.** Aftersignal of a 200 µm XIDer pixel, converted in equivalent current density, at 10 µs and 100 µs after LED irradiation is stopped as a function of incident X-ray flux.

# Chapter 6

# Summary and conclusions

New-generation synchrotron radiation sources such as the ESRF-EBS are able to produce X-ray beams with a photon flux up to three orders of magnitude higher than previous-generation sources, sometimes exceeding $10^9$ monochromatic photons per second per pixel, and with photon energies of up to 100 keV [8]. State-of-the-art photon-counting hybrid pixel detectors present issues of pulse pile-up and cannot manage such elevated flux levels, with for instance the Dectris EIGER2 being rated for a maximum flux of $10^7$ ph/s/pixel [18]. It is critical for the synchrotron community to address this limitation, and it requires the development of novel detectors that surpass the constraints of current devices, both in terms of readout electronics and sensor material. Novel detectors should be highly versatile in operation mode to cover a wide range of applications, from fast high-energy diffraction experiments, where it is key to resolve in time the 5.68 MHz X-ray emission, to more conventional experiments with a longer exposure.

A first challenge lies in the selection of an adequate sensor material that is suited for the detection of X-rays in the 30–100 keV energy range. At these energies, silicon has too low an absorption efficiency to be reliably used. High-density compound semiconductor materials based on cadmium telluride are favoured, namely CdTe and CdZnTe, despite their issues such as aftersignal and polarisation resulting from imperfections in the crystal growth.

Specifically with versatility of operation in mind, a novel readout scheme, incremental digital integration, has been implemented through the XIDer project, a collaboration between the ESRF and Heidelberg University. Based on the quantisation of signal in very short exposure frames (subframes), this readout scheme is able to sustain a very high dynamic range and exhibits by design a reduced sensitivity to parasitic variations such as dark current and aftersignal when compared to a conventional charge-integrating readout, provided these contributions remain below a

discrimination threshold.

Monte-Carlo simulations were performed with the in-house detector simulation tool X-DECIMO to evaluate the *a priori* performance of a digitally integrating detector employing a 1-mm thick Cd(Zn)Te sensor with 100 µm pixel pitch under monochromatic X-ray irradiation with energy up to 100 keV. These simulations highlighted that readout losses in digital integration, inherent to the quantisation process, are strongly linked to charge sharing and partial charge collection at the pixel level. Digital integration was shown to be functionally equivalent to a photon-counting readout scheme at photon fluxes below 0.01 ph/subframe/pixel, corresponding to 1 Mph/s/mm$^2$ for a 2.8 µs subframe with the simulated parameters. These low-flux readout losses also have a dependency on the source photon energy because of physical phenomena such as fluorescence of the cadmium and tellurium atoms, with losses sometimes reaching more than 25% of the collected signal. At very high fluxes, above 3 ph/subframe/pixel, or 300 Mph/s/mm$^2$, the readout becomes akin to a conventional charge-integrating detector, and losses disappear as partial charge collection cancels out between neighbouring pixels.

Research and development of XIDer has been an iterative process, with several generations of prototypes. The experimental part of this manuscript focused on the fourth generation of prototype XIDer assemblies, the latest at the time of writing, consisting of a 16-pixel Cd(Zn)Te sensor with 100 or 200 µm pixel pitch, bump-bonded to a custom-designed TSMC 65 nm readout ASIC. This ASIC implements incremental digital integration in two stages, the first stage counting in packets of 8 ph and the second in packets of 1 ph, both using a charge removal concept. Such a two-stage implementation is helpful to maximise dynamic range and retain single photon resolution, but as foreseen in simulations, requires precise calibration of each pixel front-end to preserve the received Poisson-like photon distributions. The conceived calibration procedure, based on the internal injection circuit inside the chip, consists in the trimming of two key digital-to-analogue converters, the quantisation threshold and the charge packet size (quantisation step), in both stages of each pixel. This calibration requires calculations based on the nominal values of certain electrical components inside the chip, and is therefore limited by the components manufacturing tolerance. The complementary approach to refine this calibration procedure will be to exploit a source of known energy, for instance fluorescence photons.

Several sources were used to characterise the calibration and the performance of prototype XIDer assemblies: internal charge injection (circuit from inside the chip itself), external charge injection (from a waveform generator), a pulsed visible-light LED circuit, and the ESRF BM05 beamline monochromatic X-rays. Calibration as-

sessment measurements have shown the success of the calibration procedure, within the specified tolerance.

Table 6.1 shows a summary of key targets of the XIDer detector project compared to what is achieved by this generation of prototypes. In total more than 40 prototype assemblies have been built since the project started. The focus of the manuscript was on a few selected CdTe assemblies with Ohmic contacts, chosen for their uniform and stable response to light. Once it became available, assemblies using the high-flux capable CdZnTe (HF-CZT) material were produced. The hybridisation process was observed to be very reliable, with close to a 100% yield for later 200 µm pixel pitch prototypes.

Electronic noise in a prototype assembly was measured to be around 1 $ke^-$ rms, which is equivalent to 5 keV rms in Cd(Zn)Te. Although this is already small enough to have single-photon resolution at energies of 30 keV and higher, it is worth noting that two-thirds of this noise is related to the parasitic capacitance, notably of the sensor input pads and wires, which will be drastically reduced in the future iteration of prototypes. Analyses of dark images using a 15 keV discrimination threshold showed that the low-leakage CdZnTe assemblies count approximately 5 false hits per second, and confirms the prototypes single-photon sensitivity. This value can be much higher for biased CdTe assemblies, reaching hundreds of thousands of false hits per second, which highlights the crucial need for a leakage current compensation system.

The maximum achievable dynamic range of the prototypes is directly linked to the driving frequency of the charge removing mechanism. The charge pump was successfully operated at 78 MHz, resulting in a maximum photon flux of 680 Mcps/pixel. The charge removal circuit was designed to handle a 200 MHz frequency [99], but the driving frequency is currently limited by the readout PCB. This is also limiting the internal frame rate to around 1 MHz, even though subframes can already be set to be smaller than 500 ns and capture individual bunches in the 4-bunch ESRF mode. The in-pixel pre-amplifier was observed to be fast enough to distinguish individual X-ray bunches separated by 176 ns in the most demanding 16-bunch ESRF filling mode, but there is still considerable gain to be made in dead time compression to push the frame rate to 5.68 MHz and be able to integrate each bunch individually. This will come at the expense of higher driving currents in the front-end electronics, and consequently higher power dissipation.

At the BM05 beamline, CdTe assemblies were observed to behave linearly under 30 keV irradiation, although they reliably measured approximately 40% extra signal relative to a silicon photodiode reference. This extra signal is thought to be caused by a flux-induced leakage current of the CdTe sensor, as supported by investigations using

the fast pulsed LED system, which at the same time demonstrated the microsecond time-resolved and synchronisation capabilities of the prototypes. This flux-induced sensor leakage is not very well characterised in the literature, and may be detrimental to the detector performance, as it is skewing the recorded distribution of counts, and can remain significant for tens of seconds after irradiation is stopped. In contrast, it took HF-CZT assemblies only a few hundreds of microseconds to reach negligible levels of leakage.

The XIDer collaboration has successfully proved that incremental digital integration is a winning choice for future detectors. Most detector parameters are approaching the project targets, although it is expected that the energy dissipation occurring when the internal frame rate is pushed to 5.68 MHz will be an engineering challenge in larger scale prototypes. The other significant challenge stems from the non-idealities of high-density sensor materials due to their complex electrical properties. High-flux CdZnTe appears to be the best option, owing to its low leakage and fast dynamics. Nevertheless, this material must be characterised also at higher X-ray energies, as electron holes play a bigger role in the charge collection process.

Finally, research and development of the XIDer project continues as the collaboration was extended with DynamiX, composed of STFC (Science and Technology Facilities Council) and the Diamond Light Source, to form the XIDyn collaboration and pursue a common platform based on incremental digital integration. The European XFEL (X-Ray Free-Electron Laser Facility) has also recently joined the collaboration, as they are planning to upgrade to higher X-ray energies. The detector development is progressing, with the sixth generation, a 16×16 pixel prototype, now being characterised.

**Table 6.1.** Goals achieved with XIDer prototypes based with ASIC T4

| **Main features** | **Target** | **Achievements** |
|---|---|---|
| **Sensor** | | |
| Sensor material | Cd(Zn)Te | Successful, good hybridisation yield |
| | GaAs:Cr | Low yield, high leakage, procurement stopped |
| Energy range | 30-100 keV | Main experimental focus at 30 keV |
| | | Sufficient absorption of Cd(Zn)Te up to 100 keV |
| Pixel size | 100-200 um | Both 100 and 200 um pixel pitches achieved |
| | | More reliable hybridisation yield with 200 um |
| Noise | 1-ph resolution in Cd(Zn)Te | ASIC only: ∼370 e- rms, eq. to 1.7 keV |
| | | ASIC+sensor: ∼1 ke- rms, eq. to 5 keV |
| | | ->Enough for 1-ph sensitivity at 30 keV |
| **Pulsed mode** | *4&16-bunch mode* | |
| Max. flux / pixel | ∼250 ph/pulse | ∼250 ph/pulse if active subf. duration >370 ns |
| Cycle dead time | <=170 ns | ∼350 ns |
| Internal frame rate | 1.42 MHz | Achievable, but readout PCB limits to ∼1 MHz |
| | 5.68 MHz | Not yet achieved |
| **Continuous mode** | *7/8+1 mode* | |
| Max. photon flux | ∼1500 Mcps/pixel | ∼680 Mcps/pixel, limited by readout PCB |
| Max. total signal | selectable | Subframe aggregation possible with telegram |

**Contributions**

The author:

- Used Monte-Carlo detector simulation tool X-DECIMO to assess performance of CdTe sensors and systems implementing digital integration, in terms of losses, non-linearity, spatial resolution and noise power spectrum. Defined simulation and analysis protocols. Helped maintain and resolve issues during X-DECIMO development. Conceived Python scripts to simulate and study the detector behaviour with electronic noise, sensor leakage current, calibration defects.

- Carried out the experimental characterisation of the electrical properties and leakage current of CdTe (with Ohmic and Schottky contacts), high-flux CdZnTe, and GaAs:Cr sensor slab samples under high-voltage biasing.

- Developed high-level Python modules to provide fast versatile control and programming of the assemblies. Edited the low-level Python modules controlling the ASIC and FPGA called by the high-level modules. Conceived and implemented automatic calibration procedures. Developed data structures, based on the hdf5 format, to write and load output data and metadata resulting of XIDer measurements.

- Inspected and assessed the quality and the hybridisation yield of 42 prototype assemblies (see Appendix 7.1). Assessed the calibration and performance of the front-end electronics with developed software tools and oscilloscope. Investigated the stability in time of biased assemblies when irradiated with visible-light LED, and with low-energy X-rays from the in-lab X-ray generator. Participated in six multi-days beam times to characterise the detector system behaviour under synchrotron X-ray light; specifically, the author was in charge of the prototype control and programming tailored for each measurement. Developed Python scripts to analyse calibration and characterisation data outputs. Within the scope of this work, all data analysed was produced with the author involvement, and the analysis of all data presented in the manuscript was carried out the author.

- Performed a poster presentation on simulation work at iWoRiD 2021, and an oral presentation on experimental results at IEEE NSS MIC RTSD 2022. Wrote as first-author Article [91] on simulations, and Article [1] on characterisation data. Participated in the data recording, analysis, and elaboration of Articles [111, 112, 118].

# Chapter 7

# Appendix

## 7.1 Table of hybridised prototype assemblies

In tables 7.1 and 7.2 are shown a complete listing of assemblies with ASIC T2 and ASIC T4 versions. The ASIC chips were all hybridised by Polymer Assembly Technology (PAT) to a sensor with 100 µm or 200 µm pixel pitch. The sensor type is either of the following:

- CdTe with Ohmic contacts, manufactured by Acrorad Co. Ltd.
- CdTe with Schottky diode contacts, manufactured by Acrorad Co. Ltd.
- Chromium-compensated GaAs or GaAS:Cr, provided by Tomsk State University
- CdZnTe with Ohmic contacts, provided by Due2Lab (CdZnTe material from Redlen)

**Table 7.1.** Table of hybridised assemblies with ASIC T2 chip.

| Assembly | Sensor | Pitch | Yield | Notes |
|---|---|---|---|---|
| PAT01 | CdTe - Ohmic | 100 µm | 4/16 | Issue with ground plane |
| PAT02 | CdTe - Ohmic | 200 µm | 16/16 | Issue with ground plane |
| PAT03 | CdTe - Ohmic | 100 µm | 8/16 | Issue with ground plane |
| PAT04 | CdTe - Schottky | 200 µm | 16/16 | Issue with ground plane |
| PAT05 | CdTe - Ohmic | 200 µm | 0/16 | |
| PAT06 | CdTe - Schottky | 100 µm | 2/16 | High leakage from working pixels |
| PAT07 | CdTe - Ohmic | 100 µm | 9/16 | |
| PAT08 | CdTe - Ohmic | 200 µm | 16/16 | High leakage in all pixels |
| PAT09 | CdTe - Schottky | 100 µm | 10/16 | Very poor light sensitivity |
| PAT10 | CdTe - Schottky | 100 µm | 10/16 | Very damaged sensor |
| PAT11 | CdTe - Schottky | 100 µm | 3/16 | |
| PAT12 | CdTe - Schottky | 100 µm | 0/16 | |
| PAT13 | CdTe - Schottky | 200 µm | 16/16 | Very unstable light response |
| PAT14 | CdTe - Schottky | 200 µm | 16/16 | Very unstable light response |
| PAT15 | GaAs:Cr | 100 µm | 13/16 | Very poor light sensitivity |
| PAT16 | GaAs:Cr | 100 µm | 9/16 | |
| PAT17 | GaAs:Cr | 100 µm | 8/16 | |

**Table 7.2.** Table of hybridised assemblies with ASIC T4 chip.

| Assembly | Sensor | Pitch | Yield | Notes |
|---|---|---|---|---|
| PAT18 | CdTe - Ohmic | 100 µm | 16/16 | Very uniform light response |
| PAT19 | CdTe - Ohmic | 100 µm | 16/16 | Highly non-uniform light response |
| PAT20 | CdTe - Ohmic | 200 µm | 11/16 | |
| PAT21 | CdTe - Ohmic | 200 µm | 16/16 | Very uniform light response |
| PAT22 | CdTe - Schottky | 100 µm | 16/16 | Highly non-uniform light response |
| PAT23 | CdTe - Ohmic | 100 µm | 16/16 | Spatial gradient in light response |
| PAT24 | GaAs:Cr | 200 µm | 8/16 | Poor light sensitivity and gradient |
| PAT25 | CdTe - Ohmic | 200 µm | 16/16 | Very uniform light response |
| PAT26 | CdTe - Ohmic | 100 µm | 15/16 | Highly non-uniform light response |
| PAT27 | CdTe - Ohmic | 200 µm | 16/16 | |
| PAT28 | CdTe - Schottky | 100 µm | 16/16 | Spatial gradient in light response |
| PAT29 | CdTe - Schottky | 200 µm | 0/16 | |
| PAT30 | CdTe - Schottky | 200 µm | 16/16 | Spatial gradient in light response |
| PAT31 | GaAs:Cr | 200 µm | 4/16 | Only bottom row of pixels is functional |
| PAT32 | CdTe - Schottky | 100 µm | 16/16 | Highly non-uniform light response |
| PAT33 | CdTe - Schottky | 200 µm | 16/16 | Highly non-uniform light response |
| PAT34 | GaAs:Cr | 200 µm | 4/16 | Only bottom row of pixels is functional |
| PAT35 | CdTe - Schottky | 200 µm | 16/16 | Most pixels have very poor light sensitivity |
| PAT36 | CdTe - Schottky | 100 µm | 16/16 | Highly non-uniform light response |
| PAT37 | GaAs:Cr | 200 µm | 4/16 | Only left row of pixels is functional |
| PAT38 | CdZnTe - Ohmic | 200 µm | 16/16 | |
| PAT39 | CdZnTe - Ohmic | 200 µm | 16/16 | |
| PAT40 | CdZnTe - Ohmic | 200 µm | 16/16 | |
| PAT41 | CdZnTe - Ohmic | 200 µm | 16/16 | |
| PAT42 | CdZnTe - Ohmic | 200 µm | 16/16 | |

# Bibliography


[1] M. Collonge, O. Baussens, P. Busca, P. Fajardo, M. Ruat, and M. Williams. Probing the potential of CdZnTe for high-energy high-flux 2D X-ray detection using the XIDer incremental digital integrating readout. *Frontiers in Physics*, Pushing Frontiers - Imaging for Photon Science, February 2024.

[2] R. Dimper, H. Reichert, P. Raimondi, L. S. Ortiz, F. Sette, J. Susini, G. Admans, P. Berkvens, A. Kaprolat, and J.L. Revol. ESRF upgrade programme phase II (Orange book). *ESRF*, 2014.

[3] ESRF. Facts and Figures. `https://www.esrf.fr/home/UsersAndScience/Publications/Highlights/highlights-2017.html/facts-and-figures.html`, Last Modified: 22 Mar 2018.

[4] J.C. Biasci, J.F. Bouteille, N. Carmignani, J. Chavanne, D. Coulon, Y. Dabin, F. Ewald, L. Farvacque, L. Goirand, M. Hahn, J. Jacob, G. LeBec, S. Liuzzo, B. Nash, H. Pedroso-Marques, T. Perron, E. Plouviez, P. Raimondi, J.L. Revol, K. Scheidt, and V. Serrière. A Low-Emittance Lattice for the ESRF. *Synchrotron Radiation News*, 27(6):8–12, November 2014.

[5] P. Raimondi, N. Carmignani, L. R. Carver, J. Chavanne, L. Farvacque, G. Le Bec, D. Martin, S. M. Liuzzo, T. Perron, and S. White. Commissioning of the hybrid multibend achromat lattice at the European Synchrotron Radiation Facility. *Physical Review Accelerators and Beams*, 24(11):110701, November 2021.

[6] J. Susini, R. Barrett, J. Chavanne, P. Fajardo, A. Götz, J.L. Revol, and L. Zhang. New challenges in beamline instrumentation for the ESRF Upgrade Programme Phase II. *Journal of Synchrotron Radiation*, 21(Pt 5):986–995, September 2014.

[7] P. Raimondi. ESRF-EBS: The Extremely Brilliant Source Project. *Synchrotron Radiation News*, 29(6):8–15, November 2016.

[8] L. Farvacque, G. Le Bec, J.C. Biasci, J.F. Bouteille, J. Jacob, J.M. Chaize, K. Scheidt, J. Chavanne, T. Perron, S. White, M. Hahn, D. Martin, and P. Raimondi. EBS Storage Ring Technical Report. *ESRF*, 2018.

[9] ESRF. EBS Parameters. `https://www.esrf.fr/home/UsersAndScience/Accelerators/ebs---extremely-brilliant-source/ebs-parameters.html`, Last Modified: 08 Oct 2020.

[10] ESRF. ESRF-EBS: A new generation of synchrotron for Europe, 2020. `https://www.esrf.fr/files/live/sites/www/files/about/upgrade/documentation/EBSPressKit.pdf`.

[11] L. Rossi, P. Fischer, T. Rohe, and N. Wermes. *Pixel Detectors: From Fundamentals to Applications*. Particle Acceleration and Detection. Springer, 2006.

[12] C. Brönnimann and P. Trüb. Hybrid Pixel Photon Counting X-Ray Detectors for Synchrotron Radiation. In E. J. Jaeschke, S. Khan, J. R. Schneider, and J. B. Hastings, editors, *Synchrotron Light Sources and Free-Electron Lasers: Accelerator Physics, Instrumentation and Science Applications*, pages 1191–1223. Springer International Publishing, 2020.

[13] R. Ballabriga, G. Blaj, M. Campbell, M. Fiederle, D. Greiffenberg, E. H. M. Heijne, X. Llopart, R. Plackett, S. Procz, L. Tlustos, D. Turecek, and W. Wong. Characterization of the Medipix3 pixel readout chip. *Journal of Instrumentation*, 6(01):C01052, January 2011.

[14] P. Maj, T. Taguchi, and Y. Nakaye. Tests of UFXC32k chip with CdTe pixel detector. *Journal of Instrumentation*, 13(02):C02014, February 2018.

[15] T. Donath, D. Šišak Jung, M. Burian, V. Radicci, P. Zambon, A. N. Fitch, C. Dejoie, B. Zhang, M. Ruat, M. Hanfland, C. M. Kewish, G. A. van Riessen, D. Naumenko, H. Amenitsch, G. Bourenkov, G. Bricogne, A. Chari, and C. Schulze-Briese. EIGER2 hybrid-photon-counting X-ray detectors for advanced synchrotron diffraction experiments. *Journal of Synchrotron Radiation*, 30(4):723–738, July 2023.

[16] K. Medjoubi, S. Hustache, F. Picca, J. F. Bérar, N. Boudet, F. Bompard, P. Breugnon, J.-C. Clémens, A. Dawiec, P. Delpierre, B. Dinkespiler, S. Godiot, J.-P. Logier, M. Menouni, C. Morel, M. Nicolas, P. Pangaud, and E. Vigeolas. Performance and Applications of the CdTe- and Si-XPAD3 photon counting 2D detector. *Journal of Instrumentation*, 6(01):C01080, January 2011.

[17] S. Tsigaridas and C. Ponchut. X-ray imaging with high-Z sensors for the ESRF-EBS Upgrade. *Journal of Instrumentation*, 14(04):C04009, April 2019.

[18] DECTRIS. EIGER2 X CdTe, March 2023. `https://www.dectris.com/detectors/x-ray-detectors/eiger2/eiger2-for-synchrotrons/eiger2-x-cdte/`.

[19] W. Becker. *Advanced Time-Correlated Single Photon Counting Techniques*, volume 81 of *Springer Series in Chemical Physics*. Springer, 2005.

[20] T. Loeliger, C. Brönnimann, T. Donath, M. Schneebeli, R. Schnyder, and P. Trüb. The new PILATUS3 ASIC with instant retrigger capability. In *2012 IEEE Nuclear Science Symposium and Medical Imaging Conference Record (NSS/MIC)*, pages 610–615, October 2012.

[21] M. C. Veale, P. Adkin, P. Booker, J. Coughlan, M. J. French, M. Hart, T. Nicholls, A. Schneider, P. Seller, I. Pape, K. Sawhney, G. A. Carini, and P. A. Hart. Characterisation of the high dynamic range Large Pixel Detector (LPD) and its use at X-ray free electron laser sources. *Journal of Instrumentation*, 12(12):P12003, December 2017.

[22] A. Allahgholi, J. Becker, A. Delfs, R. Dinapoli, P. Goettlicher, D. Greiffenberg, B. Henrich, H. Hirsemann, M. Kuhn, R. Klanner, A. Klyuev, H. Krueger, S. Lange, T. Laurus, A. Marras, D. Mezza, A. Mozzanica, M. Niemann, J. Poehlsen, J. Schwandt, I. Sheviakov, X. Shi, S. Smoljanin, L. Steffen, J. Sztuk-Dambietz, U. Trunk, Q. Xia, M. Zeribi, J. Zhang, M. Zimmer, B. Schmitt, and H. Graafsma. The Adaptive Gain Integrating Pixel Detector at the European XFEL. *Journal of Synchrotron Radiation*, 26(1):74–82, January 2019.

[23] D. Magalhães, P. Fajardo, P. Gryboś, R. Kleczek, P. Kmon, P. Otfinowski, and M. Ruat. Characterization results of the first small pixel high rate (SPHIRD) photon counting hybrid pixel detector prototypes.

[24] P. Grybos, R. Kleczek, P. Kmon, P. Otfinowski, P. Fajardo, D. Magalhães, and M. Ruat. SPHIRD–Single Photon Counting Pixel Readout ASIC With Pulse Pile-Up Compensation Methods. *IEEE Transactions on Circuits and Systems II: Express Briefs*, 70(9):3248–3252, September 2023.

[25] P. Fajardo, P. Busca, F. Erdinger, P. Fischer, M. Ruat, and D. Schimansky. Digital integration: a novel readout concept for XIDER, an X-ray detector for the next generation of synchrotron radiation sources. *Journal of Instrumentation*, 15(01):C01040, January 2020.

[26] Hamamatsu. High resolution X-ray imaging system. `https://www.hamamatsu.com/content/dam/hamamatsu-photonics/sites/documents/99_SALES_LIBRARY/sys/SCAS0011E_M11427.pdf`, Last Modified: Dec 2023.

[27] Photonic Science. X-ray FDS Detector. `https://photonicscience.com/products/x-ray-cameras/x-ray-fds-detector/`, Last Modified: Jun 2023.

[28] R. Turchetta, A. Fant, P. Gasiorek, C. Esbrand, J.A. Griffiths, M.G. Metaxas, G.J. Royle, R. Speller, C. Venanzi, P.F. Van Der Stelt, H. Verheij, G. Li, S. Theodoridis, H. Georgiou, D. Cavouras, G. Hall, M. Noy, J. Jones, J. Leaver, D. Machin, S. Greenwood, M. Khaleeq, H. Schulerud, J.M. Østby, F. Triantis, A. Asimidis, D. Bolanakis, N. Manthos, R. Longo, and A. Bergamaschi. CMOS Monolithic Active Pixel Sensors (MAPS): Developments and future outlook. *Nuclear Instruments and Methods in Physics Research Section A: Accelerators, Spectrometers, Detectors and Associated Equipment*, 582(3):866–870, December 2007.

[29] C. B. Wunderer, J. Correa, A. Marras, S. Aplin, B. Boitrelle, P. Goettlicher, F. Krivan, M. Kuhn, S. Lange, M. Niemann, F. Okrent, I. Shevyakov, M. Zimmer, N. Guerrini, B. Marsh, I. Sedgwick, G. Cautero, D. Giuressi, I. Gregori, G. Pinaroli, R. Menk, L. Stebel, A. Greer, T. Nicholls, U. K. Pedersen, N. Tartoni, H. Hyun, K. Kim, S. Rah, and H. Graafsma. The Percival 2-Megapixel monolithic active pixel imager. *Journal of Instrumentation*, 14(01):C01006, January 2019.

[30] T. Hatsui. CITIUS: a 17400 frames/s x-ray imaging detector, 2022.

[31] I. Mouhti, A. Elanique, M. Y. Messous, A. Benahmed, J. E. McFee, Y. Elgoub, and P. Griffith. Characterization of CsI(Tl) and LYSO(Ce) scintillator detectors by measurements and Monte Carlo simulations. *Applied Radiation and Isotopes*, 154:108878, December 2019.

[32] Saint-Gobain Crystals. Cesium Iodide Scintillation Material. `https://www.gammadata.se/assets/Uploads/CsITl-and-Na-data-sheet.pdf`, Last Modified: Apr 2023.

[33] K. Pauwels and P.A. Douissard. Indirect X-ray detectors with single-photon sensitivity. *Journal of Synchrotron Radiation*, 29(Pt 6):1394–1406, October 2022.

[34] A. Yoneyama, R. Baba, and M. Kawamoto. Quantitative analysis of the physical properties of CsI, GAGG, LuAG, CWO, YAG, BGO, and GOS scintillators using 10-, 20- and 34-keV monochromated synchrotron radiation. *Optical Materials Express*, 11(2):398–411, February 2021.

[35] R. Morlotti, M. Nikl, M. Piazza, and C. Boragno. Intrinsic conversion efficiency of X-rays to light in $Gd_2O_2S : Tb^{3+}$ powder phosphors. *Journal of Luminescence*, 72-74:772–774, June 1997.

[36] Spectrum Logic. Spectrum Logic 2824HS CMOS X-ray Detector. `https://static1.squarespace.com/static/5ae6dd648f51303ed37b4cdd/t/65afea094aae0c22cb21d232/1706027530201/SL+2824HS.pdf`, Last Modified: 12 Nov 2021.

[37] C. M. Davisson. Interaction of  -radiation with Matter. In K. Siegbahn, editor, *Alpha-, Beta- and Gamma-Ray Spectroscopy*, pages 37–78. Elsevier, January 1968.

[38] T. Schoonjans, A. Brunetti, B. Golosio, M. S. del Rio, V. A. Sole, C. Ferrero, and L. Vincze. The xraylib library for X-ray-matter interactions : recent developments. *SPECTROCHIMICA ACTA PART B-ATOMIC SPECTROSCOPY*, 66(11-12):776–784, 2011.

[39] NIST. X-Ray Mass Attenuation Coefficients. *NIST*, September 2009.

[40] F. Principato, M. Bettelli, A. Zappettini, and L. Abbene. A Novel Extraction Procedure of Contact Characteristic Parameters from Current–Voltage Curves in CdZnTe and CdTe Detectors. *Sensors (Basel, Switzerland)*, 23(13):6075, July 2023.

[41] L. Abbene, G. Gerardi, A. A. Turturici, S. Del Sordo, and F. Principato. Experimental results from Al/p-CdTe/Pt X-ray detectors. *Nuclear Instruments and Methods in Physics Research Section A: Accelerators, Spectrometers, Detectors and Associated Equipment*, 730:135–140, December 2013.

[42] R. Grill, E. Belas, J. Franc, M. Bugar, Š. Uxa, P. Moravec, and P. Hoschl. Polarization Study of Defect Structure of CdTe Radiation Detectors. *IEEE Transactions on Nuclear Science*, 58(6):3172–3181, December 2011.

[43] A. Cola and I. Farella. The polarization mechanism in CdTe Schottky detectors. *Applied Physics Letters*, 94(10):102113, March 2009.

[44] A. Cola and I. Farella. CdTe X-ray detectors under strong optical irradiation. *Applied Physics Letters*, 105(20):203501, November 2014.

[45] D. S. Bale and C. Szeles. Nature of polarization in wide-bandgap semiconductor detectors under high-flux irradiation: Application to semi-insulating $Cd_{1-x}Zn_xTe$. *Physical Review B*, 77(3):035205, January 2008.

[46] P. Zambon. Simulation of polarization dynamics in semi-insulating, Cr-compensated GaAs pixelated sensors under high x-ray fluxes. *AIP Advances*, 11(7):075006, July 2021.

[47] X. Mathew. Photo-induced current transient spectroscopic study of the traps in CdTe. *Solar Energy Materials and Solar Cells*, 76(3):225–242, March 2003.

[48] H. F. Haneef, A. M. Zeidell, and O. D. Jurchescu. Charge carrier traps in organic semiconductors: a review on the underlying physics and impact on electronic devices. *Journal of Materials Chemistry C*, 8(3):759–787, January 2020.

[49] G. Ariño-Estrada, M. Chmeissani, G. de Lorenzo, M. Kolstein, C. Puigdengoles, J. García, and E. Cabruja. Measurement of mobility and lifetime of electrons and holes in a Schottky CdTe diode. *Journal of Instrumentation*, 9:C12032, December 2014.

[50] A. Cola and I. Farella. Electric fields and dominant carrier transport mechanisms in CdTe Schottky detectors. *Applied Physics Letters*, 102(11):113502, March 2013.

[51] J. Becker, M. W. Tate, K. S. Shanks, H. T. Philipp, J. T. Weiss, P. Purohit, D. Chamberlain, J. P. C. Ruff, and S. M. Gruner. Characterization of CdTe sensors with Schottky contacts coupled to charge-integrating pixel array detectors for X-ray science. *Journal of Instrumentation*, 11(12):P12013, December 2016.

[52] B. Thomas, M. C. Veale, M. D. Wilson, P. Seller, A. Schneider, and K. Iniewski. Characterisation of Redlen high-flux CdZnTe. *Journal of Instrumentation*, 12(12):C12045, December 2017.

[53] Y. Li, G. Zha, Y. Dabin, S. Xi, L. Xu, H. Yu, and W. Jie. Effects of deep-level traps on the transport properties of high-flux X-ray CdZnTe detectors. *Materials Science in Semiconductor Processing*, 133:105974, October 2021.

[54] T. Hatsui and H. Graafsma. X-ray imaging detectors for synchrotron and XFEL sources. *IUCrJ*, 2(3):371–383, May 2015.

[55] P. Grybos. *Front-end electronics for multichannel semiconductor detector systems*. Number 08 in EuCARD editorial series on accelerator science. 2010.

[56] P. Trueb, B. A. Sobott, R. Schnyder, T. Loeliger, M. Schneebeli, M. Kobas, R. P. Rassool, D. J. Peake, and C. Broennimann. Improved count rate corrections for highest data quality with PILATUS detectors. *Journal of Synchrotron Radiation*, 19(Pt 3):347–351, May 2012.

[57] P. Trueb, B. A. Sobott, R. Schnyder, T. Loeliger, M. Schneebeli, M. Kobas, R. P. Rassool, D. J. Peake, and C. Broennimann. Simulating the Counting Mechanism of PILATUS2 and PILATUS3 Detectors for Improved Count Rate Corrections. *Journal of Physics: Conference Series*, 425(6):062002, March 2013.

[58] P. Trueb, C. Dejoie, M. Kobas, P. Pattison, D. J. Peake, V. Radicci, B. A. Sobott, D. A. Walko, and C. Broennimann. Bunch mode specific rate corrections for PILATUS3 detectors. *Journal of Synchrotron Radiation*, 22(3):701–707, May 2015.

[59] D. Lee, K. Lim, K. Park, C. Lee, S. Alexander, and G. Cho. An innovative method to reduce count loss from pulse pile-up in a photon-counting pixel for high flux X-ray applications. *Journal of Instrumentation*, 12(03):P03006, March 2017.

[60] C. Schulze-Briese. The New PILATUS3 ASIC with Instant Retrigger Technology, September 2012.

[61] G. Blaj, P. Caragiulo, G. Carini, S. Carron, A. Dragone, D. Freytag, G. Haller, P. Hart, J. Hasi, R. Herbst, S. Herrmann, C. Kenney, B. Markovic, K. Nishimura, S. Osier, J. Pines, B. Reese, J. Segal, A. Tomada, and M. Weaver. X-ray detectors at the Linac Coherent Light Source. *Journal of Synchrotron Radiation*, 22(3):577–583, May 2015.

[62] S. Herrmann, S. Boutet, B. Duda, D. Fritz, G. Haller, P. Hart, R. Herbst, C. Kenney, H. Lemke, M. Messerschmidt, J. Pines, A. Robert, M. Sikorski, and G. Williams. CSPAD-140k: A versatile detector for LCLS experiments. *Nuclear Instruments and Methods in Physics Research Section A: Accelerators, Spectrometers, Detectors and Associated Equipment*, 718:550–553, August 2013.

[63] G. Blaj, A. Dragone, C. J. Kenney, F. Abu-Nimeh, P. Caragiulo, D. Doering, M. Kwiatkowski, B. Markovic, J. Pines, M. Weaver, S. Boutet, G. Carini, C.-E. Chang, P. Hart, J. Hasi, M. Hayes, R. Herbst, J. Koglin, K. Nakahara, J. Segal,

and G. Haller. Performance of ePix10K, a high dynamic range, gain auto-ranging pixel detector for FELs. *AIP Conference Proceedings*, 2054(1):060062, January 2019.

[64] A. Allahgholi, J. Becker, L. Bianco, A. Delfs, R. Dinapoli, P. Goettlicher, H. Graafsma, D. Greiffenberg, H. Hirsemann, S. Jack, R. Klanner, A. Klyuev, H. Krueger, S. Lange, A. Marras, D. Mezza, A. Mozzanica, S. Rah, Q. Xia, B. Schmitt, J. Schwandt, I. Sheviakov, X. Shi, S. Smoljanin, U. Trunk, J. Zhang, and M. Zimmer. AGIPD, a high dynamic range fast detector for the European XFEL. *Journal of Instrumentation*, 10(01):C01023, January 2015.

[65] A. Allahgholi, J. Allison, A. Delfs, R. Dinapoli, P. Göttlicher, H. Graafsma, D. Greiffenberg, H. Hirsemann, S. Jack, A. Klyuev, H. Krüger, M. Kuhn, T. Koi, A. Marras, D. Mezza, A. Mozzanica, J. Poehlsen, O. Shefer Shalev, I. Sheviakov, B. Schmitt, J. Schwandt, X. Shi, S. Smoljanin, U. Trunk, J. Zhang, and M. Zimmer. Megapixels @ Megahertz – The AGIPD high-speed cameras for the European XFEL. *Nuclear Instruments and Methods in Physics Research Section A: Accelerators, Spectrometers, Detectors and Associated Equipment*, 942:162324, October 2019.

[66] LXN | Paul Scherrer Institut (PSI). JUNGFRAU, March 2023. `https://www.psi.ch/en/lxn/jungfrau`.

[67] J. H. Smith, A. Mozzanica, and B. Schmitt. A Dynamic Gain Switching Detector for SwissFEL. Technical report, Paul Scherrer Institut, 2015.

[68] A. Mozzanica. Status of the JUNGFRAU project: detector design and result from the SwissFEL pilot experiment phase, 2018.

[69] F. Leonarski, A. Mozzanica, M. Brückner, C. Lopez-Cuenca, S. Redford, L. Sala, A. Babic, H. Billich, O. Bunk, B. Schmitt, and M. Wang. JUNGFRAU detector for brighter x-ray sources: Solutions for IT and data science challenges in macromolecular crystallography. *Structural Dynamics*, 7(1):014305, February 2020.

[70] A. Koch, M. Hart, T. Nicholls, C. Angelsen, J. Coughlan, M. French, S. Hauf, M. Kuster, J. Sztuk-Dambietz, M. Turcato, G. A. Carini, M. Chollet, S. C. Herrmann, H. T. Lemke, S. Nelson, S. Song, M. Weaver, D. Zhu, A. Meents, and P. Fischer. Performance of an LPD prototype detector at MHz frame rates under Synchrotron and FEL radiation. *Journal of Instrumentation*, 8(11):C11001, November 2013.

[71] M. Hart. The Large Pixel Detector for the European XFEL: overview of the system and experience of operation at the FXE beam line, 2018.

[72] F. Erdinger. *Design of Front End Electronics and a Full Scale 4k Pixel Readout ASIC for the DSSC X-ray Detector at the European XFEL.* PhD thesis, Heidelberg University, 2016.

[73] Pradeep Kalavakuru. The readout chip for the XFEL DSSC Detector: design and test, 2018.

[74] V. Sriskaran, J. Alozy, R. Ballabriga, M. Campbell, N. Egidos, J. M. Fernandez-Tenllado, E. Heijne, I. Kremastiotis, A. Koukab, X. Llopart, J. M. Sallese, and L. Tlustos. New architecture for the analog front-end of Medipix4. *Nuclear Instruments and Methods in Physics Research Section A: Accelerators, Spectrometers, Detectors and Associated Equipment*, 978:164412, October 2020.

[75] V. Sriskaran. *Medipix4, a high granularity four sides buttable pixel readout chip for high resolution spectroscopic X-ray imaging at rates compatible with medical CT scans.* PhD thesis, EPFL, 2022.

[76] X. Llopart, J. Alozy, R. Ballabriga, M. Campbell, R. Casanova, V. Gromov, E. H. M. Heijne, T. Poikela, E. Santin, V. Sriskaran, L. Tlustos, and A. Vitkovskiy. Timepix4, a large area pixel detector readout chip which can be tiled on 4 sides providing sub-200 ps timestamp binning. *Journal of Instrumentation*, 17(01):C01044, January 2022.

[77] X. Llopart. Timepix4, a pixel detector readout chip with sub-200 ps timestamp binning, February 2022.

[78] K. Heijhoff, K. Akiba, R. Ballabriga, M. van Beuzekom, M. Campbell, A. P. Colijn, M. Fransen, R. Geertsema, V. Gromov, and X. Llopart Cudie. Timing performance of the Timepix4 front-end. *Journal of Instrumentation*, 17(07):P07006, July 2022.

[79] R. Ballabriga, J. A. Alozy, F. N. Bandi, G. Blaj, M. Campbell, P. Christodoulou, V. Coco, A. Dorda, S. Emiliani, K. Heijhoff, E. Heijne, T. Hofmann, J. Kaplon, A. Koukab, I. Kremastiotis, X. Llopart, M. Noy, A. Paterno, M. Piller, J. M. Sallesse, V. Sriskaran, L. Tlustos, and M. van Beuzekom. The Timepix4 analog front-end design: Lessons learnt on fundamental limits to noise and time resolution in highly segmented hybrid pixel detectors. *Nuclear Instruments and Methods in Physics Research Section A: Accelerators, Spectrometers, Detectors and Associated Equipment*, 1045:167489, January 2023.

[80] L. Jones, S. Bell, B. Cline, T. Gardiner, M. Hart, M. Prydderch, P. Seller, M. Veale, and M. Wilson. Spectroscopic X-ray imaging at MHz frame rates — the HEXITEC$_{MHz}$ ASIC, September 2021.

[81] L. Jones, S. Bell, B. Cline, T. Gardiner, M. Hart, M. Prydderch, P. Seller, M. Veale, and M. Wilson. Spectroscopic X-ray imaging at MHz frame rates — the HEXITEC$_{MHz}$ ASIC. *Journal of Instrumentation*, 17(10):C10012, October 2022.

[82] Medipix Collaboration. Medipix3, March 2023. `https://medipix.web.cern.ch/medipix3`.

[83] P. Grybos, P. Kmon, P. Maj, and R. Szczygiel. 32k Channel Readout IC for Single Photon Counting Pixel Detectors with 75 µm Pitch, Dead Time of 85 ns, 9 $e^-$ rms Offset Spread and 2% rms Gain Spread. *IEEE Transactions on Nuclear Science*, 63(2):1155–1161, April 2016.

[84] P. Maj. High speed X-ray detection for timing correlation spectroscopy type experiments, April 2018.

[85] A. Dawiec, P. Maj, A. Ciavardini, P. Gryboś, C. Laulhé, C. Menneglier, and R. Szczygieł. Characterisation of the UFXC32k hybrid pixel detector for time-resolved pump-probe diffraction experiments at Synchrotron SOLEIL. *Journal of Instrumentation*, 12(03):C03057, March 2017.

[86] T. B. van Driel, S. Nelson, R. Armenta, G. Blaj, S. Boo, S. Boutet, D. Doering, A. Dragone, P. Hart, G. Haller, C. Kenney, M. Kwaitowski, L. Manger, M. McKelvey, K. Nakahara, M. Oriunno, T. Sato, and M. Weaver. The ePix10k 2-megapixel hard X-ray detector at LCLS. *Journal of Synchrotron Radiation*, 27(3):608–615, May 2020.

[87] Katherine S. Shanks, H. T. Philipp, D. Gadkari, J. T. Weizeorick, J. Baldwin, M. W. Tate, A. Miceli, and S. M. Gruner. The MM-PAD-2.1: A Wide-Dynamic-Range Detector For High-Energy X-ray Imaging. In *2020 IEEE Nuclear Science Symposium and Medical Imaging Conference (NSS/MIC)*, pages 1–2, October 2020.

[88] D. Gadkari, K. S. Shanks, H. Hu, H. T. Philipp, M. W. Tate, J. Thom-Levy, and S. M. Gruner. Characterization of 128 × 128 MM-PAD-2.1 ASIC: a fast framing hard x-ray detector with high dynamic range. *Journal of Instrumentation*, 17(03):P03003, March 2022.

[89] D. Pennicard and H. Graafsma. Simulated performance of high-Z detectors with Medipix3 readout. *Journal of Instrumentation*, 6(06):P06007, June 2011.

[90] S. Spannagel and P. Schütze. Allpix$^2$ – Silicon Detector Monte Carlo Simulations for Particle Physics and Beyond. *Journal of Instrumentation*, 17(09):C09024, September 2022.

[91] M. Collonge, P. Busca, P. Fajardo, and M. Williams. Monte Carlo simulations for XIDer, a novel digital integration X-ray detector for the next generation of synchrotron radiation sources. *Journal of Instrumentation*, 17(01):C01037, January 2022.

[92] T. Johng-ay, P. Fajardo, T. Martin, C. Ponchut, P.A. Douissard, and M. Ruat. DECIMO: A simulation tool to explore next generation of detectors for synchrotron radiation applications. In *2016 IEEE Nuclear Science Symposium, Medical Imaging Conference and Room-Temperature Semiconductor Detector Workshop (NSS/MIC/RTSD)*, pages 1–7, October 2016.

[93] J. Allison, K. Amako, J. Apostolakis, H. Araujo, P. Arce Dubois, M. Asai, G. Barrand, R. Capra, S. Chauvie, R. Chytracek, G. A. P. Cirrone, G. Cooperman, G. Cosmo, G. Cuttone, G. G. Daquino, M. Donszelmann, M. Dressel, G. Folger, F. Foppiano, J. Generowicz, V. Grichine, S. Guatelli, P. Gumplinger, A. Heikkinen, I. Hrivnacova, A. Howard, S. Incerti, V. Ivanchenko, T. Johnson, F. Jones, T. Koi, R. Kokoulin, M. Kossov, H. Kurashige, V. Lara, S. Larsson, F. Lei, O. Link, F. Longo, M. Maire, A. Mantero, B. Mascialino, I. McLaren, P. Mendez Lorenzo, K. Minamimoto, K. Murakami, P. Nieminen, L. Pandola, S. Parlati, L. Peralta, J. Perl, A. Pfeiffer, M.G. Pia, A. Ribon, P. Rodrigues, G. Russo, S. Sadilov, G. Santin, T. Sasaki, D. Smith, N. Starkov, S. Tanaka, E. Tcherniaev, B. Tome, A. Trindade, P. Truscott, L. Urban, M. Verderi, A. Walkden, J. P. Wellisch, D. C. Williams, D. Wright, and H. Yoshida. Geant4 developments and applications. *IEEE Transactions on Nuclear Science*, 53(1):270–278, February 2006.

[94] J. R. Janesick. *Photon Transfer*. SPIE Press, 2007.

[95] A. Owens and A. Peacock. Compound semiconductor radiation detectors. *Nuclear Instruments and Methods in Physics Research Section A: Accelerators, Spectrometers, Detectors and Associated Equipment*, 531(1):18–37, September 2004.

[96] M. C. Veale, S. J. Bell, D. D. Duarte, A. Schneider, P. Seller, M. D. Wilson, and K. Iniewski. Measurements of charge sharing in small pixel CdTe detectors. *Nuclear Instruments and Methods in Physics Research Section A: Accelerators, Spectrometers, Detectors and Associated Equipment*, 767:218–226, December 2014.

[97] A. Bergamaschi, S. Cartier, R. Dinapoli, D. Greiffenberg, J. H. Jungmann-Smith, D. Mezza, A. Mozzanica, B. Schmitt, X. Shi, and G. Tinti. Looking at single photons using hybrid detectors. *Journal of Instrumentation*, 10(01):C01033, January 2015.

[98] F. W. D. Rost. *Fluorescence Microscopy*. Cambridge University Press, March 1992.

[99] D. Schimansky, P. Busca, F. Erdinger, P. Fajardo, and P. Fischer. Concepts for the XIDer readout ASIC incorporating a pipelined ADC with very low dead time. *Journal of Instrumentation*, 16(03):P03023, March 2021.

[100] J. T. Weiss, K. S. Shanks, H. T. Philipp, J. Becker, D. Chamberlain, P. Purohit, M. W. Tate, and S. M. Gruner. High Dynamic Range X-Ray Detector Pixel Architectures Utilizing Charge Removal. *IEEE Transactions on Nuclear Science*, 64(4):1101–1107, April 2017.

[101] H. Krüger, J. Fink, E. Kraft, N. Wermes, P. Fischer, I. Peric, C. Herrmann, M. Overdick, and W. Rütten. CIX: a detector for spectrally enhanced x-ray imaging by simultaneous counting and integrating. In *Medical Imaging 2008: Physics of Medical Imaging*, volume 6913, pages 245–256. SPIE, March 2008.

[102] D. Schimansky, P. Busca, M. Collonge, P. Fajardo, P. Fischer, M. Ritzert, and M. Williams. Concepts for the data flow control on the XIDer readout ASIC. *Nuclear Instruments and Methods in Physics Research Section A: Accelerators, Spectrometers, Detectors and Associated Equipment*, 1057:168720, December 2023.

[103] A. Lozinskaya, I. Chsherbakov, I. Kolesnikova, T. Mihaylov, V. Novikov, A. Shemeryankina, O. Tolbanov, A. Tyazhev, and A. Zarubin. Detailed analysis of quasi-ohmic contacts to high resistive GaAs:Cr structures. *Journal of Instrumentation*, 14(11):C11026, November 2019.

[104] A. Lozinskaya, M. C. Veale, I. Kolesnikova, V. Novikov, O. Tolbanov, A. Tyazhev, R. M. Wheater, and A. Zarubin. Influence of temperature on the

energy resolution of sensors based on HR GaAs:Cr. *Journal of Instrumentation*, 16(02):P02026, February 2021.

[105] M. C. Veale, S. J. Bell, D. D. Duarte, M. J. French, M. Hart, A. Schneider, P. Seller, M. D. Wilson, V. Kachkanov, A. D. Lozinskaya, V. A. Novikov, O. P. Tolbanov, A. Tyazhev, and A. N. Zarubin. Investigating the suitability of GaAs:Cr material for high flux X-ray imaging. *Journal of Instrumentation*, 9(12):C12047, December 2014.

[106] M. C. Veale, P. Booker, Simon Cross, M. D. Hart, L. Jowitt, J. Lipp, A. Schneider, P. Seller, R. M. Wheater, M. D. Wilson, C. C. T. Hansson, K. Iniewski, P. Marthandam, and G. Prekas. Characterization of the Uniformity of High-Flux CdZnTe Material. *Sensors (Basel, Switzerland)*, 20(10):2747, May 2020.

[107] O. Baussens, C. Ponchut, M. Ruat, M. Bettelli, S. Zanettini, and A. Zappettini. Characterization of High-Flux CdZnTe with optimized electrodes for 4th generation synchrotrons. *Journal of Instrumentation*, 17(11):C11008, November 2022.

[108] P. Kraft, A. Bergamaschi, Ch Broennimann, R. Dinapoli, E. F. Eikenberry, B. Henrich, I. Johnson, A. Mozzanica, C. M. Schlepütz, P. R. Willmott, and B. Schmitt. Performance of single-photon-counting PILATUS detector modules. *Journal of Synchrotron Radiation*, 16(3):368–375, May 2009.

[109] H. Heikkinen, A. Gädda, S. Vähänen, J. Salonen, P. Monnoyer, G. Blaj, L. Tlustos, and M. Campbell. Low-temperature bump bonding of Timepix readout chips and CdTe sensors at Different Sensor pitches. In *2011 IEEE Nuclear Science Symposium Conference Record*, pages 4770–4775, October 2011.

[110] J.E. Clayton, C. M. H. Chen, W. R. Cook, and F. A. Harrison. Assembly technique for a fine-pitch, low-noise interface; Joining a CdZnTe pixel-array detector and custom VLSI chip with Au stud bumps and conductive epoxy. In *2003 IEEE Nuclear Science Symposium*, pages 3513–3517, 2004.

[111] M. Williams, P. Busca, M. Collonge, P. Fajardo, P. Fischer, T. Martin, M. Ritzert, M. Ruat, and D. Schimansky. XIDER: First Prototypes and Results with the Digital Integration Readout Scheme. In *2021 IEEE Nuclear Science Symposium and Medical Imaging Conference (NSS/MIC)*, pages 1–4, October 2021.

[112] M. Williams, P. Busca, M. Collonge, P. Fajardo, P. Fischer, T. Martin, M. Ritzert, M. Ruat, and D. Schimansky. XIDER: a novel X-ray detector for the next generation of high-energy synchrotron radiation sources. *Journal of Physics: Conference Series*, 2380(1):012091, December 2022.

[113] J. J. Prías-Barragán, L. Tirado-Mejía, H. Ariza-Calderón, L. Baños, J. J. Perez-Bueno, and M. E. Rodríguez. Band gap energy determination by photoacoustic absorption and optical analysis of $Cd_{1-x}Zn_xTe$ for low zinc concentrations. *Journal of Crystal Growth*, 286(2):279–283, January 2006.

[114] G. Fonthal, L. Tirado-Mejía, J. I. Marín-Hurtado, H. Ariza-Calderón, and J. G. Mendoza-Alvarez. Temperature dependence of the band gap energy of crystalline CdTe. *Journal of Physics and Chemistry of Solids*, 61(4):579–583, April 2000.

[115] T. Ytterdal, Y. Cheng, and T. A. Fjeldly. *Device Modeling for Analog and RF CMOS Circuit Design*. John Wiley & Sons, August 2003.

[116] B. Razavi. *Design of Analog CMOS Integrated Circuits*. McGraw-Hill Education, 2016.

[117] H. Spieler. *Semiconductor Detector Systems*. OUP Oxford, August 2005.

[118] M. Williams, P. Busca, M. Collonge, P. Fajardo, P. Fischer, T. Martin, M. Ritzert, M. Ruat, and D. Schimansky. Exploring the time-resolving capabilities of XIDer assemblies. *Nuclear Instruments and Methods in Physics Research Section A: Accelerators, Spectrometers, Detectors and Associated Equipment*, 1057:168688, December 2023.

# Acknowledgements

To conclude this thesis, I would like to thank everyone who has accompanied me on my journey through my doctorate.

First, I would like to thank my supervisor, Professor Dr. Peter Fischer, for the trust he placed in me, and for his support and advice during my research work. I would also like to thank Dr. Pablo Fajardo, for welcoming me into his group at the ESRF, providing me constructive feedback, and assuming the responsibility to be the second referee.

I want to thank especially Paolo Busca, for the close mentorship he provided me throughout the years of working at the ESRF. Great thanks for the numerous discussions and pieces of advice, as well as the open and friendly atmosphere during the many hours that we spent together on characterisation measurements at the laboratory and at the beamline. Special thanks as well for the extensive help in reviewing and proof-reading this manuscript.

I would also like to thank all my colleagues of the Dectector Unit at the ESRF, especially Morag Williams, Oriane Baussens, Marie Ruat, and Thierry Martin, for the constructive and relaxed collaboration, as well as my colleague David Schimansky from Heidelberg University, who always made himself available to walk me through the intricate features of the readout ASIC he designed.

Special thanks also go to my partner Claire, who has been very encouraging and understanding throughout my thesis. I would also like to thank my family and my friends, who have always supported me during this journey.

*The XIDer project was initiated in the framework of the ESRF Extremely Brilliant Source Upgrade Programme (ESRF-EBS) funded by the ESRF Members and Associated Countries and has received financial support from the ATTRACT project funded by the EC under Grant Agreement 777222.*